Dissertation zur Erlangung des Grades eines Doktors der Naturwissenschaften

Growth of Magnesio-Aluminate Spinel in Thin Film Geometry: In-situ Monitoring using Synchrotron X-Ray Diffraction

vorgelegt von

Dipl.-Geol. Lutz Christoph Götze

im Fachbereich Geowissenschaften

der Freien Universität Berlin

Berlin, Februar 2015

Erstgutachter: Prof. Dr. Susan Schorr

Zweitgutachter: PD Dr. Ralf Milke

Tag der Disputation: Freitag, 29.5.2015

Abstract

The solid-state reaction between corundum (α–Al_2O_3) and periclase (MgO) that forms at elevated temperatures spinel ($MgAl_2O_4$) at their contact is examined in this thesis. This rather well studied system serves as a model system for novel *in-situ* X-ray diffraction experiments in which the start and progress of the reaction is monitored in real-time. By using a diffusion couple setup in which oriented, single-crystalline substrates react with thin films and by analyzing the run products employing high-resolution techniques (synchrotron X-ray diffraction along with an *ex-situ* assessment by transmission electron microscopy (TEM)), spinel growth kinetics were investigated at the nanoscale. The temperatures as well as run durations of the experiments were low compared to most previous studies in this system. In air, the temperature was varied from 700 to 1000 °C, and run durations lasted from 5 minutes to 3 hours.

The spinel crystallites grew highly {111}-oriented in the *in-situ* experiments. The evolution of the integrated intensity of the 111 spinel Bragg reflection in the experiments was thus used for an assessment of the reaction kinetics. In the setup corundum substrate/MgO thin film, spinel growth was observed at temperatures ≥ 900 °C. A diffusion-controlled reaction regime operated at 900 °C whereas at 1000 °C an interface-controlled reaction regime was found. Reaction rates were considerable faster in the setup periclase substrate/Al_2O_3 thin film in which the reactant layer crystallized to γ–Al_2O_3 (a defect spinel). Growth was observed at temperatures ≥ 800 °C in this setup. A diffusion-controlled reaction regime operated at 800 °C whereas an interface-controlled reaction regime was found at 900 and 1000 °C.

TEM was used as a complementary technique to study microstructures and microtextures of the spinel layers. By TEM analyses, it is demonstrated that the proposed diffusion mechanism for this system (the counterdiffusion of the cations through a relatively rigid oxygen sublattice) that is proven to operate in μm-thick spinel reaction bands operates also at the nanoscale. The diffusion mechanism can be deduced from the position of the initial substrate/thin film interface inside the reaction layer which is visible due to a change in microstructure. Positive and negative volume changes at the substrate/spinel phase boundaries that follow from the reaction stoichiometry of this mechanism are also displayed in TEM micrographs. Additionally, pole figures and diffraction patterns show that the layers grew topotaxially, i.e. with a distinct crystallographic relationship to the single crystal substrates, into the substrates.

Kurzreferat

In der vorliegenden Arbeit wird die Festkörperreaktion zwischen Korund (α–Al_2O_3) und Periklas (MgO) untersucht, die bei erhöhten Temperaturen Spinell ($MgAl_2O_4$) an ihrem Kontakt entstehen lässt. Dieses schon gut erforschte System dient als Modellsystem für neuartige in-situ Röntgenbeugungsexperimente, bei welchen der Start und Fortschritt einer Reaktion in Echtzeit verfolgt werden kann. Indem Diffusionspaare aus orientierten Einkristall-Substraten und Dünnschichten benutzt wurden und durch Verwendung von hochauflösenden Analysemethoden (Synchrotron-Röntgenbeugung in Kombination mit einer ex-situ Analyse mittels der Transmissionselektronenmikroskopie (TEM)), konnte das Spinell-Wachstum auf der Nanoskala untersucht werden. Die Temperaturen und Versuchsdauern der Experimente waren dabei niedrig bzw. kurz im Vergleich zu den meisten zuvor durchgeführten Studien in diesem System. Unter Atmosphärendruck wurde die Temperatur von 700 bis 1000 °C variiert, und Versuche liefen zwischen 5 Minuten und 3 Stunden.

In den in-situ Experimenten wuchsen die Spinellkristalle in hohem Maße {111}-orientiert. Aus diesem Grund konnte die Entwicklung der integralen Intensität der 111 Spinell Bragg-Reflexion in einem Experiment dazu benutzt werden, die jeweilige Reaktionskinetik abzuleiten. Im Setup Korund-Substrat/MgO-Dünnschicht wurde Wachstum bei Temperaturen ≥ 900 °C beobachtet. Hierbei wurde ein diffusionskontrolliertes Reaktionsregime bei 900 °C gefunden, während die Reaktion bei 1000 °C grenzflächenkontrolliert ablief. Reaktionsraten waren deutlich schneller im Setup Periklas-Substrat/Al_2O_3-Dünnschicht, in welchem die Reaktionsschicht zu γ–Al_2O_3 (einem Defekt-Spinell) kristallisierte. Hier wurde Wachstum bei Temperaturen ≥ 800 °C beobachtet. Ein diffusionskontrolliertes Reaktionsregime wurde bei 800 °C gefunden, während bei 900 und 1000 °C das grenzflächenkontrollierte Regime wirksam war.

TEM wurde als komplementäre Analysemethode benutzt, um Mikrostrukturen und -texturen der Reaktionsschichten zu studieren. Aus der TEM-Analyse wurde ersichtlich, dass der Diffusionsmechanismus dieses Systems (eine Gegendiffusion der Kationen durch ein eher rigides Sauerstoffuntergitter), der auf der μm-Skala schon oft nachgewiesen wurde, auch auf der Nanoskala wirkt. Der Mechanismus kann von der Position der initialen Grenzfläche zwischen den Reaktanten innerhalb der Reaktionsschicht abgeleitet werden, die durch einen natürlichen Mikrostrukturwechsel abgebildet wird. An den Phasengrenzen deuten auch negative und positive Reaktionsvolumenänderungen auf den Mechanismus. Zudem belegen Polfiguren und Beugungsmuster, dass die Schichten topotaktisch, d. h. mit einer bestimmten kristallographischen Orientierungsbeziehung zum Einkristall-Substrat, in die Substrate gewachsen sind.

Contents

List of Figures

List of Tables

Preface

The thesis is organized as follows. The motivation for the experiments presented in this study, the crystal structure of spinel and the current state of research regarding the experimental growth of spinels is presented in chapter 'Introduction'. In the following chapter 'Materials and Methods', detailed information on the substrates, the fabrication of thin films via pulsed laser deposition and the procedure during the *in-situ* experiments is given. In chapter 'Results', the outcomes of the *in-situ* experiments, texture measurements and transmission electron microscopy microstructure analysis are presented. These results are interpreted and discussed in the fourth chapter 'Discussion'. A summary is given in the last chapter. Additional informations such as a list of frequently used abbreviations can be found in the Appendix.

Results of one of the experimental setups (the corundum substrates two-layer setup presented in section 3.2.3) were published in Götze et al. (2014).

1 Introduction

1.1 Motivation

Reaction bands are a common phenomenon produced by solid-state reactions. In rocks, the corresponding microstructure is referred to as a corona structure or metasomatic reaction band. Experimental reaction rim growth is an essential tool in the Earth sciences for investigating reaction band formation and for quantifying the underlying processes (Götze et al., 2014). This notion motivated several experimental studies investigating reaction rim growth in mineral systems (e.g. Yund, 1997; Milke et al., 2001, 2007; Milke and Wirth, 2003; Watson and Price, 2002; Götze et al., 2010; Keller et al., 2010; Gardés et al., 2011; Joachim et al., 2011; Helpa et al., 2014). Usually, as in the cited studies, run products are analyzed optically or by scanning electron microscopy after the diffusion anneal missing the initial and transient stages of reaction band formation, and growth kinetics are investigated by conducting time series. Additionally, accurate measurements regarding the extent of the reaction product may then require relatively thick reaction rims typically >5–$10\,\mu$m, and these long diffusion distances limit experiments to relatively high temperatures (Yund, 1997) which are often outside the range present in the Earth's crust.

In the experiments presented in this thesis, these disadvantages are circumvented by observing the reaction band formation *in-situ* using energy-dispersive as well as angle-dispersive synchrotron X-ray diffraction in combination with a heating attachment. By using a substrate/thin film experimental setup and high-resolution analytical techniques (*in-situ* synchrotron X-ray diffraction along with an *ex-situ* analysis by focused ion beam assisted transmission electron microscopy), the temperatures as well as run durations were low compared to most previous studies in the MgO–Al_2O_3 system. Experiments were conducted between 700 and 1000 °C, and the maximum run duration was 3 hours. As a model reaction for the *in-situ* rim growth monitoring, spinel ($MgAl_2O_4$) layers were synthesized at contacts between alumina (Al_2O_3) polymorphs and periclase (MgO) according to the reaction $Al_2O_3 + MgO \longrightarrow MgAl_2O_4$. Due to the low temperatures and short run durations that where applied, nanoscale reaction bands were synthesized, i.e. they are about three orders of magnitude smaller than the reaction rims grown in the studies cited above. The experiments address in particular:

- The earliest stages of a mineral reaction, i.e. the formation of the first few lattice planes of a phase that grows at the contact between two phases that cannot coexist thermodynamically stable anymore at elevated temperatures

- The subsequent growth kinetics of this phase

Some more questions that are addressed are:

- At which temperature will the product phases react to form the spinel?
- Is there a difference in reaction rate when corundum or vice versa periclase is used as substrate?
- What is the temperature-dependent growth behavior of spinel at the nanoscale?
- What is the diffusion mechanism at the nanoscale?
- What is the texture of the *in-situ* grown spinel layers?
- How do lattice plane distances and peak shapes evolve during the *in-situ* experiment?

1.2 Spinel

After a brief presentation of the system MgO–Al_2O_3, an overview about the crystal structure of spinels in general as well as spinel *sensu stricto* and its geological relevance is given in this section.

1.2.1 The System MgO–Al_2O_3

The phase diagram of the quasi-binary system MgO–Al_2O_3 is presented in Figure 1.1. Several features of the diagram are noteworthy:

- Only spinel exists as an intermediate phase
- No phase transition of spinel occurs up to its melting point
- Spinel is stoichiometric at low temperatures up to about 1050 °C
- At temperatures above 1050 °C, MgO is only moderately soluble in spinel
- Al_2O_3 is highly soluble in spinel at elevated temperatures

Considering the dissimilar solubilities of the oxides, the chemical formula of spinel may be expressed as $MgO \cdot n\,Al_2O_3$ where n can range from about 0.6 to 7. To guarantee electroneutrality, vacancies have to be formed for the excess Al^{3+} ions introduced into the spinel lattice (Hallstedt, 1992).

The experiments of this study were conducted at temperatures $\leq 1000\,°C$; therefore, it is assumed that the spinel throughout the layer is stoichiometric.

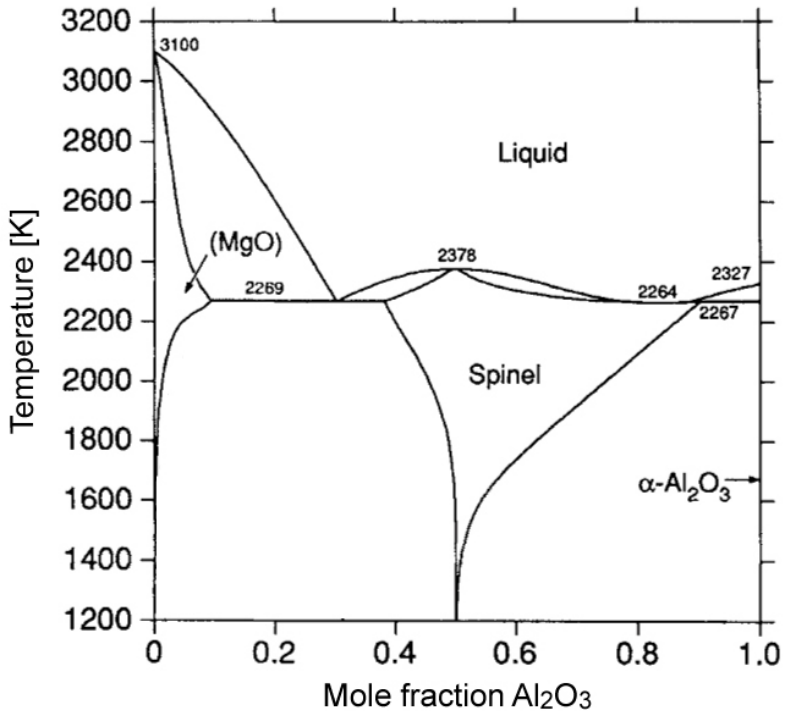

Figure 1.1: MgO–Al_2O_3 phase diagram at 1 bar. Modified after Hallstedt (1992).

1.2.2 Crystal Structure of Spinel

The crystal structure is basically the same for all spinel group minerals. This group contains geologically and industrially important minerals such as hercynite ($FeAl_2O_4$), magnetite ($Fe^{2+}Fe_2^{3+}O_4$), chromite ($FeCr_2O_4$) and ringwoodite (γ–$(Mg, Fe)_2SiO_4$). Ringwoodite is a high-pressure polymorph of olivine in the transition zone of Earth's mantle. The spinel group may be subdivided into three series, according to whether the trivalent ion is aluminum, iron or chromium, but pure end-members are rare as natural minerals (Deer et al., 1992). For instance, in spinel *sensu stricto* Mg^{2+} can be substituted by Fe^{2+} and Al^{3+} by Fe^{3+}.

The general chemical formula of spinels may be written as XY_2O_4. The cations X and Y are transition elements with oxidation states of +1 to +6, demonstrating that no trivalent ion necessarily has to be present as it is the case in ringwoodite. It follows that the valencies of the cations may be either

- X = 2+ and Y = 3+,
- X = 4+ and Y = 2+,
- or X = 6+ and Y = 1+.

Additionally, instead of oxygen, sulphur, selenium or tellurium can form the anion sublattice in spinels.

Spinel *sensu stricto* crystallizes in the cubic crystal system with the lattice constant $a_0 = 8.084\,\text{Å}$ ($Z = 8$); the space group is $Fd\bar{3}m$ (number 227) (e.g. Redfern et al., 1999). All three ions in spinel form face-centered cubic (fcc) sublattices that interpenetrate themselves (Schmalzried and Wagner, 1962). The aluminum ions occupy one-half of the octahedral interstices formed by the cubic close-packed (ccp) oxygen sublattice whereas the magnesium ions occupy one-eighth of the available tetrahedral sites. Thus, in the unit cell are 16 of the 32 octahedral interstices occupied by Al^{3+} and 8 of the 64 tetrahedral interstices are occupied by Mg^{2+}; such a unit cell is presented in Figure 1.2. The Wyckoff positions for O^{2-}, Mg^{2+} and Al^{3+} are 32e, 8a, and 16d, respectively. However, for the complete description of the general oxygen positions, the oxygen parameter u is required that is 0.25 if the anions form an exact ccp sublattice (O'Neill and Navrotsky, 1983). For spinel *sensu stricto*, this parameter is 0.2624, meaning that the ccp oxygen sublattice is slightly deformed.[1]

In this $X^{[4]}[Y^{[6]}Y^{[6]}]O_4$ configuration, where [4] and [6] denote coordination numbers, spinels are designated as normal spinels, as it was introduced by Verwey and Heilmann (1947). Upon heating, however, the cations start to change positions and a more random distribution of the cations on octahedral and tetrahedral sites is attained

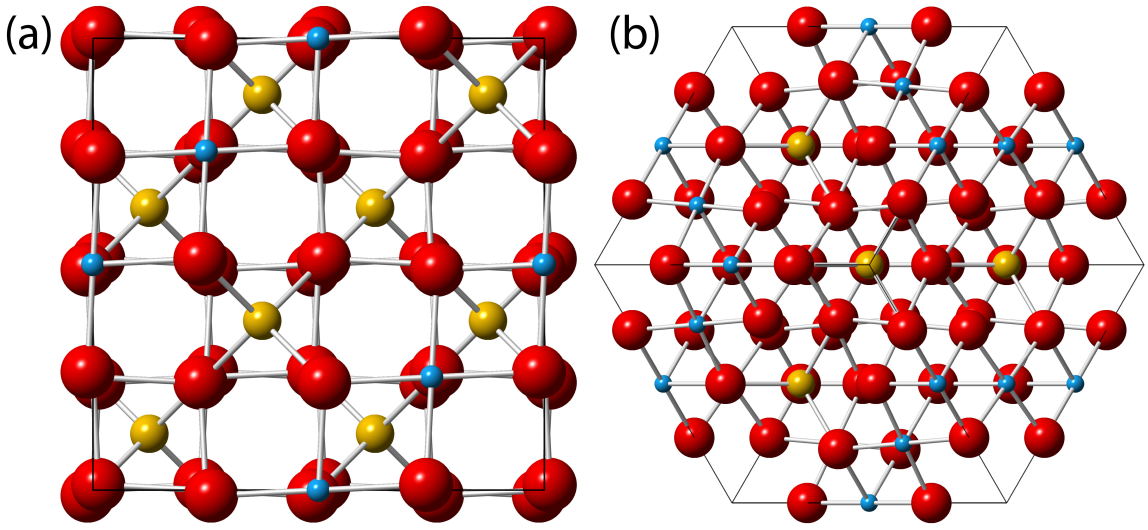

Figure 1.2: Schematics of the spinel crystal structure. (a) (100) face. (b) (111) face. In the unit cell are 16 of the 32 octahedral interstices formed by the oxygen sublattice (red spheres) occupied by aluminum (blue spheres), and 8 of the 64 tetrahedral interstices are occupied by magnesium (yellow spheres).

[1] When $u > 0.25$, the anions move away from the nearest tetrahedral cation in a [111] direction, increasing the size of the tetrahedra and decreasing the size of the octahedra (Hill et al., 1979).

(Hallstedt, 1992); the spinel is then designated as an intermediate spinel. The spinel structure is inverse when all of the X atoms occupy octahedral sites and one-half of the Y atoms occupy tetrahedral sites. The general chemical formula may then be rewritten as $Y^{[4]}[X^{[6]}Y^{[6]}]O_4$. As an example, magnetite is an inverse spinel. The inversion parameter i, which is the fraction of tetrahedral sites occupied by Y ions, accounts for the degree of inversion (O'Neill and Navrotsky, 1983). Thus, for normal spinels $\mathrm{i} = 0$, for the perfect random arrangement $\mathrm{i} = 2/3$ and for inverse spinels $\mathrm{i} = 1$.

Naturally grown magnesio-aluminate spinels are nearly normal but synthetic ones are always partially inverse (Sickafus et al., 1999). Synthetic spinel is 10 to 30 % disordered when quenched from temperatures above 1000 °C (Navrotsky et al., 1986). Wood et al. (1986) found $\mathrm{i} = 0.38$ for all samples quenched from 900 to 1600 °C whereas Redfern et al. (1999) reported a value of $\mathrm{i} = 0.21$ for synthetic spinel at 1000 °C. It is thus suggested that the spinels synthesized in this study are to a certain degree intermediate.

In summary, three structural parameters determine the atomic arrangements in spinels (Sickafus et al., 1999):

1. The lattice parameter a, which is dependent on the average effective cation radius, but without significant dependence on the specific cation arrangement specified by i

2. The cation inversion parameter i

3. The anion parameter u which is highly dependent on i

A so called defect spinel is γ–Al_2O_3 ($a_0 = 7.91$ Å; Zhou and Snyder, 1991). To depict the similarity to ordinary spinel group minerals, the formula can be written as $\square_{1/3}Al_{8/3}O_4$ where $\square$ denotes a vacancy, i.e. a cation position in the normal spinel structure that is not occupied in the defect spinel. These vacancy defects have to be introduced due to charge compensation. Thus, in the unit, cell $21\frac{1}{3}$ of the 24 octahedral and tetrahedral sites are occupied by Al^{3+} and $2\frac{2}{3}$ of these sites are occupied by vacancies. Conflicting results were reported on whether these defects are situated preferably on octahedral or tetrahedral sites (Gutiérrez et al., 2002, and references therein).

A comprehensive overview about all the Al_2O_3 polymorphs and the sequences of phase transformations towards the stable α–Al_2O_3 phase (corundum) is given in Levin and Brandon (1998). γ–Al_2O_3 and the other metastable alumina polymorphs are transformed irreversibly to corundum upon calcination above 1000 °C (Greenwood and Earnshaw, 1990; Levin and Brandon, 1998).

1.2.3 Geological Relevance and Occurence of Spinel

Spinel is a common high-temperature mineral in metamorphic rocks and peridotites. It occurs in contact-metamorphosed limestones, and it is found in a similar association in regionally metamorphosed limestones (Deer et al., 1992). In Earth's mantle, spinel

lherzolite is suggested to be present at depths between about 40 to 70 km (Matthes, 2001). In these peridotitic rocks, spinel can be used as a geothermometer due to partitioning of Mg^{2+} and Fe^{2+} between coexisting spinel and olivine (e.g. Fabries, 1979). At greater depths, the spinel is replaced by garnet according to the idealized reaction $MgAl_2O_4 + 2\ Mg_2Si_2O_6 \longrightarrow Mg_2SiO_4 + MgAl_2Si_3O_{12}$ (Redfern et al., 1999; Wood et al., 2013).

Lherzolite is the dominant rock type in the asthenosphere and is the source of basalt. Aluminum, an essential component in basalt, is largely present in lherzolites in plagioclase at low pressures (< 10 kbar), in spinel group minerals at intermediate pressures (10–20 kbar) and in garnet at high pressures (> 20 kbar). Most of the vast basalt regions of the Earth are considered to be derived by partial melting of spinel lherzolite (Haggerty, 1991).

1.3 Experimental Growth of Spinels — State of Research

The diffusion mechanism of the spinel-forming reaction is explained and an overview about the experimental growth of spinels in the literature is given in the following three subsections.

1.3.1 Diffusion Mechanism

The spinel-forming reaction can be quantitatively treated as a model of a classical solid state reaction (Schmalzried, 1981). The condition of charge neutrality of the overall diffusion flux through the spinel product layer allows three limiting cases of combinations of the diffusing species (Hesse et al., 1994):[2]

1. Diffusion of 2 Al^{3+} and 3 O^{2-} from the corundum/spinel interface to the periclase/spinel interface
2. Diffusion of Mg^{2+} and O^{2-} from the periclase/spinel interface to the corundum/spinel interface
3. Counterdiffusion of 2 Al^{3+} and 3 Mg^{2+}

In the first scenario, one mole spinel would be formed at the periclase/spinel interface for every mole Al_2O_3 released at the corundum/spinel interface, and the chemical equation reads:

$$MgO + 2\ Al^{3+} + 3\ O^{2-} \longrightarrow MgAl_2O_4 \tag{1.1}$$

[2]Due to the coupling of the ionic fluxes in the reaction product, the reaction rate is determined by the ionic species whose mobility is intermediate between that of the other two (e.g. Schmalzried, 1981).

A marker, e.g. inert platinum particles, deposited at the initial corundum/periclase phase boundary would be located at the corundum/spinel interface after the experiment, indicating that only Al^{3+} and O^{2-} were mobile, i.e. $D_{Al^{3+}}$ and $D_{O^{2-}} \gg D_{Mg^{2+}}$. In the second scenario, one mole spinel would be formed at the corundum/spinel interface for every mole MgO released at the periclase/spinel interface, and the chemical equation reads:

$$Al_2O_3 + Mg^{2+} + O^{2-} \longrightarrow MgAl_2O_4 \tag{1.2}$$

An inert marker would be located at the periclase/spinel interface after an epxeriment, indicating that only Mg^{2+} and O^{2-} were mobile, i.e. $D_{Mg^{2+}}$ and $D_{O^{2-}} \gg D_{Al^{3+}}$. In the third scenario, the counterdiffusion of the cations through the product layer, spinel is formed at both interfaces. The chemical equation at the corundum/spinel interface reads:

$$3\ Mg^{2+} + 4\ Al_2O_3 \longrightarrow 3\ MgAl_2O_4 + 2\ Al^{3+} \tag{1.3}$$

and that on the periclase/spinel interface:

$$2\ Al^{3+} + 4\ MgO \longrightarrow 1\ MgAl_2O_4 + 3\ Mg^{2+} \tag{1.4}$$

From theoretical considerations and experimental evidence, the first two scenarios are unlikely because diffusion of oxygen in spinels, possessing a dense packed oxygen sublattice and not providing diffusion channels for the large anions, is slow (Schmalzried, 1981; Hesse et al., 1994), i.e. $D_{Al^{3+}}$ and $D_{Mg^{2+}} \gg D_{O^{2-}}$. Koch and Wagner (1936) first suggested that the diffusion mechanism in this system can be regarded as 'counterdiffusion of the cations through a rigid oxygen sublattice', i.e. the third scenario, the same mechanism that they found for the formation of Ag_2HgI_4 from AgI and HgI_2 where the iodine forms the anion sublattice. Since then, it has been proven several times in experimental studies that this mechanism controls the spinel growth. Many of these studies are reviewed in subsections 1.3.2 and 1.3.3.

It can be seen in chemical equations 1.3 and 1.4 that spinel is produced in a proportion 1:3 at the respective interfaces. A schematic of this scenario is presented in Figure 1.3. As long as an inert marker did not move in the experiment, it will be located at a depth 1/4 of the overall reaction band width away from the periclase/spinel interface towards the corundum/spinel interface. With respect to the sublayer thicknesses, the smaller, periclase-grown sublayer may be thus designated as the 25 % layer and the bigger, corundum-grown sublayer as the 75 % layer.

The 1:3 sublayer ratio is not fixed though; inspection of the MgO–Al_2O_3 phase diagram (Figure 1.1) reveals that at high temperatures, assuming thermodynamic equilibrium at the interface, a non-stoichiometric spinel coexists next to corundum. The amount of Al_2O_3 soluble in spinel increases with increasing temperature whereas the solubility of excess MgO in spinel next to the periclase/spinel interface is rather limited. This non-stoichiometry in spinel reaction rims was observed by e.g. Watson and Price (2002), Götze et al. (2010), Keller et al. (2010) and Jeřábek et al. (2014).

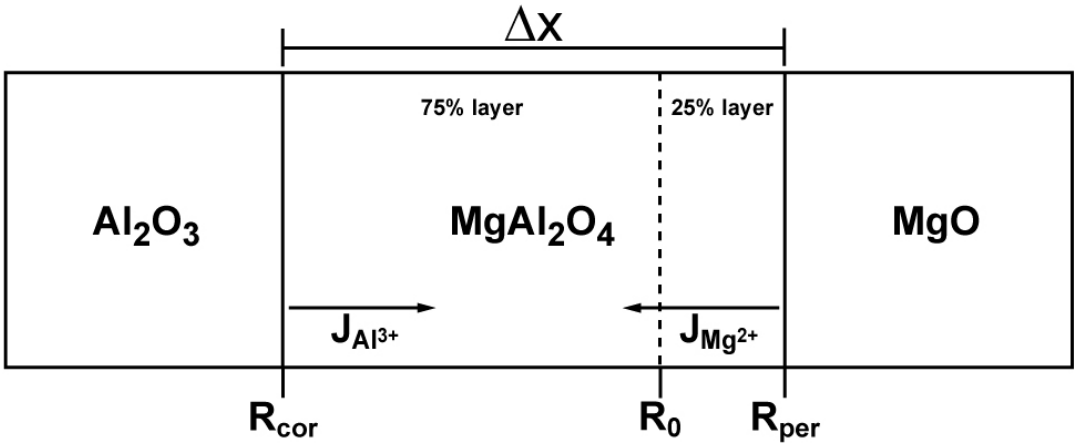

Figure 1.3: Schematic of spinel sublayers in a reaction band. The position of the original corundum/periclase interface is indicated by the dashed line labeled R_0; an inert marker would be located at this position after a diffusion anneal. R_{cor} and R_{per} denote the positions of the corundum/spinel and periclase/spinel interfaces, respectively. Δx denotes the overall reaction band thickness. $J_{Al^{3+}}$ and $J_{Mg^{2+}}$ denote the diffusive fluxes of the cations across the growing spinel layer.

The molar volume changes involved in chemical equations 1.3 and 1.4 can easily be calculated. From the conversion of 4 moles Al_2O_3 to 3 moles $MgAl_2O_4$ at the corundum/spinel interface, it follows that (calculated for 1000 °C and 1 bar using thermodynamic data from Holland and Powell (1998) and the open-source program Perple_X (Connolly, 1990; Connolly, 2005)):

$$\Delta V_{r\ cor/sp} = 3\ \cdot\ V_{m\ sp} - 4\ \cdot\ V_{m\ cor} = 17.54\ cm^3 \tag{1.5}$$

The reaction volume at this interface is positive (5.85 cm^3 per mole spinel formed) whereas that on the periclase/spinel interface is negative:

$$\Delta V_{r\ per/sp} = 1\ \cdot\ V_{m\ sp} - 4\ \cdot\ V_{m\ per} = -\ 5.86\ cm^3 \tag{1.6}$$

The volume changes at the corundum/spinel and the periclase/spinel interfaces are +16.72 % and –12.58 %, respectively, relative to the starting configurations. The overall reaction volume is positive ($\Delta V_r = 2.92\ cm^3$/mole). The net volume expansion amounts to 7.7 %.

The formation of gahnite ($ZnAl_2O_4$) between hexagonal ZnO and Al_2O_3 proceeds not via the cation counterdiffusion mechanism but via Kirkendall-type diffusion (e.g. Güder et al., 2011; Fan et al., 2006, 2007b; Yang et al., 2008). Kirkendall-type diffusion refers to a non-equilibrium interdiffusion process where vacancy diffusion towards the side of the faster diffusing species compensates for the unequal material flux (Fan et al., 2007). These vacancies may then form pores within the fast-diffusion side which eventually can

collect into voids, the so-called Kirkendall voids. In Nakajima (1997), the history of the discovery and acceptance of the Kirkendall effect is described. The effect was discovered by E. O. Kirkendall (Kirkendall, 1942; Smigelskas and Kirkendall, 1947). The Kirkendall experiment established that diffusion of substitutional lattice atoms involves defects that facilitate atomic jumps; in most materials these atomic defects are empty lattice sites which are termed vacancies (Fan et al., 2007).

1.3.2 Experimental Growth of Spinels on the μm-scale

In this and the following subsection, a summary is given of what has been done so far regarding the experimental growth of spinels at the μm-scale as well as at the nm-scale using thin films. Because not all papers on spinel growth can be reviewed in the context of this thesis, it should be noted that this topic was studied extensively by three scientists and their respective co-workers, namely the groups around H. Schmalzried, C. B. Carter and D. Hesse. The earliest studies confirmed the diffusion mechanism proposed by Koch and Wagner (1936) and investigated the crystallographic relationships between reactants and spinel.

Carter (1961) conducted experiments at 1900 °C for 48 hours using single crystal as well as polycrystalline corundum disks that reacted with a MgO vapor in a hydrogen atmosphere. He found the initial corundum/periclase interface inside the spinel reaction band using molybdenum markers. Determining a 1:3 spinel sublayer ratio, he concluded that Al^{3+} and Mg^{2+} must counterdiffuse through the spinel.

Navias (1961) conducted time series from 1 to 50 hours at temperatures ranging from 1500 to 1900 °C. Corundum reacted with vaporized MgO in a hydrogen atmosphere. He found that the spinel grows diffusion-controlled, and for the formation, an activation energy of 419 kJ/mole was reported. In an oxidizing atmosphere, spinel was formed only when corundum and periclase were in direct contact.

Rossi and Fulrath (1963) conducted experiments at 1560 °C in air for 250 hours with an emphasis on the crystallographic dependence of the spinel formed on the orientation of the parent crystals. The diffusion mechanism was confirmed from the ratio of the two spinel sublayers, and it was found that the reaction rate is independent of the orientation of the parent crystals. In the diffusion couple (0001) corundum/(111) periclase, they found that spinel grows topotaxially into corundum with (0001) corundum ∥ (111) spinel and $[10\bar{1}0]$ corundum ∥ [110] spinel. In this configuration, the close-packed oxygen planes and directions of close packing within the planes coincide in both structures.

Whitney and Stubican (1971) conducted experiments at temperatures between 1565 and 1900 °C and run durations between 1 and 140 hours. They found a diffusion-controlled reaction regime. The reaction rate was virtually the same using (0001)- or $(10\bar{1}0)$-oriented corundum single crystals. Activation energies of 520 kJ/mole for temperatures up to 1750 °C and 370 kJ/mole for higher temperatures were reported; they hypothesized a change in the diffusion mechanism through the non-stoichiometric spinel.

Mackenzie and Ryan (1981) studied interdiffusion in polycrystalline MgO and Al_2O_3 in the temperature range 1300–1450 °C in air for 48 hours by applying an electric field on the diffusion couples. By using polycrystalline pellets, the reactivity was enhanced with respect to previous studies so that temperatures as well as run durations could be lowered. They demonstrated that the interdiffusion in an electric field is faster, particularly when the alumina pellet is negatively charged. They argued that this result is another indication that the migrating species in this direction is Mg^{2+}. Platinum wire markers were used to identify the initial corundum/periclase interface after the experiments, but the expected sublayer ratio for a given temperature was rarely observed. For unelectrolyzed samples, an activation energy of 384 kJ/mol was reported.

Zhang et al. (1996) conducted experiments in the temperature range 1200–1600 °C in air for run durations up to 166 hours using polycrystalline pellets. They found a diffusion-controlled reaction regime for all temperatures and reported an activation energy of 540 kJ/mole.

Watson and Price (2002) studied the kinetics of the spinel-forming reaction in the temperature range 1200–2000 °C at pressures from 1.0 to 4.0 GPa for run durations of up to 240 hours. These long run durations had to be applied for the 1200 °C experiments to obtain reasonably thick reaction products that could be analyzed by an electron microprobe (the minimum thickness was 6 μm). For all investigated temperature/pressure combinations, a diffusion-controlled reaction regime was found. The cation counterdiffusion mechanism could be deduced from back-scattered electron images by identifying two sublayers within the spinel with a 1:3 thickness ratio. Paradoxically, in the same images a platinum foil marker was found at the periclase/spinel interface, suggesting that Mg^{2+} and O^{2-} were mobile (this demonstrates that the use of markers is not always reliable). The activation energy for spinel growth of about 410 kJ/mole was found to be pressure independent but the reaction rate clearly slowed down with increasing pressure.

Liu et al. (2005) conducted experiments at 1300 and 1600 °C in air for 5 up to 30 hours. They found a diffusion-controlled reaction regime and that the layer grows topotaxially into the corundum.

Götze et al. (2010) and Keller et al. (2010) examined the effect of uniaxial stress applied normal to the reaction interface on reaction rim growth. The temperature was varied from 1250 to 1350 °C, the uniaxial stress from 2.9 to 29 MPa and runs lasted from 36 to 157 hours. They found that the reaction rate increases significantly by increasing the uniaxial stress when single crystals as starting materials are used, and they suggested that the stress-induced increase in spinel grain boundary misorientation is accountable for the effect. The change of the grain boundary character from low-angle to a higher fraction of high-angle grain boundaries was demonstrated using electron-backscatter diffraction (EBSD). The orientation relationship at low stresses was the same observed by Rossi and Fulrath (1963), namely (0001) corundum ∥ (111) spinel and $[10\bar{1}0]$ corundum ∥ [110] spinel. This in-plane orientation is succesively lost by imposing higher stresses. On the other hand, compressive stress triggered the formation of a coherent periclase/spinel reaction interface; a (311) periclase ∥ (311) spinel interface deve-

loped. The significant effect on rim growth rates was not observed using polycrystalline Al_2O_3 as starting material where high-angle grain boundaries were already inherited, and, consequently, reaction rates were in every case fast. EBSD could as well display the initial corundum/periclase interface by different grain structures in the two sublayers and by different crystallographic orientations of these grains. Götze et al. (2010) gave an activation energy of 416 kJ/mole for the formation of spinel.

Similar results regarding the kinetics of formation and crystallographic relationships were also reported early for other spinels (e.g. Thirsk and Whitmore, 1940, for $NiAl_2O_4$; Schmalzried, 1962, for Co_2TiO_4 and $CoCr_2O_4$; Pettit et al., 1966, for $NiAl_2O_4$).

1.3.3 Experimental Growth of Spinels on the nm-scale

Using the substrate/thin film approach, the growth of spinels was also studied on the nanoscale.

Comer et al. (1966) studied the reaction between a (001)-oriented periclase substrate and a 20 nm thick thin film of γ–Al_2O_3. The γ–Al_2O_3 crystallized at 510 °C by oxidation of an alumina thin film. Substrate and film started to react at about 540 °C to form a monocrystalline layer of spinel with (001) periclase || (001) spinel. An additional polycrystalline layer was observed at temperatures 590–800 °C. They argued that the monocrystalline layer was formed by consumption of the substrate and the polycrystalline layer by consumption of the γ–Al_2O_3 layer.

Duckwitz and Schmalzried (1971) studied the formation of spinels at temperatures from 1247 to 1420 °C in air thermogravimetrically. They found interface-controlled reaction regimes that were followed by diffusion-controlled reaction regimes. Interface-controlled growth was found for $ZnAl_2O_4$ at 1247 °C during the first 4 minutes of the experiment after which the reaction regime gradually switched over to a diffusion-controlled one.

Li et al. (1992) produced spinel between epitaxial MgO thin films on corundum substrates accidentally by irradiation with an electron beam during TEM analysis. They found a parabolic growth law and reported a reaction rate constant of $\overline{k} = 5.7\,\text{Å}^2/\text{min}$. The maximum thickness of the reaction band (formed in about 3 hours) was only 3 nm. The temperature of formation remains unclear, but, with respect to the rate of formation, should be well below 1000 °C.

Hesse et al. (1994) found that the cation counterdiffusion mechanism operates also at the nanoscale. In the substrate/thin film diffusion couple $(1\bar{1}02)$ corundum/(001) MgO, platinum markers were found inside the reaction band at the compatible position; this spinel layer was about 50 nm thick. Experiments were carried out at 1100 °C for 30 minutes and 1 hour. Using high-resolution transmission electron microscopy (HRTEM), a particular focus of this study was on the structure of the corundum/spinel reaction front. They found a systematic $5 \pm 0.5°$ tilt of the (001) spinel lattice planes around the [010] spinel axis deviating from the exact $(1\bar{1}02)$ corundum ∥ (001) spinel and $[11\bar{2}0]$ corundum ∥ [010] spinel orientation relation. They attributed this tilt to the sys-

tem trying to attain a coherent state at the interface because the misfit at the reaction front is reduced due to the tilt. A similar observation was reported by Carter and Schmalzried (1985) from the semi-coherent interface (0001) corundum/(111) $CoAl_2O_4$.

Sieber et al. (1996) used (001)-oriented periclase substrates that reacted with an Al_2O_3 vapour at 1000 to 1200 °C as well as $(1\bar{1}02)$-oriented corundum substrates that reacted with epitaxial MgO thin films at 1100 °C for 1 hour. A particular focus was laid on the structure of the reaction fronts at the atomic level using high-resolution TEM. The cation counterdiffusion mechanism was deduced from the position of a platinum marker layer. The Al_2O_3 vapour crystallized as γ–Al_2O_3, but reaction rates were apparently slower than in Comer et al. (1966).

Sieber et al. (1997b, 1997c) studied the reaction $MgO + In_2O_3 \longrightarrow MgIn_2O_4$ using thin and thick films, 250 nm and 3–4 μm in thickness, respectively. The In_2O_3 thin films reacted between 1300 and 1500 °C for 1 hour and the thick films at 1500 °C for 4 hours. From differences in the dislocation structures at the reaction fronts, they proposed an interface-controlled reaction mode in the thin films and an diffusion-controlled mode in the thick films. In thin films, the Burgers vectors of the misfit dislocations are pointing out of the interface which enables a fast glide of the dislocations that have to move together with the reaction front. In thick films, however, the Burgers vectors lying in the interface plane and dislocations have to climb during the reaction. They concluded that the mode of dislocation movement is different for the interface- and diffusion-controlled reaction regimes.

Sieber et al. (1997) demonstrated that the structure of a reaction front depends on the sign and amount of the lattice mismatch between various spinels and a (001)-oriented MgO substrate, i.e. whether dislocations have to glide or climb during interface movement. Due to a negative misfit of 4.1 % at the (001) periclase $\|$ (001) spinel interface, dislocations have to climb at this reaction front.

He and Becker (1997) found an interface-controlled reaction regime in an optical *in-situ* study at temperatures between 1000 and 1100 °C for the growth of $CoAl_2O_4$ on (0001)- and $(11\bar{2}0)$-oriented corundum single crystals. At 1000 °C, a linear reaction rate constant of $k \approx 0.004$ nm/s was found for the (0001)-oriented sample. The rate constant was about a factor of three higher for the $(11\bar{2}0)$-oriented samples, and it was deduced that processes at the semicoherent $Al_2O_3/CoAl_2O_4$ interface are rate-limiting.

Kotula and Carter (1996) investigated the reaction kinetics of $NiAl_2O_4$ formation on (0001)-oriented corundum at 1100 °C. A 20 nm thick spinel seed layer was deposited between the reactants before to avoid nucleation problems. A comparatively slow linear growth rate of 0.0009 nm/s was observed. Extending this study, Kotula et al. (1998) found an interface-controlled reaction regime for this diffusion couple at temperatures between 1050 and 1150 °C, and an activation energy of 697 kJ/mol was reported. At 1050 °C, a rate of $k = 0.0001$ nm/s was obtained. The $\{1\bar{1}00\}$ and $\{1\bar{1}02\}$ orientations showed diffusion-controlled behaviour at the nanoscale. They attributed this difference to interfacial coherency.

Pin et al. (2013, 2013b) studied the reaction $Al_2O_3 + ZnO \longrightarrow ZnAl_2O_4$, investigating the role of the crystallographic orientation on the reactivity. Using a (0001)-oriented corundum single crystal, they found an interface-controlled reaction regime, a linear growth rate of $k = 0.048 \pm 0.001\,nm/s$ and an induction period of about 13 minutes for the onset of growth (Pin et al. 2013b). Using a $(11\bar{2}0)$-oriented corundum single crystal, the growth rate was about four times slower (Pin et al. 2013).

From all the studies mentioned above, it can be seen that no experiments were conducted at temperatures as low as 800 °C and very short run durations in combination with an *in-situ* monitoring of growth using synchrotron X-ray diffraction.

1.4 Rate Laws of Solid-State Reactions

The reaction rate of thin film solid-state reactions such as the spinel-forming one is determined by two different processes: (i) the reaction processes at both reaction fronts and (ii) the diffusion of particles across the reaction layer formed (Sieber et al., 1997b). Following Schmalzried (1981, 1995), particles will be transported over the phase boundaries and through the spinel reaction layer during the course of the experiment. The overall driving force for the reaction is the difference in Gibbs energy between the reactants and the reaction product. When atomic particles attempt to cross a phase boundary, they encounter a resistance. In order that a particle flux can be maintained, a discontinuity in the activity of the components must therefore occur. As the thickness of the spinel layer increases, the resistance to diffusion of the reaction layer increases relative to the resistance of the phase boundaries. Finally, if the phase boundary resistance can be neglected relative to the diffusional resistance, then a state of local thermodynamic equilibrium will be attained at the phase boundaries, and the discontinuity in activity of the components disappears. For oxide spinel formation, this state is reached when the reaction layer has a thickness Δx of roughly $1\,\mu m$ at the usual experimental temperatures of 1200 °C. A parabolic rate law is now observed in the form

$$\Delta x^2 \;=\; 2\,\overline{k}\,t \tag{1.7}$$

where $\overline{k}$ is the parabolic reaction rate constant. This constant shows Arrhenius behaviour, i.e. the spinel formation is a thermally activated process:

$$\overline{k} \;=\; k_0 \cdot e^{-\frac{E_a}{R\,T}} \tag{1.8}$$

where the pre-exponential factor k_0 is a constant, E_a is the activation energy for spinel formation and R is the gas constant.

As long as the spinel layer is thin, the diffusive mass transfer over short distances is very efficient and rather the reaction processes on both sides of the growing spinel layer are rate-limiting than the long-range diffusion of the Al_2O_3 and MgO components across the layer (Götze et al., 2014). The interfacial reaction in spinel-forming systems consists of a number of steps (Schmalzried, 1978b; cited in Ghigna et al., 2011):

- Cations diffuse to the interface
- Cations cross the interface
- Cations supersaturate with respect to the reactant
- Cations redistribute in the event that they relax into the proper sublattice
- 'Precipitation' to form the product

Simultaneously, the anions have to rearrange in order to accommodate the lattice mismatch, and the misfit-accommodating dislocation network has to move either by glide or climb (Graff et al., 1998). The structure of an interface is determined by the two adjacent phases. If these phases do not change during the reaction, except to alter their dimensions, the resistance of the phase boundary to the passage of particles will be constant, and a linear growth law in the form

$$\Delta x \;=\; k\,t \tag{1.9}$$

can be observed as long as the interface reaction is rate-determining (Schmalzried, 1981), i.e. the kinetics are at first interface-controlled. However, with increasing layer thickness, the distances over which transport must occur become longer. Diffusion therefore becomes successively less efficient and eventually becomes rate-limiting. The transition between interface reaction control and diffusion control is gradual. At which layer thickness the transition occurs, depends on the relative ease of the interface reactions and the long-range diffusion of the diffusing species (Götze et al., 2014).

As the linear growth behavior can be observed only at the earliest stages of the reaction, i.e. in nanoscale reaction layers, it is usually hard to observe; however, using diverse analytical methods, an interface-controlled reaction regime for various spinels was reported by e.g. Duckwitz and Schmalzried (1971) as well as Pin et al. (2013, 2013b) for the growth of $ZnAl_2O_4$, He and Becker (1997) for $CoAl_2O_4$ and Kotula et al. (1998) for $NiAl_2O_4$.

The periclase/spinel phase boundary is coherent as the fcc oxygen sublattice of periclase is transformed into the fcc oxygen sublattice of spinel. On the other hand, the corundum/spinel phase boundary is regarded as semi-coherent as corundum possesses an approximately hexagonal close-packed (hcp) oxygen sublattice, meaning that both the cation and anion sublattices have to be reconstructed, and bundles of partial dislocations that transform the hcp oxygen structure into the fcc structure of spinel have to move in the interface during the transformation (Schmalzried, 1978). The propagation of one interface is kinematically coupled to the propagation of the other interface, and the semi-coherent corundum/spinel phase boundary was found to be rate-limiting in the interface-controlled reaction regime (e.g. He and Becker, 1997; Kotula et al., 1998; Pin et al., 2013b).

2 Materials and Methods

2.1 Substrates

Corundum as well as periclase single crystal substrates were acquired from manufacturer Korth Kristalle GmbH (Kiel, Germany). The reaction surface was classified as 'epi-ready', meaning that this surface is ultra-high polished and that no further treatment is necessary for the deposition of epitaxial thin films. Indeed, atomic force microscopy (AFM) measurements confirmed that the surface roughness R_a, calculated as the arithmetic mean of the absolute measurement values, is in the nanometer range. Dimensions of the substrates were $10 \times 10 \times 1.5 \pm 0.1\,\mathrm{mm}^3$. A specimen can be seen in Figure 2.6a on page 25.

2.1.1 Corundum

Corundum (also designated as α–Al_2O_3) crystallizes in the trigonal crystal system with cell dimensions $a_0 = 5.13\,\text{Å}$ and $\alpha = 55.28°$ ($Z = 2$); using the hexagonal crystallographic coordination system, cell dimensions are $a_0 = 4.76\,\text{Å}$ and $c_0 = 12.99\,\text{Å}$ ($Z = 6$) (Lee and Lagerlof, 1985). Its space group is $R\bar{3}c$ (number 167). The oxygen ions form an almost hcp anion sublattice, and the aluminum ions occupy in an ordered array only two-thirds of the available octahedral interstices. Due to this symmetry reduction, corundum is trigonal and not hexagonal. The description using hexagonal axes leads to a 30° rotation of the a-axes about the c-axis when compared to an hcp metal; the close-packed directions in the anion sublattice thus lie along $<10\bar{1}0>$ whereas in hcp metals they lie along $<11\bar{2}0>$ (Lee and Lagerlof, 1985).

Considering the crystal structure in more detail, the unoccupied octahedra lead to a slight displacement of the aluminum cations along the [0001] direction towards the empty octahedral sites, and this displacement is accompanied by a distortion of the oxygen sublattice (Levin and Brandon, 1998). The oxygen sublattice is thus only pseudo-hexagonal close-packed.

Synthetic corundum is also often designated as sapphire in the literature. This designation should not be confused with the naturally occurring blue variety of corundum which is also called sapphire; this variety contains titanium (Ti^{4+}) and iron (Fe^{2+}) in the crystal lattice (Carter and Norton, 2007).

The orientation of the corundum substrates is (0001). A schematic of the (0001) face is presented in Figure 2.1. The (0001) surface of corundum is one of the most widely used

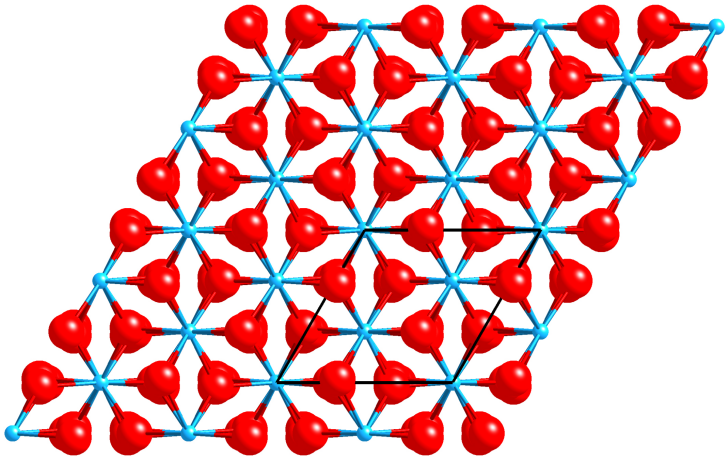

Figure 2.1:
Schematic of the corundum crystal structure. (0001) face. Aluminum atoms (blue spheres) occupy two-thirds of the octahedral interstices formed by the pseudo-hexagonal close-packed oxygen sublattice (red spheres). A unit cell is marked by a solid black line in the lower right corner.

substrates for the (epitaxial) growth of metal, semi-conductor and high-temperature superconductor thin films (Barbier et al., 2001). This is the orientation in which the oxygen anions are hexagonally arranged in plan view, i.e. each oxygen ion in this plane is surrounded by six neighbors. In the literature, this orientation is also designated as the *c*-plane orientation of corundum as this is the crystallographic plane perpendicular to the c-axis. A specimen with this orientation is then often abbreviated as *c*-plane corundum. Similar denotations are *a*-plane and *m*-plane for the prism planes $\{11\bar{2}0\}$ and $\{10\bar{1}0\}$, respectively, and *r*-plane for the rhombohedral planes $\{1\bar{1}02\}$ (e.g. Stampe et al., 1999). The (0001) face is also the basal plane of corundum.

The orientation was verified by a θ/θ X-ray diffraction measurement using a lab diffractometer. However, using the high photon flux at the synchrotron beamlines and the possibility to vary ω ($\equiv \theta$, cf. Fig. 2.8 on page 28), it was found that the substrates had a slight miscut from the exact (0001) orientation; the miscut varied between 0.2 and 1°.

2.1.2 Periclase

Periclase (MgO) crystallizes in the rock salt structure type, i.e. in the cubic crystal system and space group $Fm\bar{3}m$ (number 225). The lattice constant is $a_0 = 4.21$ Å ($Z = 4$) (Hazen, 1976).

In the crystal structure, both ions are arranged face-centered cubic and one ion occupies the octahedral interstices formed by the respective other ion. In other words, both fcc sublattices interprenetrate themselves, and the respective displacement is $\frac{1}{2}<001>$ or equally $\frac{1}{2}<111>$ (Carter and Norton, 2007).

The orientation of the periclase substrates is (111). Similar to the corundum substrates, this is the orientation where the oxygen ions are in a close-packed arrangement in plan view; however, the stacking sequence in [111] is ABCABC... in fcc structures, meaning that there are three distinct planes of close-packed oxygen layers that alternate periodically whereas in hcp structures the sequence in [0001] is ABABAB... with only

two distinct alternating planes. A schematic of the (111) face of periclase is presented in Figure 2.2.

Similar to the corundum substrates, it was found at the synchrotron beamlines that these single crystals had a miscut; the orientation deviated up to 6° from the exact (111) orientation (most samples had a miscut of about 3°). Due to this significant off-orientation, the 111 Bragg peak was only barely visible in laboratory θ/θ scans.

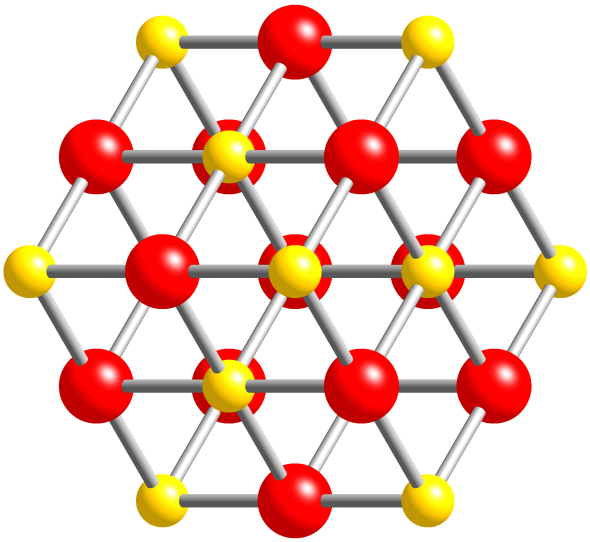

Figure 2.2:
Schematic of the periclase crystal structure. (111) face of the unit cell. Oxygen atoms in red spheres and magnesium atoms in yellow spheres; both ions form fcc sublattices, and one ion occupies the octahedral interstices formed by the respective other ion.

2.2 Pulsed Laser Deposition of Thin Films

Many different methods for the deposition of thin films exist. Overviews of the various techniques can be found in e.g. Wasa et al. (2004) and Martin (2010); an introduction to the pulsed laser deposition (PLD) technique can be found in Eason (2007). PLD belongs to the physical vapor deposition (PVD) class of thin film deposition techniques; the other broad category is chemical vapor deposition (CVD) (Wasa et al., 2004). Every PVD process can be defined by three basic steps (Martin, 2010):

1. Creation of vapor-phase species
2. Transport of the species from source to substrate
3. Film growth on the substrate

A schematic of these steps in PLD is presented in Figure 2.3. To be more precise, the following processes succeed in this particular technique: firstly, high-power laser pulses ablate a small amount of material from a solid target when a focused laser beam is absorbed by a small area of the target surface. Chemical bonds of the molecules within the solid target are broken and the material is evaporated. The evaporated material is

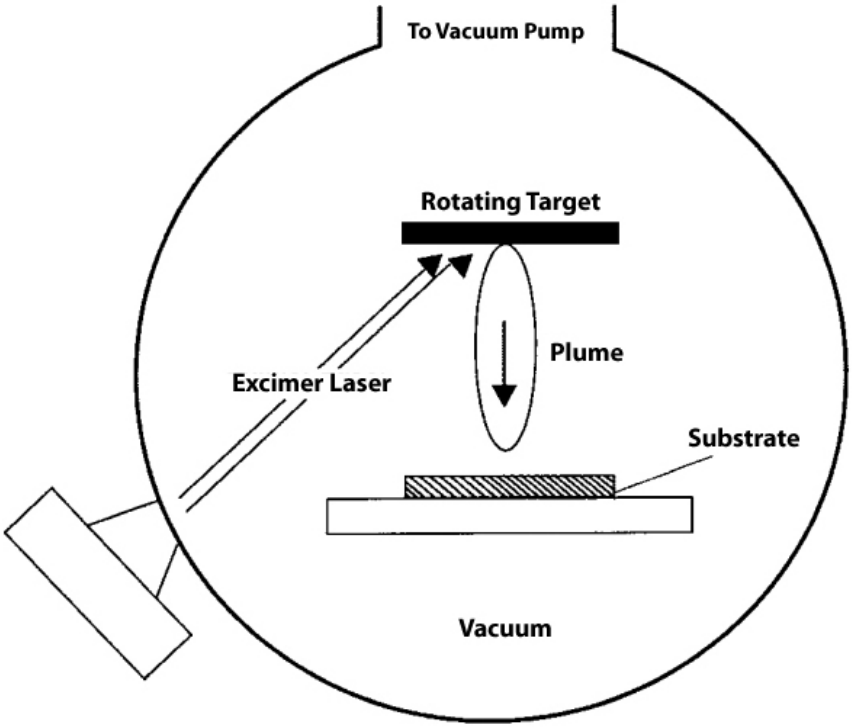

Figure 2.3: Schematic of the basic processes in PLD, i.e. ablation of the target material by high-power laser pulses, transport of the ablated material towards the substrate and film growth on the substrate. Modified after Wasa et al. (2004).

comprised of ions, molecules, neutral atoms and free radicals in their ground and excited states. This further absorbs a large amount of energy from the laser beam, producing an expansion of hot plasma. The plasma plume is then expanded away from the target with a velocity distribution of different particles in the forward direction. Finally, the ablated species condense on a substrate, placed at an angle opposite to the target, forming a thin film (paragraph after Shah et al., 2010). Due to the high energy of the laser pulses and the resulting high temperatures at the target surface, it is assumed that all of the target constituents are evaporated simultaneously (Shaginyan, 2001). The high degree of stoichiometric transfer from target to substrate is presumably the main reason for the widespread application of PLD (Schou, 2009).

The main disadvantages of PLD are that, at present, this technique provides a limited area of uniform film thickness, and microsized globules or particles can be ejected from the target (Wasa et al., 2004; see also Dohmen et al., 2002). Shaginyan (2001) highlights the problem of possible texturing effects of the target during irradiation: due to shadowing effects, features at the target surface are enhanced via cone formation when the target is irradiated. This cone formation leads to a shift in the angle of the plasma towards the laser beam. Because the composition and the thickness of the film are opti-

mal when the film is deposited from the peak of the plasma plume, a shift of the plume direction can be a serious problem for the deposition of stoichiometric films.

These three problems, i.e. non-uniform layer thicknesses, particles on the substrate surface and cone formation at the target surface, were noticed during or after the deposition process; their handling is discussed in the following two subsections.

2.2.1 Procedure of Pulsed Laser Deposition

Thin films of this study were fabricated via PLD in cooperation with Dr. R. Dohmen from the Mineralogy-Petrology group of the Faculty of Geosciences at the Ruhr-Universität Bochum, Germany. The reference paper for the PLD setup in Bochum is Dohmen et al. (2002). Their system employs an excimer laser (Model LPX305i from manufacturer Lamda Physik). An ArF gas mixture was used which results in a laser wavelength of 193 nm. This gas mixture is consumed steadily, and, as a consequence, pulse energies are not constant but decrease with time. The basic laser and deposition processing parameters are presented in Table 2.1. The laser beam passes an aperture, a quartz focussing lense and a fluorite window to the vacuum chamber before hitting the target. Thus, the actual energy on the target is reduced to about 10-50 mJ/pulse, and the laser fluence amounts to 1-5 J/cm^2. Figure 2.4 shows the inside of the vacuum chamber with positions of targets and substrates.

Prior to thin film deposition, the substrates were cleaned by sonication. By this treatment, a faint coating could be removed from the polished surface of the periclase substrates. This coating is probably brucite that formed according to the reaction $MgO + H_2O \longrightarrow Mg(OH)_2$. Such nonintentional hydration of periclase substrates was also reported by e.g. Blum (1997) and Lee et al. (2003). Especially (111)-oriented periclase crystals tend to react easily with moisture in the air (Lee et al., 2003; Sutcu et al., 2009).

Table 2.1: Laser and deposition processing parameters.

Parameter	Value
Laser	ArF
Laser wavelength	193 nm
Pulse energy	170-360 mJ
Pulse duration	30 ns
Pulse rate	10 Hz
Laser spot size	0.5 × 2 mm^2
Laser fluence	1-5 J/cm^2
Ambient medium	Air/vacuum ($\leq 10^{-5}$ mbar)
Target-to-substrate distance	≈3 cm

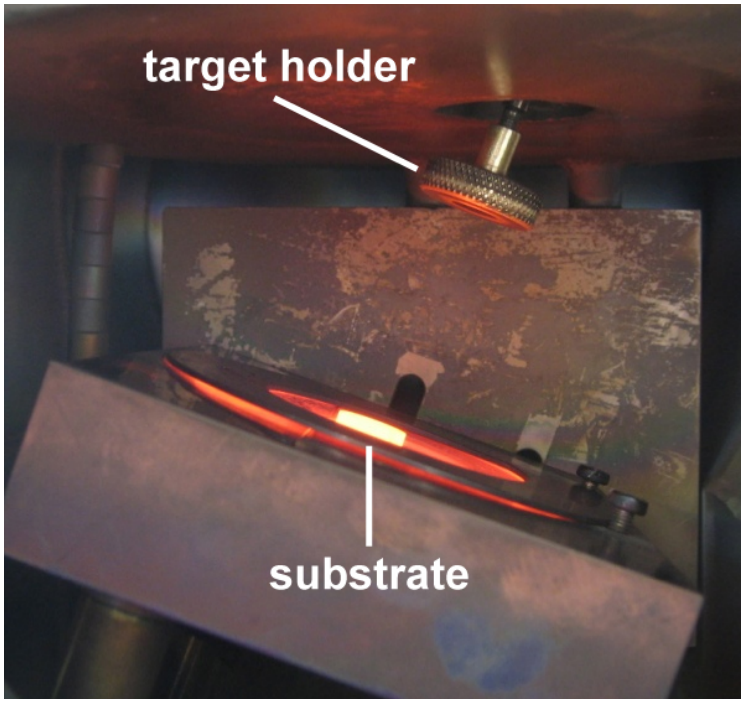

Figure 2.4:
PLD setup in Bochum showing positions of targets and substrates inside the vacuum chamber. Targets are placed inside the rotating target holder. The target-to-substrate distance is about 3 cm. The substrate is glowing due to a pre-anneal using a SiC heater that is situated beneath the specimen.

After sonication, the reaction surfaces were additionally cleaned by rinsing in ethanol. To evaporate adsorbed materials from the surface, in particular water, the substrates were then heated for at least 10 minutes inside the vacuum chamber at about 400 °C using a SiC heater that is placed directly beneath the substrates (a glowing substrate can be seen in Figure 2.4). After turning off the heater, additional 10 minutes were given for the cooling of the samples to prohibit the spinel-forming reaction that may take place during the deposition of the reactant layer. As a consequence of the cooling, reactant layers were deposited amorphous. During these 20 minutes of pretreatment, a high vacuum background inside the deposition chamber could be established by using a turbo pump.

For the crystallization of the amorphous $MgAl_2O_4$ layers in the two experimental setups with a spinel seed layer between the reactants (the three-layer setups, cf. Fig. 2.5 on the characterization of the starting materials and section 3.1.1 on all experimental setups), samples were annealed for 5 minutes at 1000 °C in an external furnace prior deposition of the reactant layer. It was always tried to deposit the seed layer having a thickness of 50 nm. Layer thicknesses could be estimated on-site using the formula (R. Dohmen, personal communication)

$$x \approx \frac{\Gamma}{4\,n} \tag{2.1}$$

where Γ is the optical path difference, and n is the index of refraction of the deposited mineral. The optical path difference was obtained from the Michel-Lévy interference colour chart by taking the respective value for the maximum interference colour on the

coated substrate. In many cases, the non-uniform thickness of the deposited thin film could be deduced on-site from different interference colours on the coated samples, indicating that a maximum layer thickness is followed by successively decreasing thicknesses. The area with the maximum film thickness had usually a rather oval shape and covered at most 40 % of the sample surface. The distribution of material deposited from the plume is often found to be symmetric with respect to the target surface normal, and the distribution can be described in terms of a $\cos^m(\theta)$ distribution where m can vary from ≈4 to 30 (Norton, 2007). Using this PLD setup, Dohmen et al. (2002) found m = 23 for an olivine film on a silicon wafer, and the area with uniform film thickness was circular with a diameter of about 4 mm. By adjusting slightly the quartz focussing lense that is placed in the laser path, it is possible to minimize thickness differences and also to circumvent the cone formation at the target because then a different area is hit at the target and the path of the plasma plume has a slight offset.

It can be concluded that these substrates with a surface area of 1 cm^2 were too large to deposit films having a uniform thickness. On the other hand, a uniform layer thickness was not essential for the *in-situ* experiments because the synchrotron beam illuminated only a small area of the samples (cf. sections 2.3.2 and 2.3.3 on the beamlines), and, above all, the samples were needed in that size to fit into the heating attachment (section 2.3.1). It was always tried to deposit the maximum thickness in the center of the sample where subsequently also the synchrotron beam hit the sample and foils for transmission electron microscopy (TEM) analysis were lifted out by the focused ion beam (FIB) technique.

2.2.2 Target Materials

Commercially available Al_2O_3 and MgO powders were used for the synthesis of the targets. Pellets of the oxides were fabricated by compacting the powders using a manual hydraulic laboratory press and subsequent sintering at high temperatures. To be sintering effective, i.e. to enhance diffusion and eliminate porosity, it is recommended to anneal green bodies at about 70 to 80 % of their respective melting points in Kelvin (e.g. Salmang and Scholze, 2006). Well compacted targets may be required to reduce the ejection of microsized globules or particles that may deposit on the substrate as well. Melting points of corundum, periclase and spinel are 2055, 2825 and 2105 °C (Alper et al., 1962; Hallstedt, 1992; cf. phase diagram in Fig. 1.1 on page 3), respectively, resulting in sintering temperatures of about 1357, 1896 and 1392 °C, respectively. Various Al_2O_3 and $MgAl_2O_4$ pellets were annealed in platinum crucibles over night from 1350 to 1500 °C in air. MgO pellets could be sintered only at 1650 °C. However, eventually periclase single crystals served as targets for the deposition of MgO. Test runs using silicon wafers as substrate showed that the sputter yield was slightly better and less particles on the surface appeared using these single crystals. On the other hand, for Al_2O_3, the better sputter yield using pellets as targets and not single crystals was preferred over the existence of some more particles.

Spinel pellets were synthesized by mixing the Al_2O_3 and MgO powders in stoichiometric proportions. Prior to mixing, the powders were dried for several hours at 150 °C to evaporate hygroscopic water. Especially the MgO powder had remarkable weight losses of up to 8 %. After the first deposition runs using pellets fabricated this way, grazing incidence X-ray diffraction (GIXRD) measurements demonstrated that only spinel crystallized after annealing the samples at 1000 °C.[1] Because only a very small amount of the material is ablated during each run, these proven pellets could be used subsequently for all remaining samples which were composed of a spinel seed layer between substrate and reactant layer.

2.2.3 Characterization of Deposited Thin Films

By now, plenty techniques are available, which generally make use of incident photons, electrons or ions, to analyze the various properties of thin films. An overview of these techniques can be found in e.g. Baer and Thevuthasan (2010), and an overview of thin film properties that are most commonly tested can be found in e.g. Mattox (2010).

For this study, it was important to know how much material was transferred during PLD runs so that the deposition time could be adjusted if necessary. Using Equation 2.1, the layer thickness could be estimated, but eventually TEM was employed to determine absolute thicknesses. For each setup, one specimen served as a representative for the characterization of the starting materials; thus, the actual thickness will vary among the samples of a specific setup as the pulse energies steadily decrease during PLD. TEM bright field images of the four different experimental setups are presented in Figure 2.5.[2]

Calculated deposition rates of the thin films in Figure 2.5 are presented in Table 2.2. It can be seen that the deposition rates for MgO were poor. Subimages (a) and (c) of Figure 2.5 show that the MgO layers are comparatively narrow despite deposition times were longer than 2 hours in each case. This poor sputter yield is due to MgO having a wide optical bandgap; thus, the ablation efficiency from ceramic or single crystal MgO targets is low for commercially available pulsed laser wavelengths (Norton, 2007). The sputter yield was better for Al_2O_3 and especially for $MgAl_2O_4$.

Adhesion is a fundamental requirement of any substrate/film system (Mattox, 2010). In this study, the adhesion of the deposited thin films to the substrates was always excellent. As it can be seen in Figure 2.5 and especially in additional high-resolution TEM images, no porosity or voids are present at the substrate/thin film interface.

Before annealing the samples, preliminary measurements at the synchrotron beamlines demonstrated that no spinel was formed during PLD, i.e. no interdiffusion and reaction of the materials occurred. Thus, the interface may be categorized as abrupt.

[1] More information on the GIXRD technique can be found in section 2.5.2, and results of measurements are presented in section 3.6

[2] Not shown are the one-layer setups in which only a spinel layer was deposited on top of the substrates.

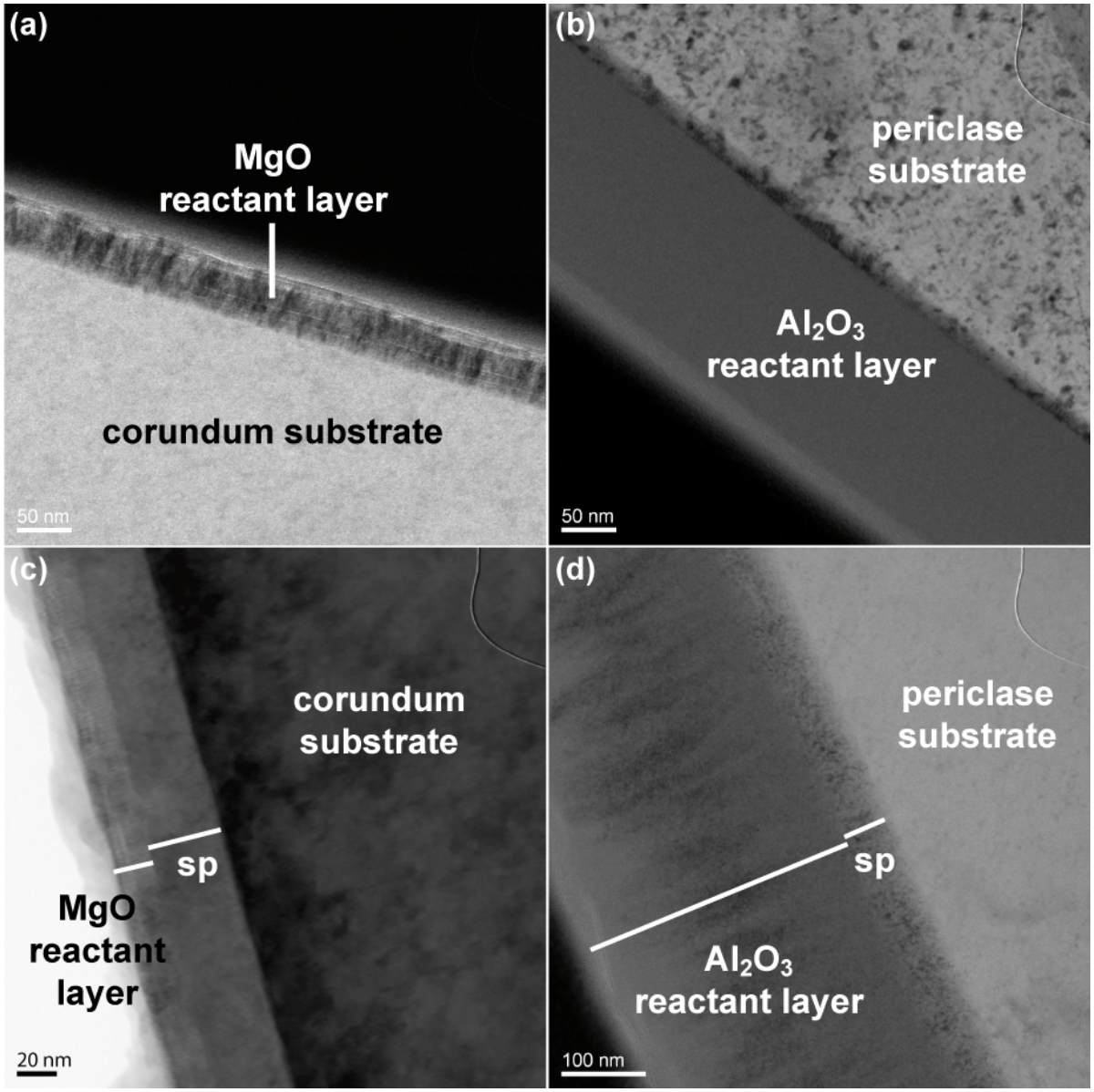

Figure 2.5: Cross-sectional TEM bright field images of the starting materials. (a) Corundum substrates two-layer setup. (b) Periclase substrates two-layer setup. (c) Corundum substrates three-layer setup. (d) Periclase substrates three-layer setup. A spinel seed layer (sp), about 50 nm in thickness, is present between substrates and reactant layers in the three-layer setups. Note scale bars in the lower left corners of the images.

Table 2.2: Deposition rates for the thin films presented in Figure 2.5.

Subimage	Thin film	Deposition time [min]	Deposition rate [nm/min]	Pulse energy [mJ]
(a)	MgO	150	0.33	256
(b)	Al_2O_3	120	1.42	172
(c)	spinel	10	4	336
(c)	MgO	135	0.15	288
(d)	spinel	10	5	352
(d)	Al_2O_3	120	2.58	344

2.3 In-situ Experiments

In the subsections of this section, informations about the heating attachment and the two synchrotron beamlines that were used for the *in-situ* experiments can be found. Additionally, it is presented in detail how the *in-situ* experiments were carried out.

2.3.1 Heating Attachment

Samples were annealed and investigated *in-situ* using the heating attachment 'DHS 1100 Domed Hot Stage' in combination with the 'TCU 200 Temperature Control Unit' (DHS and TCU, respectively, in the following) from manufacturer Anton Paar GmbH.[3] The DHS is designed for conventional four-circle X-ray diffractometers to conduct *in-situ* X-ray diffraction experiments in reflection geometry from 25 to 1100 °C with very fast heating and cooling rates of up to 300 K/min, respectively. The main functions of the TCU are:

- Defining the target temperature as well as heating and cooling rates for the DHS by means of an Eurotherm controller
- Providing controlled power to the heater of the DHS to regulate the heating and cooling of the sample holder
- Displaying the sample holder temperature and providing it for readout with a computer
- Turning the compressed-air cooling of the DHS on and off, depending on sample holder temperature
- Monitoring the status of DHS and preventing operation if the instrument is not in safe condition

[3]Informations in this chapter stem to a large part from the instruction manuals for both devices (Paar, 2011; Paar, 2011b). A predecessor of the DHS is described in Resel et al. (2003).

A close-up of the DHS is presented in Figure 2.6a, and the complete setup (DHS, TCU plus an air service unit) is presented in Figure 2.6b. The Eurotherm controller (type Eurotherm 2604) inside the TCU can be controlled via an external computer using a RS 232 interface. An air service unit was used for the cooling of the DHS at temperatures above 200 °C. This unit regulates the compressed air (inlet pressure should be between 2 and 4 bar) and removes particles out of the air by means of a fine filter (5 μm) and a micro filter (0.01 μm). An X-ray transparent graphite dome has to be mounted onto the DHS at temperatures above 200 °C (the domed DHS can be seen in Figure 2.6b). The dome prevents enhanced and irregular heat dissipation and provides, in combination with the compressed air, a homogeneous cooling of the sample stage. By using the dome, samples can be investigated also in inert gas or in vacuum, but all experiments of this study were conducted in air. The X-ray transmission of the graphite dome amounts to 65 % for CuK$\overline{\alpha}$ radiation (primary plus diffracted beam).

Samples were heated from beneath the sample plate by a Kanthal heater. The sample plate is about 1 mm thick and is made up of aluminum nitride. The excellent thermal conductivity of this material guarantees a high temperature uniformity across the heating

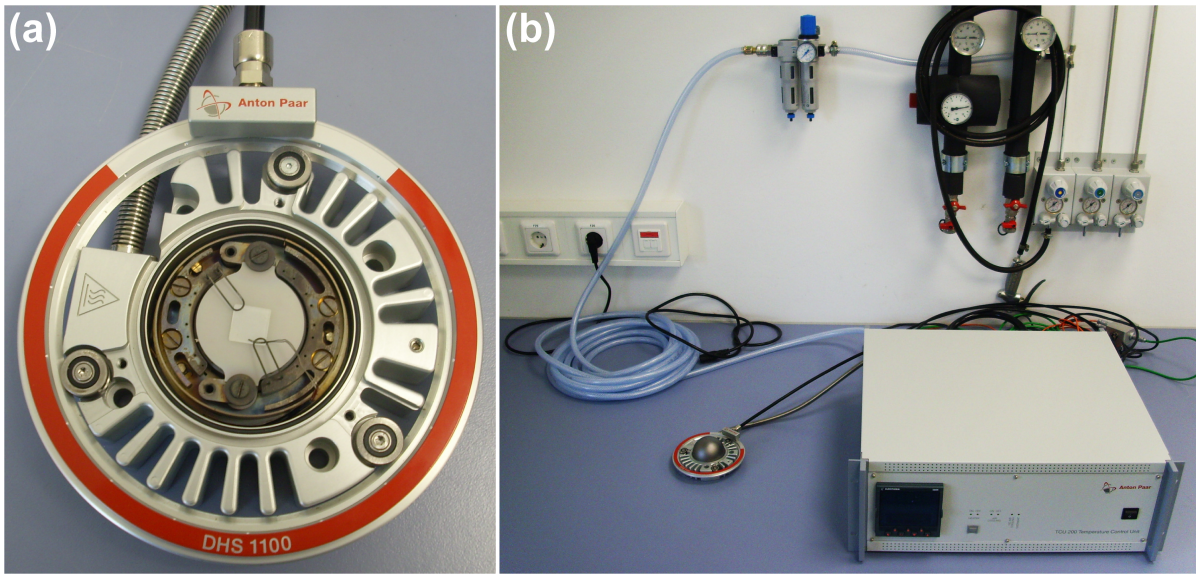

Figure 2.6: Heating attachment and temperature control unit for *in-situ* X-ray diffraction experiments. (a) Close-up of the heating attachment. In the middle of the sample plate a typical substrate (edge lenghts = 1 cm) can be seen that is fixed onto the device via springs. On the lower spring a thermocouple can be seen that measured the temperature at the surface of the samples. (b) The complete setup with the TCU in the lower right corner, the domed heating attachment in the lower left corner and the air service unit in the middle at the top (the larger air service unit in the upper right corner belongs to the lab and delivered the compressed air for test runs).

plate. The temperature is measured by a Pt-Pt10Rh (type S) thermocouple that is located below the center of the heating plate. The Eurotherm controller inside the TCU converts the signal from this thermocouple into a temperature readout and provides subsequently the correct heating current to the DHS. As this is the temperature of the sample plate (T_{DHS} in the following), the actual temperature at the sample surface, where the spinel-forming reaction takes place, is different by some centigrades. The deviation depends on the thickness and thermal conductivity of the substrate, on the thermal contact between sample stage and sample and on the sample environment (gas or vacuum). To measure the temperature at the surface of the samples, a special second (type K) thermocouple was installed in our DHS. Consequently, the TCU was also modified by the manufacturer to display the temperatures of both thermocouples (but the target temperature for a specific experiment that has to be defined via the TCU is still that of the sample plate, i.e. T_{DHS}). The second thermocouple was clamped onto the substrates as it can be seen in Figure 2.6a.

The temperature measured by the second thermocouple (T_{sub} in the following) will also depend on the quality of its mechanical contact to the substrate. In general, it might show lower temperatures than the actual temperature at the surface because the tip of the thermocouple cannot be clamped too firmly onto the substrates. This part is prone to breakdown and has to be handled with care. However, to calibrate the second thermocouple, the temperature difference between the thermocouples was monitored during several test runs before the actual *in-situ* experiments. The offsets were recorded at temperature steps of 100 K beginning at $T_{DHS} = 500\,^{\circ}C$ where the deviation started to be substantial. Once the desired T_{DHS} is reached, T_{sub} remains stable as well. In Figure 2.7 are the arithmetic means along with $1\,\sigma$ uncertainties (which are about ± 10 K for each temperature) of measured T_{sub} plotted against the defined T_{DHS}. It can be

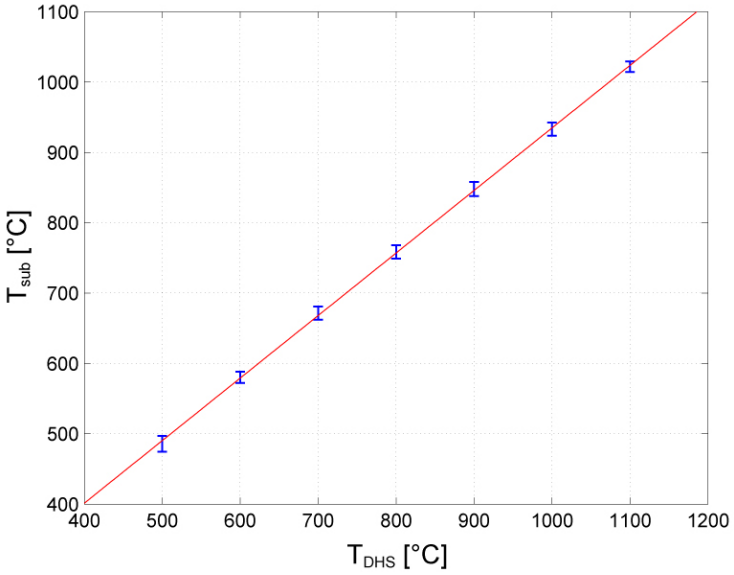

Figure 2.7: Temperature deviations between the thermocouples of the DHS. Temperatures of T_{sub} plotted against the defined T_{DHS}. Error bars indicate $1\,\sigma$ uncertainties of T_{sub} measurements obtained from various test runs. The red line is a linear fit to the data.

seen that the deviation increases with increasing T_{DHS}. As an example, the offset is about 78 K for the maximum temperature of the DHS, i.e. $T_{sub} = 1022 \pm 10$ °C when $T_{DHS} = 1100$ °C. The data is fitted linearly in Figure 2.7; the equation obtained reads

$$T_{sub} = 0.89 \cdot T_{DHS} + 45.32 \tag{2.2}$$

For the *in-situ* experiments, this equation was used to obtain a certain T_{sub} instead of adjusting this temperature for each experiment because, as stated before, T_{sub} depends on the respective quality of the mechanical contact between thermocouple and substrate. Using this procedure, all samples of a specific temperature series had the same T_{DHS}, and the real temperature at their surface may differ only due to sample thickness variations (sample thicknesses were 1.5 ± 0.1 mm, cf. section 2.1).

2.3.2 EDDI Beamline

EDDI is an acronym for *E*nergy *D*ispersive *DI*ffraction. The reference paper for the beamline, which is situated at the synchrotron radiation facility BESSY II in Berlin, Germany, is Genzel et al. (2007). Among several other papers, valuable information on the layout of the beamline, its detector system and the data evaluation package that EDDI provides for data pre- and post-processing can also be found in Genzel et al. (2006), Denks and Genzel (2007) and Apel et al. (2011).

In the energy-dispersive mode of diffraction, it is possible to obtain complete diffraction spectra with a multitude of simultaneously recorded reflections on a short time scale of about 10 seconds per spectrum in a fixed scattering arrangement; this makes it an ideal tool for the *in-situ* characterization of growing thin films with respect to phase composition, crystallographic texture and film microstructure (Genzel et al., 2007). In contrast to the angle-dispersive mode of diffraction, in which a monochromatic beam is used, a polychromatic beam illuminates the sample in the energy-dispersive mode and the energies of the diffracted photons are measured. Detected photons had energies from about 2 to 130 keV, corresponding to wavelengths of roughly 1 nm to 10 pm.

2.3.2.1 Layout of the Beamline

A schematic of the basic beamline components is presented in Figure 2.8. The photon source of the beamline is a superconducting 7-T multipole wiggler, and the beamline makes direct use of the white synchrotron beam as it is provided by the wiggler (Apel et al., 2011). By means of the wiggler, the hard X-rays up to 100 keV and more can be generated (Spieß et al., 2009). In the primary beam path, the beam is collimated in both, the equatorial (i.e. vertical) and the axial (i.e. horizontal) direction, by the white beam mask (an absorber mask) and the slit systems S1 and S2 whereas the aluminum filter system attenuates photons with energies < 10 keV which would introduce heat into the sample (Genzel et al., 2006). The mask and slit systems reduced the beam cross-section

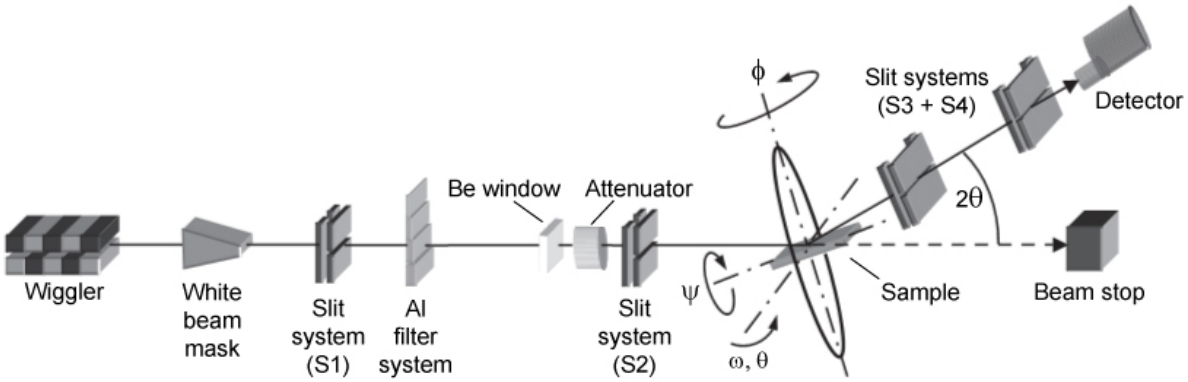

Figure 2.8: Schematic layout of the main EDDI beamline components. Modified after Genzel et al. (2007).

on the sample to $0.5 \times 0.5\,\mathrm{mm}^2$ (M. Klaus, personal communication). Additional attenuation of the photon flux can be attained by placing sheets or pieces of graphite, copper, aluminum or iron into the beam between the beryllium window, which completes the vacuum section of the beamline, and the slit system S2 (Genzel et al., 2007). Without attenuators in the beam path, the intensity is about 10^{12} Photons / s mm^2 at 10 keV and 10^{10} Photons / s mm^2 at 100 keV for a storage current of 250 mA (Genzel et al., 2007).

Inside the experimental hutch, the DHS was mounted onto the EDDI diffractometer, which is placed 30 m behind the wiggler. It is a four-circle diffractometer, thus also capable of texture measurements and X-ray stress analysis (XSA). In the diffractometer system, a x-y-z translation table is integrated which was used at the beginning of the installation to align the DHS so that the beam hits the center of the heating plate. Exact height adjustment for each sample was later accomplished by means of a laser system and a CCD camera. The status of both, the DHS and the TCU inside the hutch, was monitored by several webcams.

The diffracted beam is collimated equatorially and axially by the slit systems S3 and S4 to $0.03 \times 5\,\mathrm{mm}^2$, respectively (M. Klaus, personal communication), before the photons reach the detector. The detector system consists of a semiconducting LEGe (*L*ow *E*nergy *Ge*rmanium) detector with a detached transistor reset preamplifier, a digital signal processor and a multi channel analyzer (Genzel et al., 2007). The multi channel analyzer allows the differentiation of photon energies in about 16 000 channels. The correlation between channels and the energy scale is described by a 2nd order polynomial calibration function (Genzel et al., 2007).

2.3.2.2 Procedure of *in-situ* Experiments

At this beamline, only *in-situ* X-ray diffraction experiments in reflection geometry were carried out. The diffraction angle 2θ was always 12°. Thus, ω was principally 6°, but corrections were necessary that accounted for the variable miscut of the substrates

(cf. sections 2.1.1 and 2.1.2). The off-orientation was determined before each experiment by varying ω to bring the sample in maximum reflection position. Due to the sample tilt of nominally 6°, the footprint of the beam on the sample is enlarged to a length of $0.5\,\mathrm{mm}/\sin(6^\circ) = 4.78\,\mathrm{mm}$.

Via the RS 232 interface and the Modbus protocol, the TCU was remote-controlled by an external EDDI computer, but the temperature set point, i.e. the target temperature, as well as the heating and cooling rates were still defined in the TCU before an experiment (the latter were defined only once as 200 K/min). The computer was used to start an experiment with these predefined parameters and to end an experiment as the run duration cannot be programmed in this type of Eurotherm controller. Additionally, by interfacing the computer, the temperatures of both thermocouples were recorded simultaneously and were assigned to the respective spectrum. Also the respective values of ω, 2θ, ϕ, ψ, the sample height z, the ring current and the counting time, among others, are registered in each data file.

To obtain evaluable peak resolutions, the counting time Δt for each spectrum was 300 seconds at target temperatures. Because very fast heating and cooling rates of 200 K/min were used, the counting time during the heating and cooling stages was 60 seconds per spectrum in most experiments so that the sudden appearance of a phase may have been monitored during this period.

During this beamtime, BESSY II was operated in decay mode, meaning that the ring current decreased steadily with time from a maximum ring current of 300 mA to a minimum of about 150 mA. New electrons had to be injected into the storage ring every 8 hours. During these injections, the beam shutter was closed and no spectra could be recorded so that every experiment was planned to end before a new injection.

To summarize, the prodecure during each experiment was as follows:

- Mounting the sample onto the DHS
- Height adjustment of the sample via a laser and CCD cameras
- Determining the miscut of the substrates
- Mounting the graphite dome onto the DHS
- Defining the temperature set point (the target temperature) in the TCU
- Closing the experimental hutch and opening the beam shutter
- Starting the experiment on the external EDDI computer
- Recording the diffraction spectra
- Stopping the experiment on the external EDDI computer
- Closing the beam shutter and opening the experimental hutch to dismount the sample

2.3.2.3 Signals in the Diffraction Spectra

In the energy-dispersive mode of diffraction, d_{hkl} values of phases are obtained using the energy-dispersive Bragg equation (e.g. Spieß et al., 2009):

$$d_{hkl} = \frac{h \cdot c}{2 \cdot sin\,\theta \cdot E_{hkl}} = const. \frac{1}{E_{hkl}} \tag{2.3}$$

where h = Planck's constant, c = velocity of light, E_{hkl} = energy of the diffracted photon. The diffraction angle 2θ is fixed during the experiment and was in all cases 12°. This equation can be derived from the well known Bragg's equation

$$\lambda \;=\; 2\,d \cdot sin\,\theta_B \tag{2.4}$$

by replacing the wavelength of a photon with its energy

$$E \;=\; h\frac{c}{\lambda} \tag{2.5}$$

Due to the fixed scattering arrangement, only the E_{hkl} of a peak in the diffraction spectrum has to be determined to obtain the respective d_{hkl} value, the remaining parameters are constant.

Besides the Bragg reflections of the substrate and the thin films, escape peaks from the LEGe detector and fluorescence lines may appear in the spectra. Escape peaks may emanate if the photon energy is above the K-edge energy of germanium ($E_K = 11.104\,keV$). For each Bragg peak at an energy E_{Bragg} exceeding E_K, two escape peaks are possible; they appear at energies $E_{esc\,alpha} = E_{Bragg} - 9.876\,keV$ and $E_{esc\,beta} = E_{Bragg} - 10.983\,keV$ (Apel et al., 2011). The process behind the generation of these peaks is fluorescence in the germanium detector crystal; a diffracted photon interacts with the crystal and loses energy by emitting an electron from the K-shell of germanium (Spieß et al., 2009). The subsequently detected photon has then an energy of either $E_{esc\,alpha}$ or $E_{esc\,beta}$ when the excited germanium atom emitted $K\alpha$ or $K\beta$ radiation, respectively. Thus, escape peaks have always lower intensities and lower energies than the Bragg peak they are associated with.

Both substrates usually generated esc_{alpha} peaks and sometimes also esc_{beta} peaks. Escape peaks from a (0001)-oriented corundum substrate and a (111)-oriented periclase substrate are depicted in the EDDI spectra presented in Figure 2.9. The thin films generated sometimes esc_{alpha} peaks but never distinct esc_{beta} peaks. In the following, escape peaks will be designated as *esc* in graphs presenting EDDI spectra.

Fluorescence lines were frequently observed from copper and zinc (pointing to brass in the beam path) and to a lesser degree from tungsten and lead (pointing to shielding components of the beamline). Additionally, in some experiments fluorescence from chromium, iron, cobalt, nickel, germanium and molybdenum was detected. All these lines were generated either from components of the beamline or from the fixing springs and the housing of the DHS. The springs and the housing are made up of Inconel (Paar, 2011) which is a nickel-chromium-cobalt alloy. Fluorescence lines will be denoted as *FL* in following graphs.

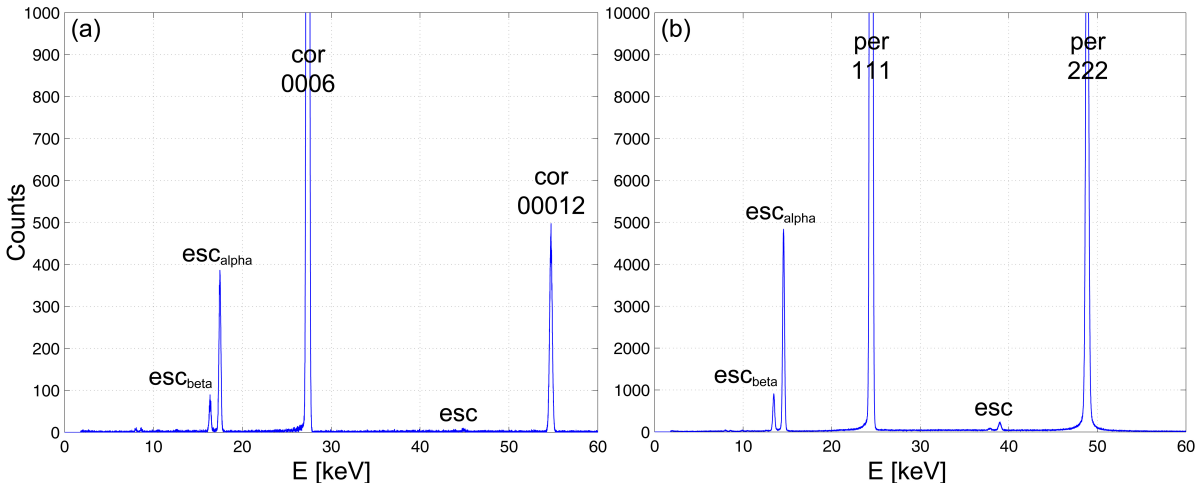

Figure 2.9: esc_{alpha} and esc_{beta} peaks appear at positions –9.88 and –10.98 keV from the substrate reflections, respectively. (a) Escape peaks from the 0006 reflection of corundum at 27.38 keV (T = 193 °C; Δt = 60 s). (b) Escape peaks from the 111 periclase reflection at 24.47 keV (T = 25 °C; Δt = 300 s).

2.3.2.4 Data Evaluation

The EDDI data processing concept is visualized in Genzel et al. (2006). The diffractometer and the detector system is controlled by the software package spec® which also reads in control variables such as the decreasing ring current and the wiggler field which are needed in the data evaluation process for spectra calibration (Genzel et al., 2007). For data pre- and post-processing, EDDI provides a MATHEMATICA® software package that converts spec-files into dat-files. Using this software package, diffraction lines were characterized in terms of peak positions (E_{hkl}), integrated intensities (I_{hkl}) and integral breadths (I_B). Values and results given in the following will be as they were calculated by this package.[4]

2.3.3 KMC-2 Beamline

At the diffractometry experimental station of the KMC-2 beamline at BESSY II additional *in-situ* experiments as well as texture measurements of the *in-situ* grown spinel layers were conducted. The reference paper for the KMC-2 beamline is Erko et al. (2000).

At this beamline, a monochromatic beam was used; thus, angle-dispersive diffraction measurements were carried out. As it was discovered during the previous beamtime at the EDDI beamline that the spinel reaction layers grow predominantly {111} ori-

[4]No uncertainties were provided for the integrated intensities by the software package, but its relative errors were estimated to only 0.75 % (M. Klaus, personal communication).

ented, this peak was monitored during the *in-situ* experiments. During this beamtime, BESSY II was operated in top-up mode, meaning that the ring current was nominally always near 300 mA.

2.3.3.1 Layout of the Beamline

The layout of the KMC-2 beamline is similar to that of the EDDI beamline. Main differences were that a monochromatic beam and an area detector were used. The white synchrotron beam is monochromatized by means of a SiGe double-crystal monochromator. The energy of the beam was chosen to be 8.0480 keV ($\lambda = 0.15406$ nm), resembling CuKα_1 radiation. Two slit systems collimated the primary beam vertically and horizontally to $1 \times 0.5\,\mathrm{mm}^2$, respectively. The DHS was mounted inside the experimental hutch on a HUBER six-circle diffractometer. Samples were aligned by means of a x-y-z stage and a laser. No slit system was used at the diffracted beam side. The sample-to-detector distance was 60 cm. The two-dimensional detector is a gas filled wire detector which has a spatial resolution of 150 μm and an active area of 115 mm in diameter. It is a general area detector diffraction system (GADDS) from Bruker AXS which covered a 2θ range of 10.5°.

2.3.3.2 Procedure of *in-situ* Experiments and Data Evaluation

The procedure of the *in-situ* experiments was similar to the previous beamtime at the EDDI beamline. At first, the miscut of the substrates had to be determined by varying ω whereas 2θ was held constant at the Bragg angles of the substrates ($2\theta_{0006\,cor} = 41.68°$ and $2\theta_{111\,per} = 36.95°$). This miscut had to be considered after the calibration for the ω of the 111 spinel reflection. The TCU could also be remote controlled by an external computer, and the software package spec® was used to control the diffractometer and the detector system as well as to record the data.

By using an area detector and due to the absence of slit systems at the diffracted beam site, the acquisition time per measurement could be lowered to 30 seconds at this beamline. The huge amount of data per experiment was then evaluated automatically using a script that was executed by the curve fitting software Fityk (Wojdyr, 2010). This script substracted at first the background using a quadratic function, the 111 spinel Bragg reflection was then fitted by an area-based Voigt function which provided the position (2θ), height, integrated intensity (I_{111}) and the full width half maximum ($FWHM$) of the peak.

2.3.3.3 Texture Measurements

In addition to *in-situ* experiments, the macrotexture of the spinel layers was determined at the KMC-2 beamline. Therefore, pole figures for selected samples of all experimental setups were measured. Pole figures are two-dimensional representations of the three-dimensional orientation distribution of polycrystalline samples. The orientation

distribution function (ODF) could be calculated from these measurements using the open-source texture toolbox MTEX (Hielscher and Schaeben, 2008; Bachmann et al., 2010) in its version 3.3.2. The determined ODF provides, for instance, texture indizes (TIs) which give a measure for the degree of preferred orientation.

It was found at the EDDI beamline that the out-of-plane orientation of the spinel crystals on both substrates is primarily {111}, i.e. the scattering vector of the {111} lattice planes is parallel to the substrate normal. This may be a first indication that the crystals grew oriented on and into the substrates. However, for a complete description of the texture, the in-plane orientation of these crystals has to be determined as well. For this reason, a sample is tilted and rotated in a texture goniometer to bring lattice planes into the scattering plane whose scattering vector is not parallel to the substrate normal; such a texture goniometer is presented schematically in Figure 2.10a. The tilt of the sample is denoted by the angle ψ ($0° \leq \psi \leq 90°$).[5] For all $\psi \neq 0$, the diffractometer is out of the coplanar configuration and operates in a noncoplanar geometry (Birkholz, 2006). The angle of rotation of the sample measures the azimuth angle and is denoted by the symbol ϕ ($0° \leq \phi \leq 360°$). The angles ψ and ϕ correspond to the usual pole figure coordinates α and β, respectively. Poles of a particular crystallographic plane are usually presented in stereographic projections which preserve the angular relationships between planes in the projection; such a polar grid is presented in Figure 2.10b. Poles are the

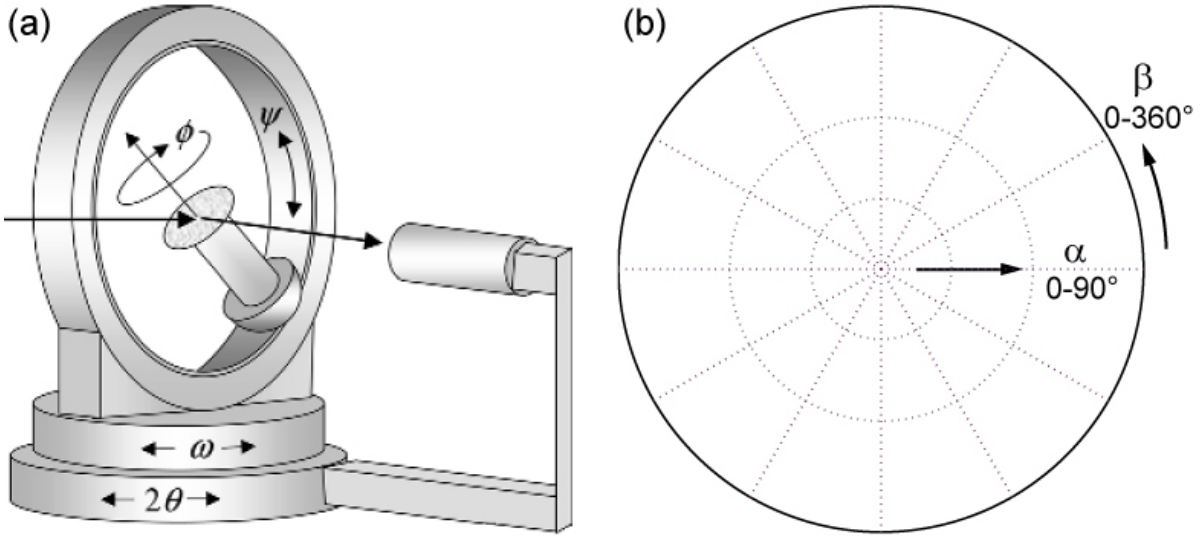

Figure 2.10: (a) Schematic of a four-circle diffractometer with the four variable angles ω, 2θ, ϕ and ψ. The usual θ circle is decoupled from the 2θ circle and is then named ω. The azimuth and tilt angles are denoted by ϕ and ψ, respectively. Image from Birkholz (2006). (b) Polar grid (stereographic projection) in which pole figures are drawn. Pole figure coordinates α and β correspond to ψ and ϕ, respectively.

[5] Also χ is used in the literature where $\chi = 90° - \psi$.

normals of lattice planes that intersect the positive hemisphere of a unit sphere. This hemisphere is projected into two dimensions and a pole figure is obtained. For cubic crystals, the pole is identical to the crystallographic axis with the same indices (Mason and Schuh, 2009).

Three types of textures are usually distinguished in polycrystalline thin films: random textures, fibre textures and epitactic alignment of the crystallites. A film with no preferred orientation of the crystallites would produce a random texture which is characterized by a featureless pole figure, i.e. the distribution of poles in the pole figure is uniform or random. In fibre textures, the orientation of crystallites is fixed with respect to a certain direction of the substrate while the angle of rotation around this direction is not fixed for the crystallites. This direction is designated as the fibre axis, which is often the substrate normal. Fibre textures produce ring patterns of uniform intensities around the centre of the polar plot. Epitaxy is characterized by distinct out-of-plane as well as in-plane orientation relationships between substrates and thin films. The epitactic alignment of crystallites produces sharp spots at specific locations in the pole figure. Depending on the degree of preferred orientation, a sample is then referred to as having a weak, moderate or strong texture (He, 2009).

The ultimate goal in a texture measurement is to derive the ODF which is a 3-D representation of the orientation density of grains in a polycrystal (Engler and Randle, 2010). The ODF is defined as the volume fraction of crystallographic orientations with an orientation in the interval between g and $g + dg$ in a space containing all possible orientations given by (Hielscher et al., 2010; Engler and Randle, 2010):

$$\frac{\Delta V}{V} = \int f(g)\ \mathrm{d}g \tag{2.6}$$

where $\Delta V/V$ is the volume fraction of crystals with orientation g, $f(g)$ is the texture function and dg is the volume of the region of integration in orientation space:

$$\mathrm{d}g = \frac{1}{8\pi^2} \sin\phi\ \mathrm{d}\varphi_1\ \mathrm{d}\phi\ \mathrm{d}\varphi_2 \tag{2.7}$$

where φ_1, ϕ, φ_2 are a triplet of Euler angles which describe the rotation between the crystal and sample coordinates and

$$\oint f(g)\ \mathrm{d}g = 1 \tag{2.8}$$

The ODFs were calculated in MTEX from the measured pole figures using a de La Vallée Poussin kernel with a half-width of 1.25° and a resolution of 5°.

More detailed information on texture measurements using X-ray diffraction techniques can be found in e.g. Engler and Randle (2010) and Birkholz (2006).

2.3.3.4 Procedure of Texture Measurements

A minimum of two pole figures was measured for each sample. For each pole figure, the detector and the sample stage is positioned at the proper Bragg angles 2θ and θ, respectively, of the respective reflection. The first measurement was the {111} pole figure for which 180 or 360° ϕ-scans were carried out at tilt angles of $\psi = 10°$, 30° and 50°, respectively. The area detector covered a tilt range of $\pm 10°$ at each of these three angles so that a ψ-range of about $0-60°$ was considered. To determine whether a distinct in-plane orientation of the crystallites exists, the {311} pole figure was measured afterwards. The angle between two lattice plane normals in the cubic crystal system can be calculated by (e.g. Spieß et al., 2009):

$$cos\,\psi \;=\; \frac{h_1h_2 + k_1k_2 + l_1l_2}{\sqrt{(h_1^2 + k_1^2 + l_1^2)(h_2^2 + k_2^2 + l_2^2)}} \tag{2.9}$$

Thus, the sample has to be tilted 29.5° to bring the {311} lattice planes into Bragg condition when the out-of-plane orientation of most spinel crystals in the reaction band is {111}.

Samples were usually scanned in ϕ-steps of 1° for 5 seconds each measurement. For high-symmetry crystal classes such as the cubic ones, measuring only a part of the full pole figures can solve the texture problem (Birkholz, 2006). It was found during the first texture measurements that the pole figures were centrally symmetric so that indeed 180° ϕ-scans were sufficient for determining the texture.

2.3.4 X-Ray Absorption within the Layers

The fraction of photons absorbed in a thin film depends on the chemical composition of the sample, the density of the material, the path length traveled through the medium, which itself depends on the incident angle and on the thickness of the films, and on the energy of the X-rays. The dominating effect of absorption for energies up to 10 keV is the generation of photoelectrons (Birkholz, 2006). The attenuation of the intensity is given by the Lambert-Beer law:

$$I = I_0 \cdot e^{-\mu_m\,\rho\,s} \tag{2.10}$$

where I is the intensity after absorption, I_0 is the intensity of the incident X-ray beam, μ_m [cm^2/g] is the mass attenuation coefficient, ρ is the density of the material and s is the overall path length traveled by the X-ray beam through the layer (incident plus diffracted beam path). The product $\mu_m \cdot \rho$ gives the linear attenuation coefficient μ_l [cm^{-1}]. The linear attenuation coefficient μ_l for a multi-element substance such as spinel can be obtained through the mass attenuation coefficients of the elements (Creagh and Hubbel, 2004):

$$\mu_l = \rho \sum_i g_i\,(\mu_m)_i \tag{2.11}$$

where g_i is the mass fraction of the element i in the substance. The mass attenuation coefficients of the elements are listed in Creagh and Hubbel (2004) for the CuK$\overline{\alpha}$ radiation energy (8.041 keV) which is close to the energy employed at the KMC-2 beamline (8.048 keV) resembling CuKα_1 radiation. Using this data, the linear attenuation coefficient μ_l was calculated as 110.27 cm^{-1}. The path length s is given by $s/2 = \Delta x/\sin\theta$. Thus, for a maximum spinel layer thickness of 400 nm and an incident angle of 9.5° employed at the KMC-2 beamline, the intensity will be attenuated by 5.2 %. Most spinel layers were in the order of 100 nm; for this thickness the attenuation is only 1.3 %. The attenuation will be even less than these values because the polycrystalline thin films are less dense than bulk spinel.

2.3.5 Estimation of Crystallite Sizes

A rough estimation of the crystallite size D — more specifically the average size of coherent scattering domains — is provided by the Scherrer equation (e.g. Spieß et al., 2009):

$$D = \frac{K \cdot \lambda}{B \cdot cos\,\theta_{hkl}} \tag{2.12}$$

where $K = 0.89$ when using the $FWHM$ and $K = 1$ when using the I_B; B is the determined $FWHM$ or I_B in radians. The Scherrer equation can be applied for crystallite sizes below 150–200 nm (Spieß et al., 2009). The evolution of crystallite sizes presented in chapter 'Results' was calculated using this equation. The decrease of the $FWHM$ or I_B with time results usually from an increase of the crystallite size.

2.4 Transmission Electron Microscopy

TEM was used as a complementary *ex-situ* technique to the rather bulk X-ray diffraction methods described above. It was employed to characterize representative samples before the *in-situ* experiments and to investigate the spinel layers after the *in-situ* experiments in terms of absolute reaction rim widths, microstructures, microtextures and chemical properties. The preparation of cross-sectional foils using the FIB method and their analysis were conducted in cooperation with Dr. R. Wirth from the GFZ German Research Centre for Geosciences in Potsdam, Germany. Focussing on geomaterials, informations about FIB sample preparation in combination with subsequent TEM analysis can be found in Wirth (2004) and Wirth (2009). General informations about TEM can be found in e.g. Fultz and Howe (2008) and Williams and Carter (2009). A summary of the FIB techniques is given in e.g. Gianuzzi et al. (2005).

FIB was used to extract cross-sectional foils from the center of the samples. For milling purposes, a FEI FIB 200 TEM device operated with a Ga^+ ion beam at an acceleration voltage of 30 kV was used. Foil dimensions were $15 \times 5.5 \times 0.15\,\mu m^3$ so that the run

products could be analyzed over a lateral extent of about 15 μm; such a foil is presented in Figure 2.11.

For analyses, a FEI Tecnai G2 F20 X-Twin microscope equipped with a field emission gun as electron source operated at an acceleration voltage of 200 kV was used. Using conventional TEM (CTEM), the run products were imaged mainly by bright-field (BF) TEM, but also dark-field (DF) micrographs were acquired. In the scanning transmission electron microscopy (STEM) mode, high-resolution transmission electron microscopy (HRTEM) was used to study the interfaces between phases. Diffraction patterns (DPs) were collected using the selected area electron diffraction (SAED) technique. It was applied on some samples to study microtextures and orientation relationships. A diffrac-

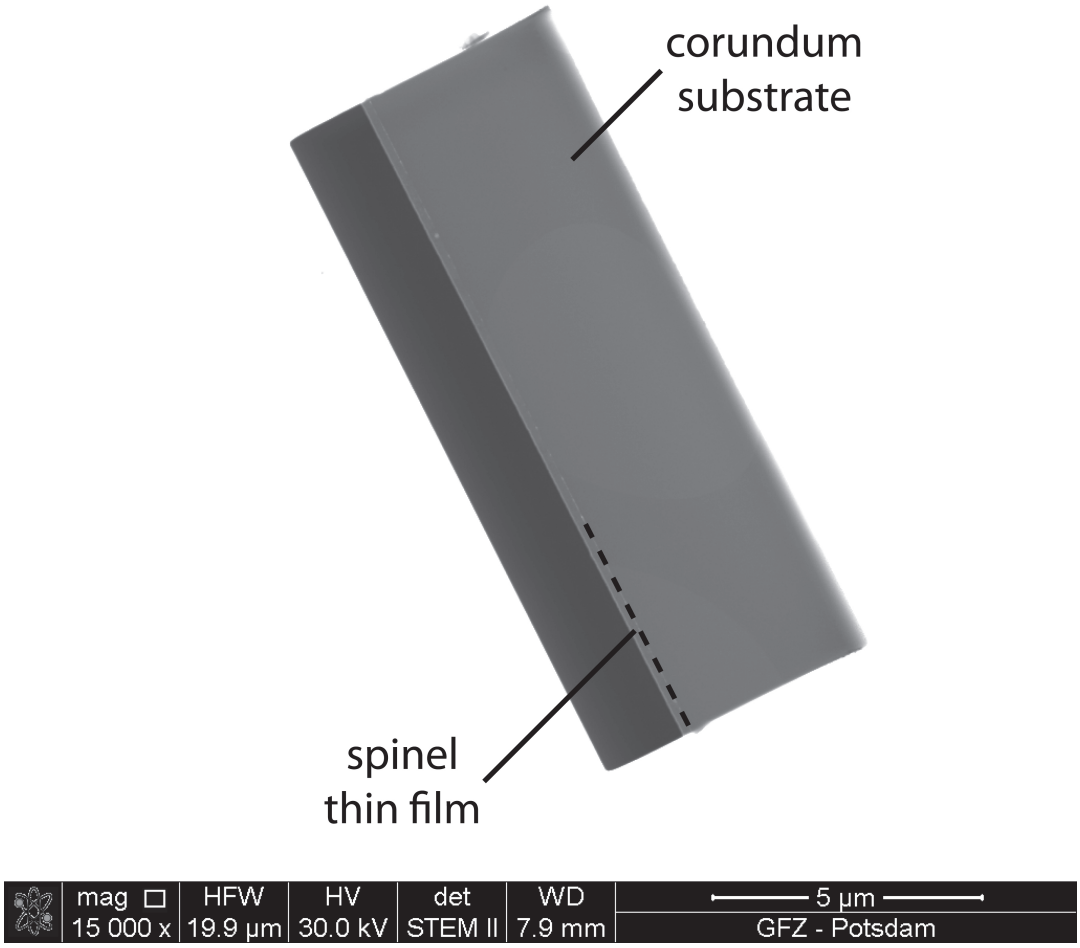

Figure 2.11: Cross-sectional TEM foil milled out of the center of a sample by FIB. The foil is imaged here by a FEI Quanta 3D FEG machine. The spinel thin film on top of the substrate is 180 nm thick. The dashed line marks the phase boundary between substrate and thin film. Note scale bar in the lower right corner.

tion spot in a DP can be indexed using the fundamental relationship $\mathrm{R\,d} = \lambda\,\mathrm{L}$, where R is the distance between the direct and the diffracted beams as measured on the screen, d is the lattice plane distance, λ is the wavelength of the electrons, and L is the camera length (e.g. Williams and Carter, 2009). The product $\lambda\,L$ for the microscope at the GFZ was 27.25 nm · mm, and the diameter of the incident beam was 150 nm (R. Wirth, personal communication).

Using an EDAX X-ray analyzer, phases could be identified by energy-dispersive X-ray spectroscopy (EDX). For elements of similar atomic number it is reasonable to estimate their concentrations by comparing intensities of their $K\alpha$ peaks (Fultz and Howe, 2008). According to the chemical formula of spinel, the peak height of aluminum is therefore about twice that of magnesium in EDX measurements so that spinel could be identified qualitatively. The extent of the spinel layer could also be tracked by EDX mappings and line scans. Originating from the FIB sample preparation, frequently gallium and platinum was found in the EDX spectra whereas copper and carbon signals may emanate from the copper grid and the perforated carbon film at which the foil is placed after lift-out from the sample, respectively (Wirth, 2004; Wirth, 2009). Along with these chemical measurements, high-angle annular dark field (HAADF) images were aquired. The HAADF signal contains and displays Z-contrast plus diffraction contrast information; thinner areas of the foil with the same chemical composition appear to be darker in HAADF micrographs (Wirth, 2009).

Reaction band thicknesses were measured on several TEM micrographs for each sample to calculate a mean Δx along with $1\,\sigma$ uncertainties. Thicknesses were obtained by dividing the area of the spinel reaction band in the particular image by the length of the substrate/spinel interface. Large error margins for Δx indicate that the reaction layer grew highly non-uniform across the foil.

2.5 Other Analytical Methods

2.5.1 Characterization of Sample Surfaces

Sample surfaces, i.e. the grain structures of the thin films in plan view, were analyzed by atomic force microscopy (AFM) and scanning electron microscopy (SEM). The SEM was a FEI Quanta 3D FEG dual beam (FIB/SEM) machine operated at an acceleration voltage of 15 kV in a low vacuum mode.

2.5.2 Grazing Incidence X-Ray Diffraction

GIXRD is especially suited for the analysis of thin films. A schematic of the GIXRD working principle is presented in Figure 2.12. To maximize the signal from the thin film and to minimize contributions of the substrate, low incident angles are used in the GIXRD configuration. Using a small entrance angle α, the path traveled by the X-rays

in the thin film increases significantly in the GIXRD configuration compared to the symmetric θ-θ and θ-2θ configurations, and the structural information contained in the diffractogram may originate only from the thin film and not from the substrate (Birkholz, 2006). The measurement of the diffractogram is performed by keeping the incident angle α of the X-rays constant while only the detector is moved along the diffractometer circle. Thus, the scattering vector $\vec{s}_{hkl}$ of a particular set of lattice planes is not parallel to the surface normal s_3 as it is the case for the symmetric θ-θ and θ-2θ configurations in which the lattice planes causing an observed Bragg reflection are all oriented parallel with the substrate plane (Birkholz, 2006). This method may thus not be very useful for epitaxial aligned thin films.

An X'Pert PRO MPD device with a copper anode was used for the GIXRD measurements. The X-ray tube operated in line focus mode, the generator voltage was 40 kV, and the tube current was 30 mA. The incident beam was shaped by a $1/16^\circ$ fixed divergence slit which controls the equatorial divergence of the beam whereas the axial divergence was controlled by 0.04 rad Soller slits. A beam mask was employed to control the irradiated width on the sample, and a nickel filter with a thickness of 0.02 mm suppressed the CuKβ radiation. On the diffracted beam side, 0.04 rad Soller slits were used as well. Scans were usually performed in the range $2\theta = 16$–70° using a step size of 0.02°.

GIXRD verified that only spinel crystallized after using synthetic $MgAl_2O_4$ pellets for PLD; this is relevant for the three-layer setups where a spinel seed layer was deposited between the reactants (cf. Figs. 2.5c and 2.5d on page 23).

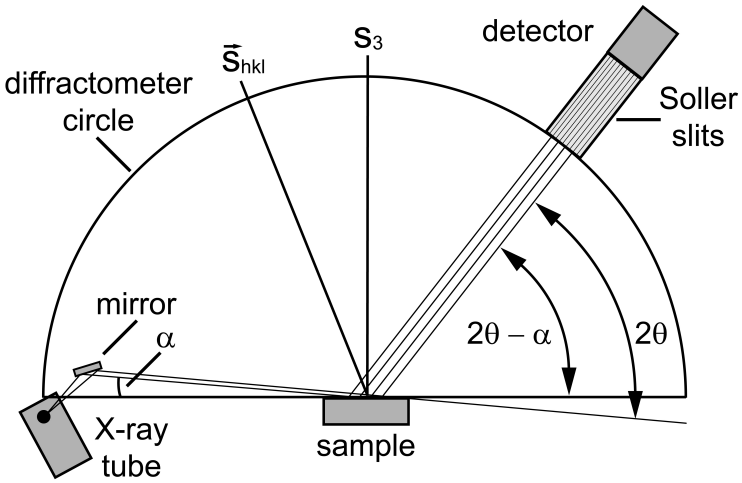

Figure 2.12: Schematic of the GIXRD configuration. The detector is moved along the diffractometer circle while the X-ray tube is fixed. The scattering vector $\vec{s}_{hkl}$ points along the bisection of the incident and diffracted beam. The sample includes thin film and substrate, but only the thin film is probed. Modified after Birkholz (2006).

3 Results

The three different experimental setups and the stages of the experiments are presented briefly in the first section of this chapter. The results of the *in-situ* experiments, texture measurements and *ex-situ* TEM microstructure analyses are presented afterwards. For a clear and comprehensive characterization of a specific experiment, TEM micrographs are also presented in the section of the *in-situ* measurements. The *ex-situ* analyses of spinel seed layers is presented in the last section of this chapter.

3.1 In-situ Experiments — General Remarks

3.1.1 Experimental Setups

Spinel growth in three different experimental setups was investigated; these setups are presented schematically in Figure 3.1. The one-layer setup designates samples in which initially amorphous $MgAl_2O_4$ layers crystallized to spinel. The two-layer setup designates samples in which spinel layers are supposed to grow between substrate and reactant layer. The three-layer setup designates samples in which a spinel layer was deposited between the reactants before to avoid possible nucleation problems. It was additionally observed in similar experiments that reaction layers grow irregular in thickness when no seed layer

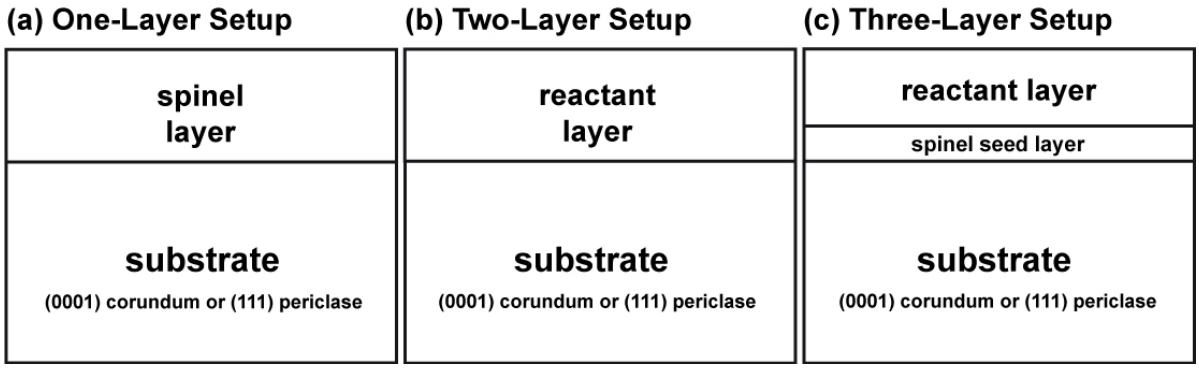

Figure 3.1: Schematics of the experimental setups. (a) One-layer setup: crystallization of spinel thin films on top of the substrates. (b) Two-layer setup: monitoring of spinel growth between the reactants. (c) Three-layer setup: monitoring of the expansion of a spinel seed layer that initially had a thickness of approximately 50 nm.

of the reaction product was deposited before (e.g. Kotula and Carter, 1995; Kotula and Carter, 1996; R. Milke, personal communication).[1]

The two-layer and three-layer experimental setups were also presented by cross-sectional TEM micrographs on the characterization of the starting materials in Figure 2.5 on page 23.

3.1.2 Stages of the Experiments

The procedure during the *in-situ* experiments was explained in sections 2.3.2.2 and 2.3.3.2 for the beamtimes at the EDDI and the KMC-2 beamlines, respectively. The different stages of an experiment are additionally illustrated in Figure 3.2. The experiments can be divided into four stages; these stages are separated by dashed lines in Figure 3.2.

1. In many experiments at the EDDI beamline, a preliminary measurement at room temperature was conducted; individual preliminary measurements lasted from 60 to 300 seconds.

2. During the heating stage, spectra and diffractograms were collected every 60 and 30 seconds at the EDDI and KMC-2 beamlines, respectively. The heating rates were always 200 K/min.

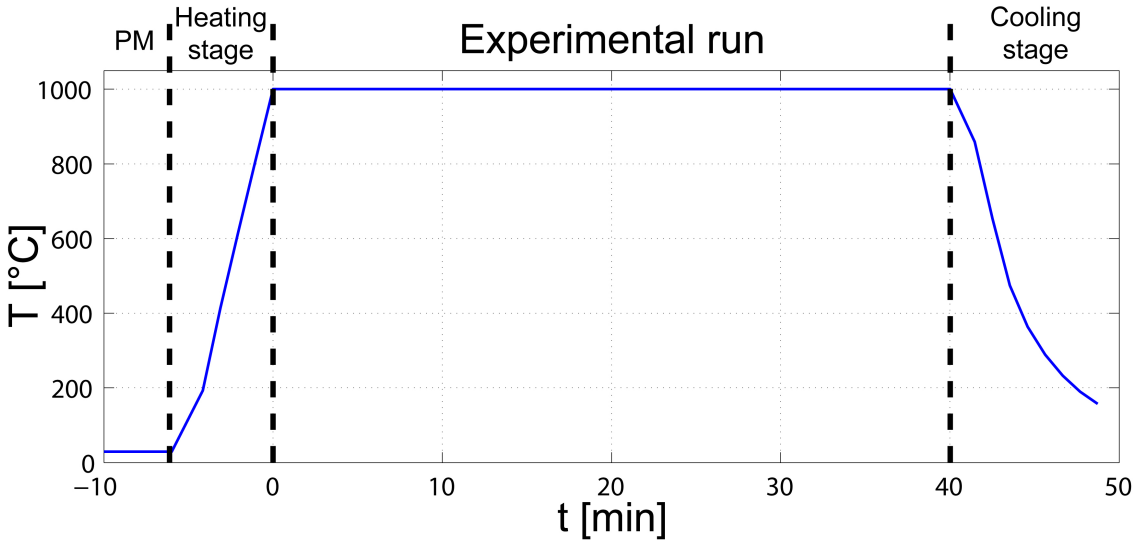

Figure 3.2: Stages of the *in-situ* experiments. PM indicates that a preliminary measurement at room temperature was recorded. Heating and cooling rates during the heating and cooling stages were nominally always 200 K/min; t = 0 when the target temperature at the surface of the sample is reached; $T_{sub} = 1000\,^{\circ}C$ in this example; the experimental run duration is 40 minutes.

[1] Seed layers are also often designated as buffer layers in the literature.

3. At the EDDI beamline, spectra were usually recorded every 300 seconds at target temperature. At the KMC-2 beamline, diffractograms were recorded every 30 seconds. In the following subsections, the start of an experiment will be the moment when target temperature at the sample surface was reached ($T \equiv T_{sub}$ in following graphs), and the experimental run duration will be the time of annealing at target temperature only.

4. Similar to the heating stage, during the cooling stage of the experiments, spectra and diffractograms were collected every 60 and 30 seconds at the EDDI and KMC-2 beamlines, respectively. The cooling rates were also nominally 200 K/min, but it can be seen in Figure 3.2 that the heat dissipated slower, especially at temperatures below 500 °C.

3.2 In-situ Experiments — Corundum Substrates

3.2.1 Spinel Growth in the One-Layer Setup

An initially amorphous spinel layer was deposited onto a corundum substrate, and the emergence of the 111 spinel Bragg reflection upon annealing was monitored *in-situ* at the KMC-2 beamline. To detect the emergence of the peak during the heating stage, the heating rate was exceptionally slow using 50 K/min, and the acquisition time per measurement was 20 seconds. Target temperature was 1000 °C where the sample was annealed for 6 minutes.

Although no TEM foil was prepared for this sample, the thickness of the spinel layer is estimated to be 300 ± 50 nm. This is deduced, on the one hand, from the typical deposition rate for the spinel targets of about 5 nm/min. On the other hand, assuming normal grain growth, average grain diameters of about 300 nm point also to this thickness. The polycrystalline grain structure of the film after the experiment is presented in plan view in Figure 3.3a. Following Thompson (1990), normal grain growth in polycrystalline thin films usually slows and eventually stops once three-dimensional grain growth results in an average grain size that is comparable to the film thickness, i.e. once a completely columnar grain structure develops in which all grain boundaries extend from the top to the bottom of the film; this phenomenon is known as the specimen thickness effect. The driving force for grain growth, which is the reduction of the total grain boundary energy, is reduced for a film with a columnar structure. Additionally, in normal grain growth the grain size distribution follows a log-normal function and is unimodal.

The 111 spinel Bragg reflection started to emerge during the heating stage of the experiment at temperatures above 900 °C, and the intensity increased afterwards, but the overall intensity of the reflection remained relatively low during the 6 minutes of annealing at 1000 °C. Starting with a measurement recorded at 902 °C, every second diffractogram obtained in this interval is plotted in Figure 3.3b; it can be seen that the intensity of the reflection increased and the *FWHM* decreased pointing to the steady

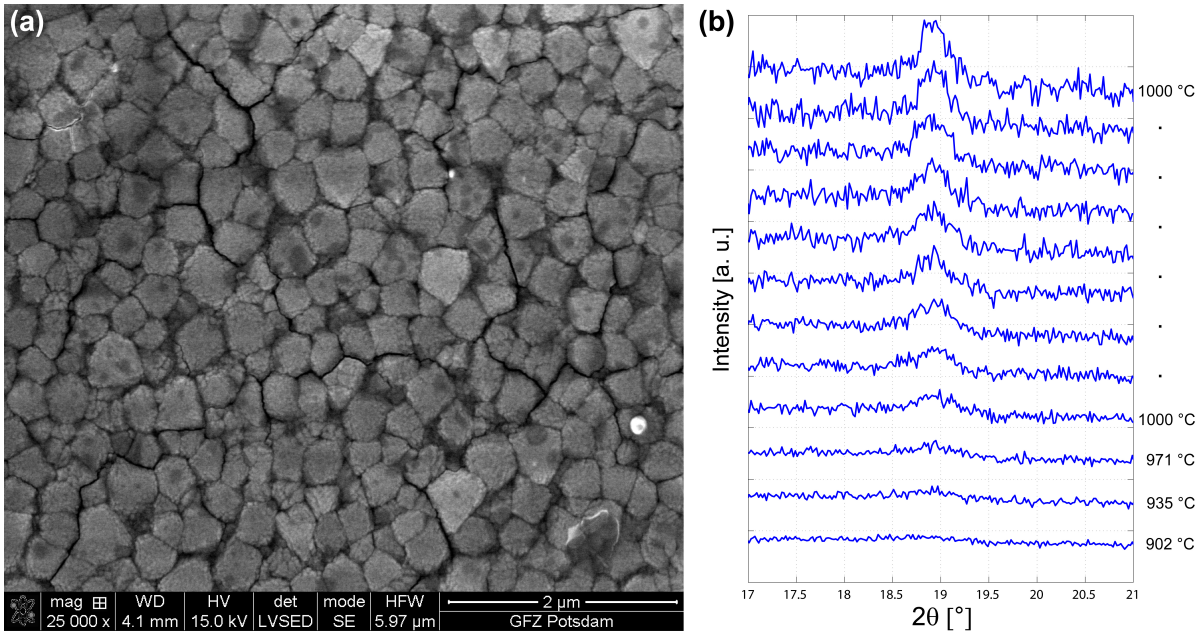

Figure 3.3: Corundum substrates one-layer setup. (a) A representative SEM micrograph shows in plan view the polycrystalline grain structure of the spinel thin film after the experiment. Note scale bar in the lower right corner. (b) The 111 spinel Bragg reflection at about 18.9° started to emerge at temperatures above 900 °C. Diffractograms are shifted along the y-axis. Every second diffractogram in this interval is plotted so that $\Delta t = 40\,s$ between two lines.

growth of {111}-oriented grains. Using the Scherrer equation, a final value of $D = 30\,nm$ was calculated for the crystallite size, differing considerably with the grain diameters of about 300 nm, but the former is more specifically only the average size of coherent scattering domains. The 111 spinel lattice plane distance changed little at 1000 °C; a mean value of $d_{111} = 4.689 \pm 0.003\,Å$ was derived. Texture measurements demonstrated that many crystallites are not {111}-oriented, i.e. they crystallized not epitaxial on the corundum substrate (these measurements are presented among others in section 3.4.1). This and the relatively low but steadily increasing intensity of the 111 reflection illustrates that the grain ensemble probably still recrystallized, suggesting that normal grain growth was not completed after 6 minutes of annealing at 1000 °C. Grains with orientations that lead to low surface energies have an energetic advantage during growth (Thompson, 1990), meaning that the fraction of {111}-oriented crystallites probably would have increased upon further annealing, i.e. these grains replace others during the recrystallization process because surface energies would be greatly reduced for spinel rotation twins forming Σ3 grain boundaries.

Due to a lack of direct contact with the substrate, it is suggested that especially the amorphous material towards the top of the film crystallized initially more randomly than

the material in the vicinity to the substrate which may grew preferably with the expected out-of-plane orientation relationship, namely with (0001) corundum || (111) spinel. Due to the aim of the system to reduce the total grain boundary energy, the {111}-oriented crystallites replace energetic less favored crystallites during the recrystallization process, which eventually leads to an increase of the intensity. This was not investigated further, but the texture measurements presented in section 3.4 demonstrate that the spinel layers grow less randomly oriented when formed topotaxially by reaction. They also show that the exact orientation relationship gets succesively lost the further away from the substrate the spinel crystallites are located.

3.2.2 Crystallization of the MgO Reactant Layer

The initially amorphous MgO reactant layer crystallized to periclase as it was indicated in some experiments at the EDDI beamline by *hhh*-type Bragg reflections of periclase; these reflections can be seen in Figures 3.4, 3.6a and 3.6b. The intensities of the 111 and 222 reflections in Figure 3.4 correspond to a 114 nm thick periclase layer that crystallized upon annealing at 700 °C for 60 minutes; this layer can be seen in a TEM BF micrograph in Figure 3.5a. The 111 reflection started to emerge in the last measurement during the heating stage at 696 °C. At target temperature, the peak position E_{111}, the integrated intensity I_{111} as well as the integral breadth I_B of the reflection remained relatively constant. For the peak position at 24.14 ± 0.03 keV, a lattice plane distance of 2.457 ± 0.003 Å is derived; the I_B is $0.49 \pm 0.05°$.

Periclase reflections were also observed in an experiment at 900 °C which is presented in more detail in the next subsection. The first signals from the MgO reactant layer were observed during the heating stage of the experiment in a spectrum recorded at

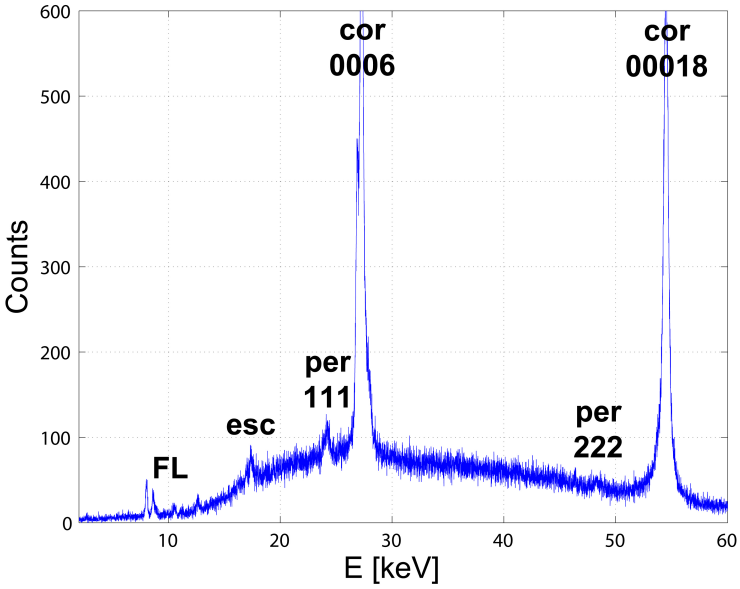

Figure 3.4:
Corundum substrates two-layer setup: EDDI spectrum at 700 °C. After 1 hour of annealing at 700 °C the spectrum exhibits 111 and 222 periclase reflections but no signals from spinel ($\Delta t = 300$ s). This intensity corresponds to the 114 nm thick periclase layer presented in Figure 3.5a.

804 °C (Fig. 3.6a). Similar to the experiment at 700 °C, the 111 and 222 periclase reflections were observed. The 111 periclase reflection was exceptionally prominent in this spectrum in comparison with the substrate peaks. The position of the 111 reflection at 24.104 ± 0.004 keV corresponds to a lattice plane distance of 2.4604 ± 0.0004 Å, and the integral breadth of the peak is 0.62°. At target temperature, the position of the peak was constant at 24.087 ± 0.006 keV, corresponding to a lattice plane distance of 2.4622 ± 0.0006 Å. The integral breadth decreased steadily to a final value of 0.38° after 60 minutes; this indicates that the layer recrystallized considerably during the experiment. Nearly equiaxed periclase crystallites about 50 nm in diameter can be seen in the TEM micrographs in Figures 3.6c and 3.6d.

Probably due to the minuteness and nanocrystallinity of the MgO reactant layers, periclase reflections were not detected in all experiments carried out at the EDDI beamline. For instance, the 114 nm thick layer in Figure 3.5a caused reflections whereas the approximately 40 nm thick layer in Figure 3.5b caused no resolvable reflections. The detection of the thin films depends also on the specific value of ω as it the spectra presented in Figures 3.29c and 3.29d on page 85 demonstrate.

3.2.3 Spinel Growth in the Two-Layer Setup

In this setup, the temperature was varied from 700 to 1000 °C for run durations of 1 hour in each case; additional experiments differing in run duration were conducted at 1000 °C. An overview of samples and respective experimental parameters is given in Table A2 in the Appendix.

In-situ Experiments at 700 and 800 °C: At 700 and 800 °C, no spinel reflections were detected. In accordance with the *in-situ* measurements, neither the subsequent TEM analyses gave an indication of spinel growth at these low temperatures; a very sharp interface between the reactants can be seen in TEM BF micrographs (Fig. 3.5). TEM EDX measurements demonstrated that, although no spinel was formed, aluminum diffused into the periclase layer in the 800 °C experiment.

In-situ Experiments at 900 °C: Spinel as well as periclase reflections were detected in the experiment at 900 °C. At first, it was observable during the heating stage that the MgO reactant layer crystallized to {111}-oriented periclase (Fig. 3.6a). The appearance of the 111 spinel reflection at 12.61 ± 0.01 keV ($d_{111} = 4.703 \pm 0.004$ Å) was observable in the first spectrum obtained at target temperature, i.e. after 5 minutes. A 3-D plot of the spectra obtained at 1000 °C is presented in Figure 3.6b (for a clear arrangement only every second spectrum is plotted). The intensity of this reflection increased steadily with time, indicating that the spinel layer expanded continuously during the experiment. For a comparison with the complementary 1 hour experiment at 1000 °C (sample Cor28), the evolution of I_{111} is presented in Figure 3.8a; it can be seen that the intensity of the

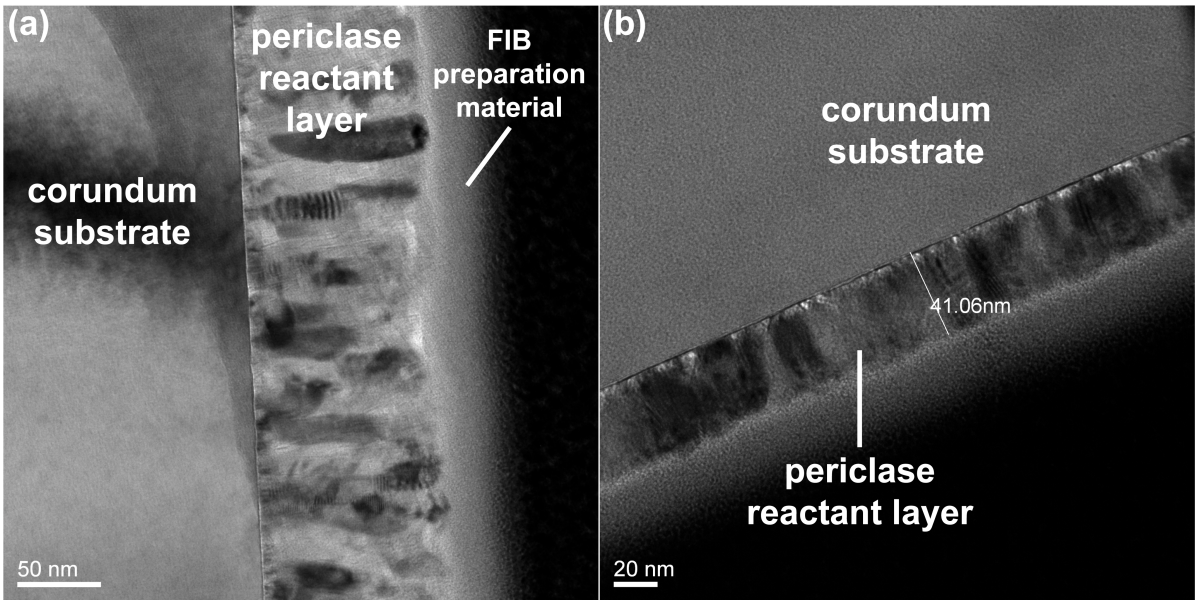

Figure 3.5: Corundum substrates two-layer setup: TEM analyses of the 700 and 800 °C experiments. The micrographs show sharp interfaces between the reactants, indicating that nucleation and growth of spinel at these low temperatures was impeded. (a) 700 °C experiment. The periclase layer has a thickness of 114 nm. Several elongated crystallites can be discerned; their grain boundaries are perpendicular to the interface. Most of these crystallites are {111}-oriented. (b) 800 °C experiment. The layer thickness of 41 nm was measured by the TEM software. Note scale bars in the lower left corners of the images.

111 reflection in the 900 °C experiment rises quickly in the first two measurements, i.e. during the first 10 minutes, but then shows a slower increase in a parabolic manner. This trend can even be recognized in the 3-D plot in Figure 3.6b; the intensity does not increase very much in later stages of the experiment. The position of the reflection varied little; a mean 111 spinel lattice plane distance of 4.706 ± 0.003 Å was derived. The integral breadth decreased from 0.67 to 0.48°.

According to the last spectrum in Figure 3.6b, in which both 111 reflections of the thin films are still present, a spinel layer as well as a periclase layer were found in the subsequent TEM analysis. The extent of the spinel layer was determined in TEM BF images as they are presented in Figures 3.6c and 3.6d. A thickness of 15 ± 1 nm was obtained; this corresponds to only some 32 111 spinel lattice planes. The spinel reaction layer exhibits no conspicuous microstructures; individual crystallites are not discernible. On the other hand, the periclase reaction layer above is polycrystalline; several nearly equiaxed crystallites can be discerned. Their grain boundaries extend from top to bottom and are perpendicular to the plane of the film. Bend contours emerge at the corundum/spinel phase boundary, extending several dozens of nm into the substrate.

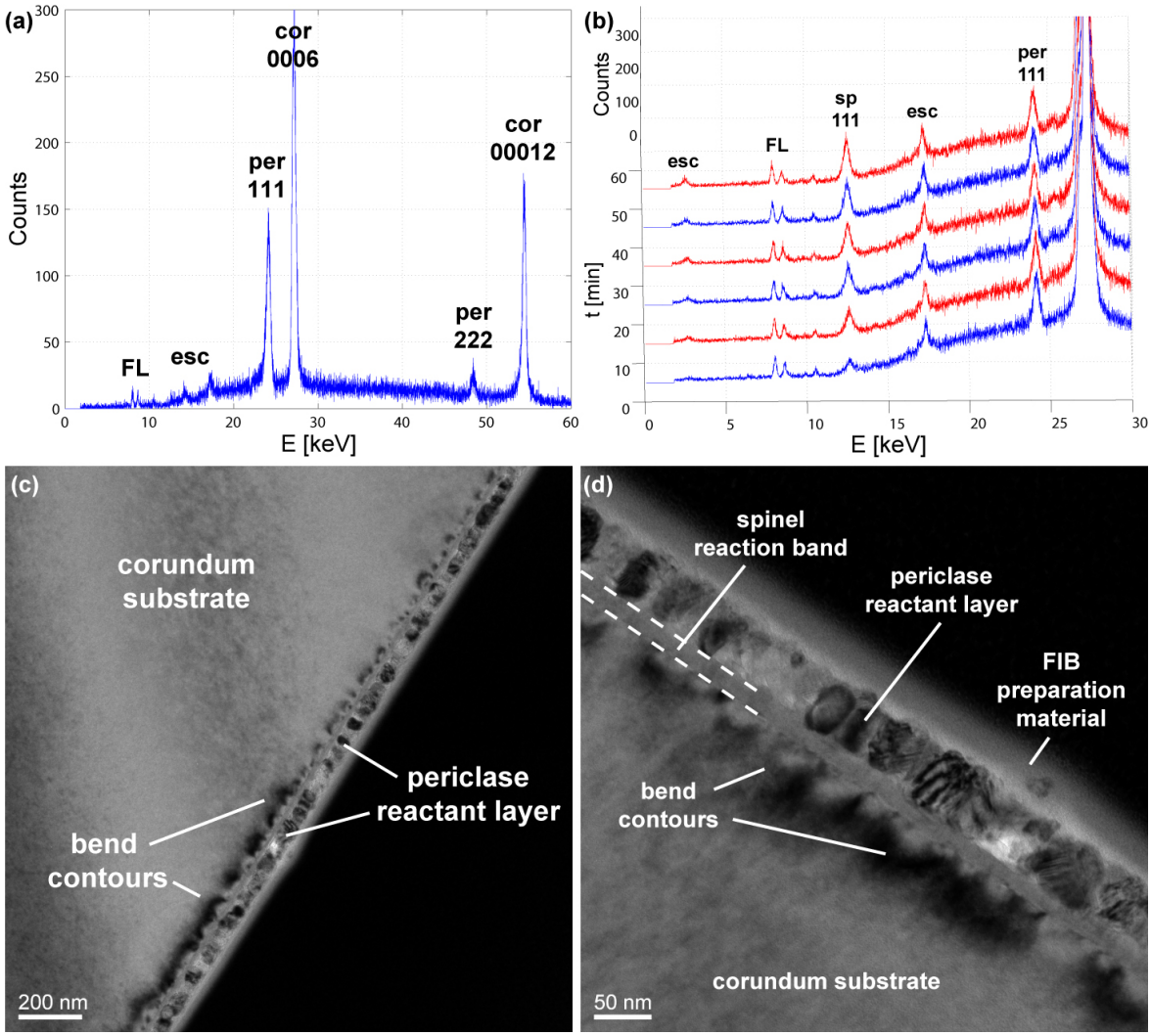

Figure 3.6: Corundum substrates two-layer setup: growth behavior at 900 °C. (a) Spectrum recorded during the heating stage of the experiment (T = 804 °C; Δt = 60 s). The MgO reactant layer crystallized to {111}-oriented periclase; several fluorescence lines and escape peaks appear between 8 and 18 keV. (b) 3-D plot showing the development of the 111 spinel reflection with time. The intensity of the 111 periclase reflection on the right slightly decreases due to the conusmption of the reactant layer. For the sake of clarity, only every second spectrum is plotted. (c) TEM BF micrograph. Overview image shows homogeneity across the foil of the microstructures depicted in (d) in more detail where the extent of the spinel reaction band ($\Delta x = 15 \pm 1$ nm) is marked by dashed lines. The periclase layer above is polycrystalline. Bend contours emerge at the corundum/spinel interface. Note scale bars in the lower left corners of the micrographs.

In-situ Experiments at 1000 °C: The kinetics of spinel growth at 1000 °C were considerably enhanced. In every experiment, I_{111} increased largely linear with time. In three samples (Cor8, Cor9 and Cor30), the MgO reactant layer was completely consumed during the experiment. The consumption could be deduced from the *in-situ* X-ray diffraction data as well as from the *ex-situ* inspection of the samples by TEM. Firstly, the linear increase of I_{111} decelerated to the point at which the intensity remained constant, indicating that the expansion of the layer stopped. Secondly, subsequent TEM analyses (visual inspection as well as EDX measurements) provided no indication of a residual periclase reactant layer in these experiments in contrast to all other samples. This growth behavior is illustrated in Figure 3.7 for sample Cor8 for which the longest linear growth behavior was observed. The evolution of I_{111} with time is presented in Figure 3.7a. The 111 spinel Bragg reflection could accurately be fitted in the 9th measurement obtained at target temperature, i.e. after about 4 minutes; this is in accordance with the experiments $T \geq 900\,°C$ conducted at the EDDI beamline in which the 111 spinel reflection was always observable in the first spectrum, i.e. after 5 minutes, indicating that spinel growth starts immediately with no perceivable retardation. Subsequently, a linear increase is observed for about 100 minutes, then the increase decelarates, and, eventually, I_{111} stays constant after about 130 minutes. The intersection of the linear growth trend with the intensity plateau at the end of the experiment is approximately at 120 minutes.

A TEM BF micrograph of this sample is presented in Figure 3.7b. Two layers can be discerned in this image. The thin, outer layer has a remarkable uniform thickness whereas the thicker, inner layer grew non-uniform into the substrate, exhibiting a wavy interface morphology. TEM EDX analyses revealed that both layers are spinel, implying that a residual MgO reactant layer is missing. A HAADF micrograph and four exemplary EDX measurements are presented in Figure 3.7c. The first two measurements in areas 1 and 2 were conducted in the outer sublayer, and they exhibit the same pattern as measurements 3 and 4 that were conducted in the inner sublayer. The Mg:Al peak height ratio of approximately 1:2 is typical for spinel. Note that the planar microstucture is discernible in the HAADF micrograph of Figure 3.7c as well; EDX measurements were deliberately positioned in both sublayers. Because this planar microstructure points to the cation counterdiffusion mechanism of the spinel-forming reaction, it is presented in more detail in section 3.5.1.

The linear increase of I_{111} at 1000 °C in the experiments at the EDDI beamline was similar to that presented for sample Cor8 in Figure 3.7a except that spectra were recorded only every 5 minutes. In Figure 3.8a are the complementary 1 hour experiments at 900 and 1000 °C compared to depict the parabolic and linear trends, respectively. In Figure 3.8b is a TEM BF image of sample Cor28 shown. The spinel reaction band attained a thickness of $122 \pm 8\,nm$. The reaction band is polycrystalline; individual grains are elongated, grain boundaries extend from top to bottom and are perpendicular to the plane of the film. In contrast to the spinel layer, no periclase grains are visible in this image. The residual reactant layer appears to be highly nanocrystalline, and the periclase/spinel interface is not clearly discernible. For this reason, Al and Mg TEM

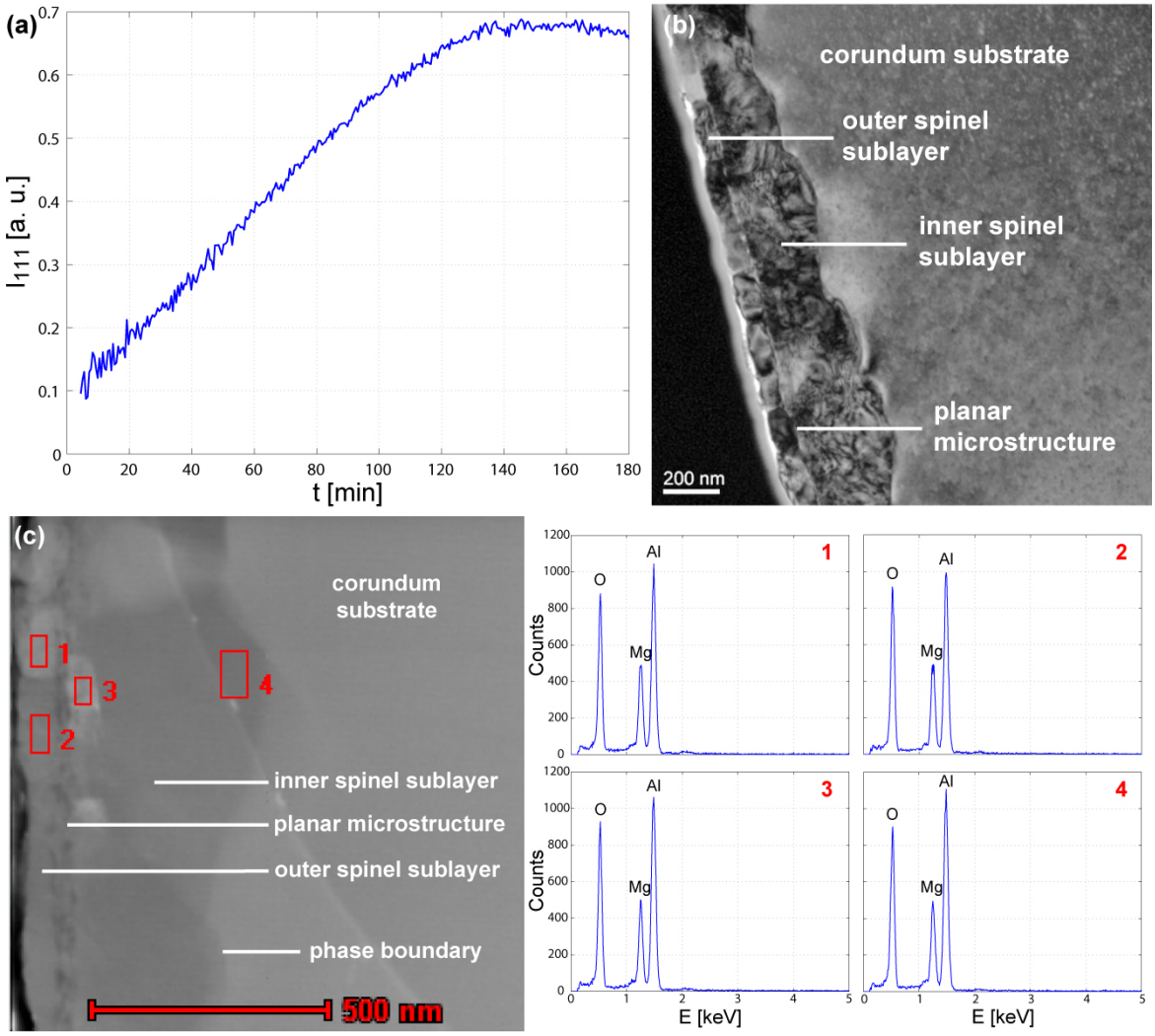

Figure 3.7: Corundum substrates two-layer setup: growth behavior at 1000 °C. (a) Increase of I_{111} with time. A deviation of linearity sets in after about 100 minutes; after about 130 minutes, I_{111} stays constant. (b) The TEM BF micrograph shows a 394 ± 29 nm thick spinel reaction band; a residual reactant layer is absent. The planar microstructure separates the reaction band into two sublayers. The inner sublayer exhibits a wavy interface morphology towards the substrate. (c) HAADF micrograph and TEM EDX measurements; areas of EDX measurements 1, 2, 3 and 4 are marked with red boxes. All four measurements point to the exclusive existence of spinel in these areas. The planar microstructure and the wavy phase boundary are discernible in this micrograph as well. Note scale bars at the bottom of the micrographs.

EDX mappings served to distinguish between spinel and periclase thin films (inset in the lower right of Fig. 3.8b).

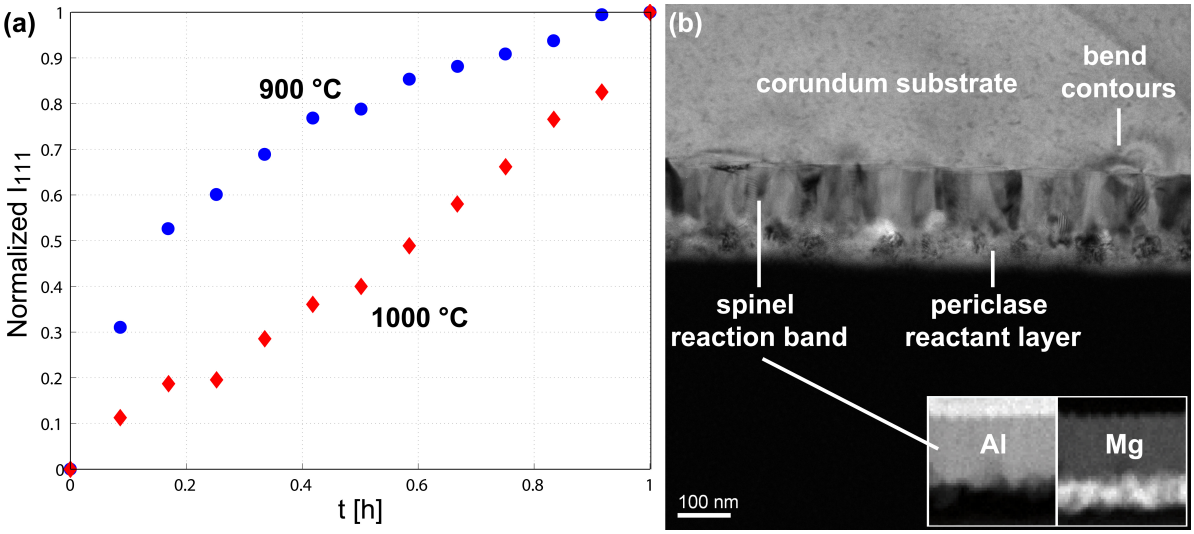

Figure 3.8: (a) Increase of I_{111} with time in the complementary 1 hour experiments at 900 °C (sample Cor26; blue circles) and 1000 °C (sample Cor28; red diamonds) in which the reaction bands attained thicknesses of 15 ± 1 and 122 ± 8 nm, respectively. The I_{111} is normalized to depict the different trends; I_{111} increased parabolically with time at 900 °C but linearly at 1000 °C. (b) TEM BF micrograph of sample Cor28. Inset in the lower right presents TEM EDX mappings that reveal clearly the extent of spinel. Note scale bar in the lower left corner.

Reaction rates at 1000 °C: Reaction rates at 1000 °C seem to differ to some degree. Assuming an interface-controlled reaction regime, reaction band thicknesses and resulting linear reaction rate constants of all 1000 °C experiments are presented in Table 3.1. For all samples in which the periclase reactant layer was consumed during the experiment, the moment of consumption was estimated using the intersection of the linear

Table 3.1: Overview of reaction band thicknesses Δx and resulting linear reaction rates k for the corundum substrates two-layer setup experiments carried out at T = 1000 °C.

Sample	Beamline	Δx [nm]	t [min]	k [nm/s]
Cor8	KMC-2	394 ± 29	≈120	0.055 ± 0.004
Cor9	KMC-2	277 ± 25	≈64	0.072 ± 0.007
Cor27	EDDI	18 ± 1	5	0.060 ± 0.003
Cor28	EDDI	122 ± 8	61.7	0.033 ± 0.003
Cor29	EDDI	71 ± 4	30.8	0.038 ± 0.003
Cor30	EDDI	104 ± 4	≈42.3	0.041 ± 0.002

growth trend with the plateau of constant intensity (cf. Fig. 3.7a); these are the t-values given in Table 3.1 for these three experiments. Additionally, this moment is consistent with sudden changes of the peak position as well as of the peak shape. This behavior is presented in more detail at the end of this subsection on the evolution of lattice plane distances and peak widths. It can be seen in Table 3.1 that k ranges from 0.033 ± 0.003 to 0.072 ± 0.006 nm/min. Comparing samples Cor9 and Cor28, which both were annealed for approximately 1 hour, it can be seen that the reaction rate in sample Cor9 was about twice as fast than in sample Cor28. However, the mean of the six values given in Table 3.1 is $k = 0.05 \pm 0.02$ nm/s.

Onset of Spinel Growth: It was stated before that the 111 spinel Bragg reflection was always observable in the first EDDI spectrum, i.e. after 5 minutes, for all experiments $T \geq 900\,^{\circ}C$. Additionally, in one of the 1000 °C experiments (sample Cor30), the emergence of the 111 spinel reflection was observed during the heating stage. Three measurements of this experiment are presented in Figure 3.9 in a 3-D plot; these were the 4th, 5th and 6th spectra recorded (188, 250 and 313 seconds after the beginning

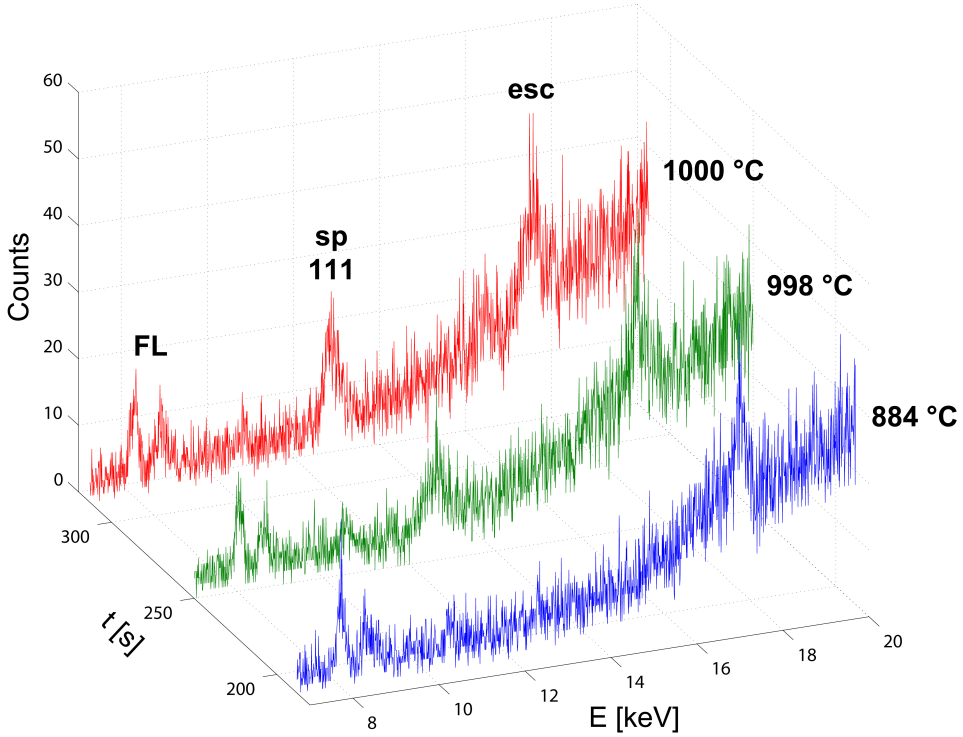

Figure 3.9: Emergence of the 111 spinel reflection at 12.6 keV during the heating stage of an *in-situ* experiment ($\Delta t = 60$ s in all three measurements). Spinel was at first detected at 998 °C. Fluorescence lines stem from copper (8.0 keV) and zinc (8.6 keV) and the escape peak from the 0006 reflection of the corundum substrate at 27.2 keV.

of heating, respectively; $\Delta t = 60\,s$ in each case). The 111 spinel reflection is observable for the first time in the spectrum recorded at 998 °C. This implies that growth of the first few lattice planes occurred in the 60 seconds of annealing between 884 and 998 °C. In comparison with the spectrum recorded at 884 °C, it can be seen that this signal is neither fluorescence nor an escape peak. As it was the case in most other experiments, prominent fluorescence lines appeared in these spectra from copper and zinc at 8.0 and 8.6 keV, respectively, and the intensity of these fluorescence lines is approximately constant in the three spectra.

As stated before, samples Cor8 and Cor9, monitored at the KMC-2 beamline, exhibited no perceivable retardation of spinel growth as well. The peak emerged slowly and was evaluable after 4 minutes at target temperature.

These findings may further constrain the temperatures and time intervals in which growth is detectable using these materials and methods.

Evolution of Lattice Plane Distances and Peak Widths: Besides characterization of the spinel Bragg reflections regarding their intensity, the peaks can of course be evaluated with respect to their position and shape; this provides information on the evolution of lattice plane distances as well as of crystallite sizes during the *in-situ* experiments. The 111 spinel lattice plane distances, $FHWMs/I_Bs$ and calculated crystallite sizes at the end of all relevant experiments in this setup are summarized in Table 3.2.

Table 3.2: Corundum two-layer setup: overview of lattice plane distances, *FWHMs* (KMC-2) or I_Bs (EDDI) and crystallite sizes determined from the 111 spinel Bragg reflection, respectively. To account for the sudden changes of these values in the experiments in which the periclase reactant layer was consumed, two entries are given denoted by *a* (for the values at the point of consumption) and *b* (for the last measurement at target temperature) in the sample names (compare also with Figure 3.10).

Sample	d_{111} [Å]	FWHM [°]	D [nm]
Cor8a (1000 °C; 120 min)	4.720 ± 0.001	0.20	39
Cor8b (1000 °C; 180.2 min)	4.717 ± 0.001	0.18	44
Cor9a (1000 °C; 64 min)	4.721 ± 0.001	0.22	36
Cor9b (1000 °C; 120.1 min)	4.715 ± 0.001	0.19	41
Sample	d_{111} [Å]	I_B [°]	D [nm]
Cor26 (900 °C; 60.6 min)	4.708 ± 0.002	0.48	12
Cor28 (1000 °C; 61.7 min)	4.720 ± 0.001	0.28	20
Cor29 (1000 °C; 30.8 min)	4.722 ± 0.002	0.35	17
Cor30a (1000 °C; 42.3 min)	4.719 ± 0.001	0.32	18
Cor30b (1000 °C; 119.3 min)	4.715 ± 0.001	0.32	18

Samples Cor8 and Cor9 serve well to depict the evolution of the 111 spinel lattice plane distances and peak shapes with respect to the *FWHM* during the course of the *in-situ* experiments. Figures 3.10a and 3.10b present the decreasing trends of the 111 spinel lattice plane distances in these experiments. Due to the initial minuteness of the reaction layer, the values at the beginning exhibit a marked scatter; however, this variation is reduced greatly after about 20 minutes. Starting at about 4.735 Å, d_{111} decreases steadily with time approaching 4.720 Å. This value of 4.720 Å is consistent with the experiments at 1000 °C monitored at the EDDI beamline. At this point, the periclase reactant layer was inferred to be consumed in both experiments (after approximately 120 and 64 minutes, respectively), and the decreasing trend is suddenly enhanced afterwards; a kink is visible in the graphs (especially for sample Cor9 in Figure 3.10b). Thus, this kink is another indicator at which point the reactant layer was consumed during the runs. After the consumption, d_{111} falls consistently by 0.004 ± 0.001 Å at the end of the three experiments in which consumption was observed.

The *FWHM* of the 111 spinel reflections decrease also (Figs. 3.10c and 3.10d). Starting at 0.7°, the width drops gradually to approximately 0.2° at the end of both runs; the trend is remarkably similar between the experiments. The position of the reflection and the *FWHM* are both processed in the Scherrer equation to estimate crystallite sizes; the evolution of the crystallite size determined this way is presented in Figures 3.10e and 3.10f. Starting at about 10 nm, the crystallite size increases parabolically to more than 40 nm at the end of both experiments. A sudden enhanced increase of the crystallite size can be seen for sample Cor8 in Figure 3.10e after 120 minutes, the assumed moment of consumption of the periclase reactant layer; this may indicate that the spinel grains recrystallized after the consumption.

Samples Cor28 and Cor29 were scanned again after the *in-situ* experiment at room temperature. The 111 spinel lattice plane distances were determined as 4.675 ± 0.001 and 4.680 ± 0.001 Å, respectively; the I_B was 0.28 and 0.34°, respectively, in very good agreement with the values obtained at target temperature.

3.2.4 Spinel Growth in the Three-Layer Setup

In this setup, the temperature was varied from 800 to 1000 °C; experiments were conducted at 800, 900 and 1000 °C for run durations of approximately 40 minutes in each case. Additional experiments differing in run duration were carried out at 1000 °C. An overview of samples and respective experimental parameters is given in Table A2 in the Appendix. Two TEM foils were prepared from this setup.

In-situ Experiment at 800 °C: Similar to the complementary experiment without a seed layer, growth was probably impeded at 800 °C. The intensity of the spinel seed layer increased slightly whereas the integral breadth decreased from 0.61° in a measurement at room temperature to 0.50° at the end of the experiment. Using the Scherrer equation, crystallite size was calculated to increase from 9 to 11 nm during the course of the run.

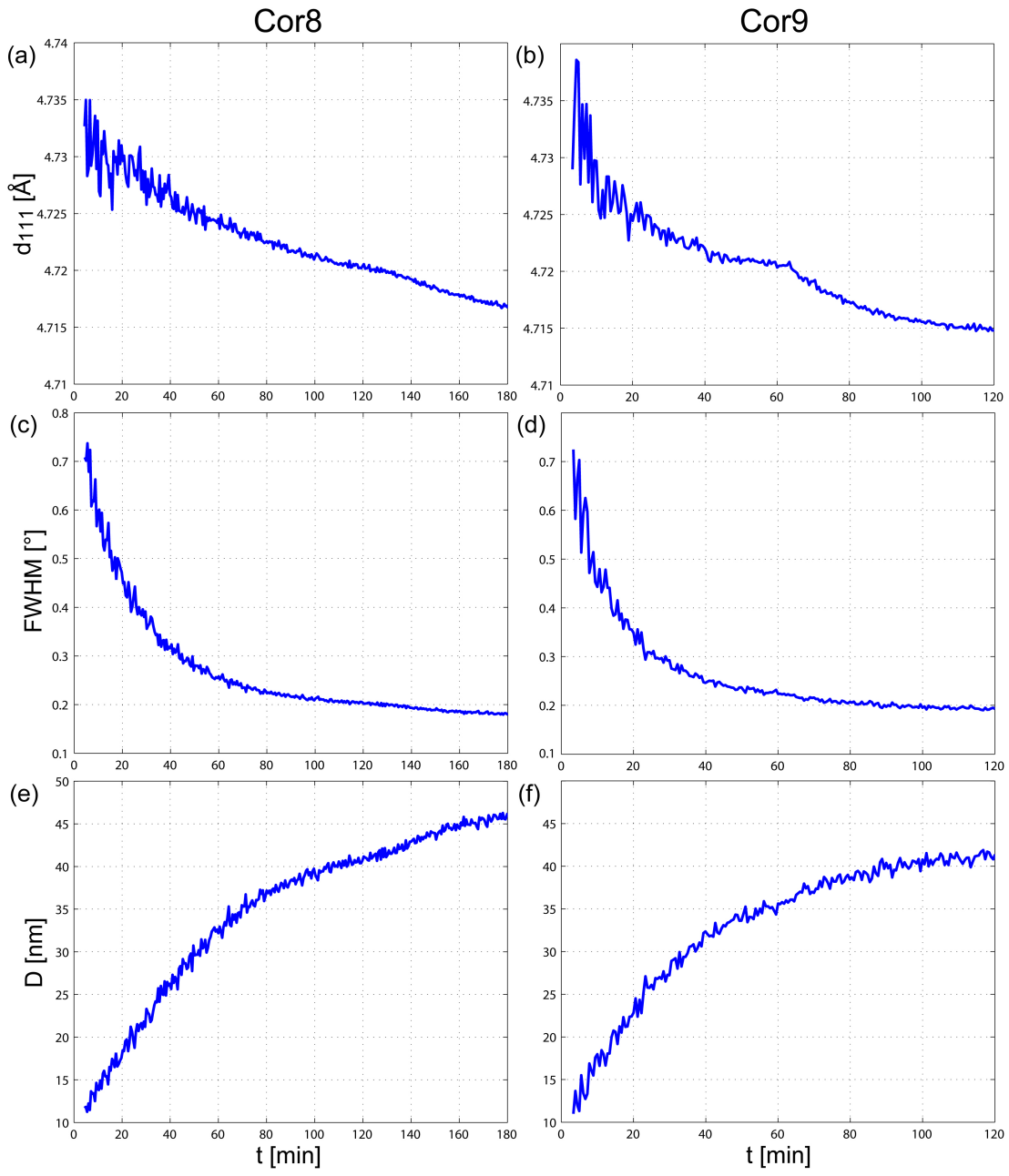

Figure 3.10: Corundum substrates two-layer setup: evolution of (a, b) 111 spinel lattice plane distances, (c, d) *FWHMs* and (e, f) crystallite sizes during the course of experiments Cor8 (left column) and Cor9 (right column). Note that the periclase reactant layer was estimated to be consumed after 120 and 64 minutes, respectively; a sudden change at these moments — especially for the d-value — is observable confirming these estimates.

The position of the 111 spinel Bragg reflection varied little at target temperature; a mean d-value of 4.691 ± 0.002 Å was derived. Periclase reflections were not detected in accordance with many experiments in the two-layer setup.

To conclude, a slight increase of I_{111} along with a decrease of the I_B with time may point to additional growth, but both observations may be related to recrystallization processes within the spinel seed layer. No TEM foil was prepared for this sample so that an *ex-situ* assessment is missing which could verify an expansion of the seed layer.

In-situ Experiment at 900 °C: The run at 900 °C yielded similar results to the complementary experiment in the two-layer setup. The spinel seed layer was not detected in a preliminary measurement at room temperature and not in the first three measurements during the heating stage as also the corundum substrate reflections disappeared in these spectra; however, the 111 spinel as well as the substrate Bragg reflections were detected afterwards. The first signal of spinel could be observed in a spectrum recorded at 813 °C. Starting with this measurement, the increase of I_{111} with time is presented in Figure 3.11a. The increase exhibits parabolic behavior similar to the complementary experiment without a seed layer (cf. Fig. 3.8). The steadily increasing trend points to a steady expansion of the spinel seed layer during the experiment; however, growth was probably retarded greatly because only 15 ± 1 nm of spinel were formed during 1 hour in the complementary experiment in the two-layer setup. Also the I_B of the 111 spinel reflection and the calculated crystallite size remained more or less constant at 0.48° and 12 nm, respectively, indicating negligible additional growth. The extent of the spinel layer is 52 ± 2 nm as it was determined by surveying several TEM micrographs. A TEM BF micrograph of this sample is presented in Figure 3.11b. It was always tried to deposit 50 nm of spinel in the three-layer setups (cf. section 2.2.1 on the deposition of the films), but the real thickness of each seed layer will vary by several nanometers. More reliable evidence for additional growth give again bend contours at the corundum/spinel phase boundary. As it will be presented in more detail in section 3.5.1 on microstructures visible in TEM micrographs, these contrasts emerge once spinel growth starts. Compared with other samples, they are not that pronounced in this micrograph but rather blurry and fuzzy (again similar to the complementary experiment, cf. Fig. 3.6d); this points to only a slight expansion of the seed layer.

It can be seen in Figure 3.11b that the amorphous MgO reactant layer crystallized to a polycrystalline thin film. The periclase grains are nearly equiaxed, their grain boundaries extend from top to bottom and are perpendicular to the plane of the film. Grain boundaries or other microstructures — such as the extent of the original seed layer inside the band — are not that well discernible in the spinel layer using the BF mode; however, rounded grains are visible using the DF mode, and these crystallites have dimensions consistent with the value calculated from the *in-situ* experiment ($D = 12$ nm). Thus, unlike the grains in the periclase layer, crystallites may not be elongated in the spinel layer but rather rounded and much smaller.

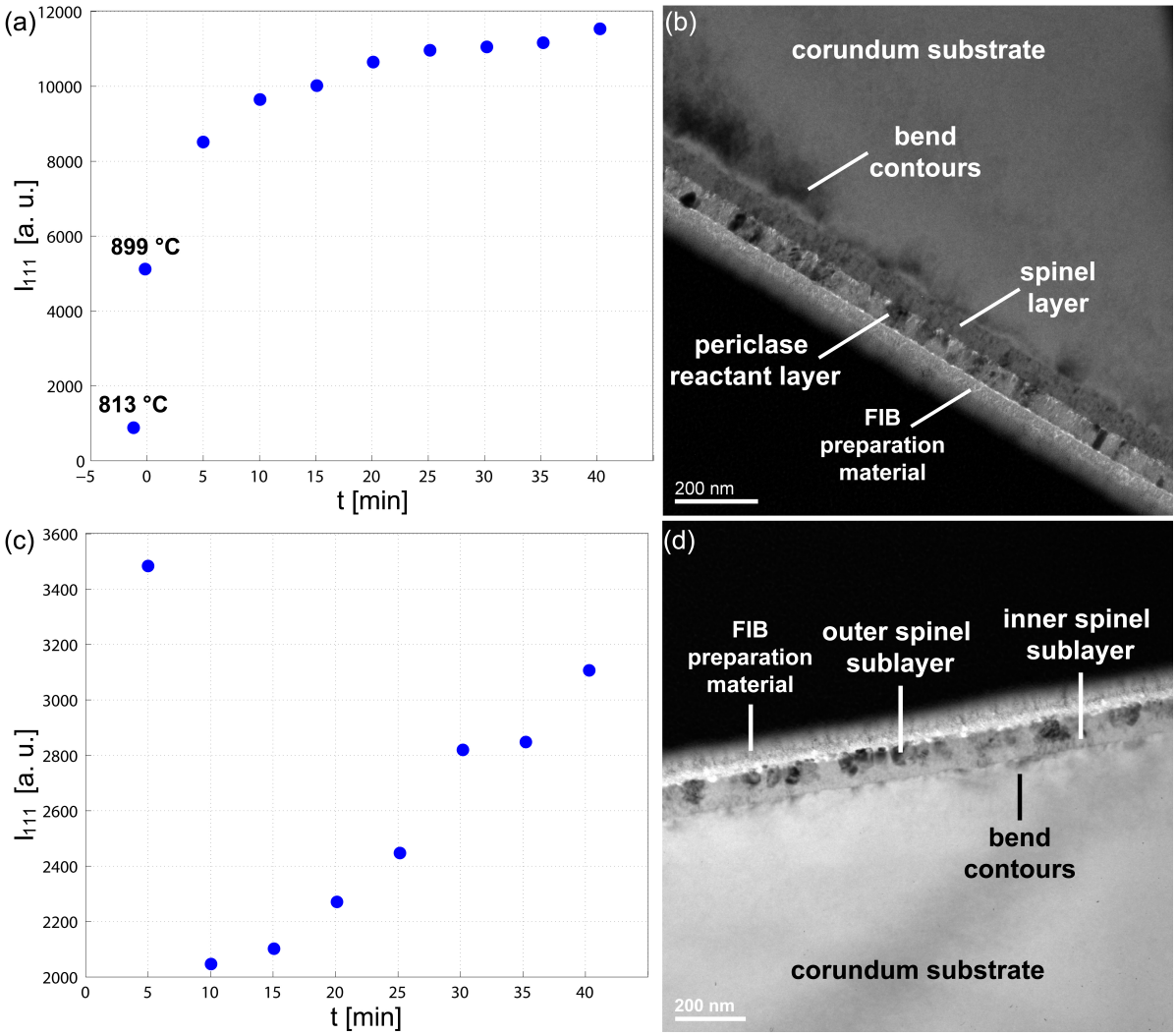

Figure 3.11: Corundum substrates three-layer setup: growth behavior at 900 and 1000 °C. (a) Evolution of I_{111} with time at 900 °C starting with a measurement recorded at 813 °C; a parabolic trend is indicated. (b) A TEM BF micrograph of this sample shows a polycrystalline periclase layer, a 52 ± 2 nm thick spinel layer and several blurred bend contours. (c) Evolution of I_{111} with time at 1000 °C; a linear trend is indicated. (d) TEM BF micrograph. No relics of the reactant layer were found; both sublayers are spinel. Note scale bars in the lower left corners of the micrographs.

To conclude, the parabolic increase of I_{111} and the bend contours point to an expansion of the spinel seed layer at 900 °C. The complementary experiment at 900 °C in the two-layer setup demonstrated that the reaction rate is very slow at this temperature; it is thus inferred that the additional growth is restricted to approximately 10 nm in this experiment.

In-situ Experiments at 1000 °C: In each of the experiments at 1000 °C, the I_{111} increased steadily with time and linear trends are indicated. Even in the longest experiment in this setup, the I_{111} still rose after 2 hours (but the I_B remained virtually constant at 0.36° during the second hour). A consumption of the MgO reactant layer could never be deduced from the *in-situ* measurements unlike it was suggested for three samples in the two-layer setup in which the increase of I_{111} decelerated and the intensity remained constant after some time (Fig. 3.7a) and the moment of consumption was accompanied with a sudden pronounced drop of the lattice plane distance (Figs. 3.10a and 3.10b).

Despite a constantly rising I_{111}, a residual periclase layer was not found in the subsequent TEM analysis of sample Cor21 — the only 1000 °C experiment of which a TEM foil was taken. The evolution of I_{111} with time of this experiment is presented in Figure 3.11c. The first spectrum recorded after 5 minutes exhibits an anomalous high intensity; however, afterwards I_{111} dropped and it then increased steadily in a linear fashion. A TEM micrograph of this sample is presented in Figure 3.11d. It can be seen that the reaction band grew uniform into the substrate; a thickness of 80 ± 1 nm was determined. Spinel seed layer expansion is indicated by bend contours. They are commonly more pronounced in other micrographs obtained from this foil than in subimage 3.11d. However, in this micrograph it can be seen best that the reaction band is composed of at least two sublayers. Both sublayers are spinel as it was revealed by TEM EDX. The outer sublayer exhibits individual, equiaxed crystallites which appear occasionally much darker than the material of the inner spinel sublayer below. This latter sublayer is unstructured in this micrograph, but in a DF image many tiny crystallites appeared; their dimensions match with the value derived from the Scherrer equation ($D = 14$ nm).

A third spinel sublayer cannot be discerned in TEM micrographs. Besides the spinel seed layer inside the reaction band, a corundum-grown as well as a periclase-grown spinel sublayer is expected with respect to the cation counterdiffusion mechanism of the spinel-forming reaction. It is suggested that the inner spinel sublayer in Figure 3.11d is the corundum-grown sublayer and the outer spinel sublayer is the seed layer. The periclase-grown sublayer may be too small to distinguish it from the seed layer.

Evolution of Lattice Plane Distances and Peak Widths: An overview of 111 spinel lattice plane distances, $FWHM/I_Bs$ and crystallite sizes at the end of the experiments in this setup is presented in Table 3.3. The three experiments monitored at 1000 °C have a mean d-value of 4.710 ± 0.002 Å. In contrast, the samples without a seed layer have consistent d-values of 4.720 ± 0.002 Å. It has to be noted that for sample Cor18, monitored at 900 °C, a slightly higher d-value was determined than for the aforementioned samples monitored at 1000 °C. As expected, the smallest d-value was derived at 800 °C.

In this setup, the 111 spinel lattice plane distances remained more or less constant at target temperatures. A decreasing or increasing trend is not indicated as the evolution of d_{111} in Figure 3.12 demonstrates.

The *FHWM* of the 111 spinel reflection of sample Cor21 decreased from 0.52° at room temperature to 0.40° in the last measurement at target temperature. Using the Scherrer equation, the crystallite size was estimated to increase from 11 to 14 nm. Similar values for the $FWHM/I_B$ and crystallite sizes were obtained for the other samples (Table 3.3). As expected, trends indicate that for similar run durations (samples Cor16, Cor18 and Cor21 monitored for 40 minutes) the I_B is smaller at higher temperatures. Likewise, the $FWHM/I_B$ decreases for longer run durations at the same temperature (comparing samples Cor17, Cor21 and Cor22 monitored at 1000 °C).

Table 3.3: Corundum three-layer setup: overview of lattice plane distances, the *FWHM* (KMC-2) or $I_B s$ (EDDI) and crystallite sizes determined from the 111 spinel Bragg reflection, respectively.

Sample	d_{111} [Å]	FWHM [°]	D [nm]
Cor17 (1000 °C; 10.9 min)	4.710 ± 0.002	0.55	14
Sample	d_{111} [Å]	I_B [°]	D [nm]
Cor16 (800 °C; 40.3 min)	4.694 ± 0.002	0.50	11
Cor18 (900 °C; 40.3 min)	4.716 ± 0.001	0.48	12
Cor21 (1000 °C; 40.3 min)	4.712 ± 0.002	0.40	14
Cor22 (1000 °C; 120.3 min)	4.708 ± 0.001	0.36	16

Linear Thermal Expansion: The 111 spinel reflection in experiment Cor21 was detected in all spectra recorded (including a preliminary measurement). As determined using the EDDI software package, the evolution of the 111 spinel lattice plane distance during the entire experiment is presented in Figure 3.12. The data can be used to calculate mean linear thermal expansion as well as contraction coefficients α in the form $\alpha = \Delta \mathrm{l} \cdot \mathrm{l_0}^{-1} \cdot \Delta \mathrm{T}^{-1}$, where Δl is the change in the lattice plane distance compared to the initial lattice plane distance l_0 at room temperature, and ΔT is the change in temperature (e.g. Salmang and Scholze, 2007). The increase from 4.632 Å at 29 °C to 4.708 Å at 1000 °C results in a linear thermal expansion coefficient of $\alpha_{29/1000} = 16.9 \cdot 10^{-6}\,\mathrm{K}^{-1}$. As can be seen in Figure 3.12, at target temperature the distance increased slightly. The decrease from 4.712 Å in the last measurement at target temperature to 4.677 Å in the last spectrum recorded during the cooling stage at 157 °C results in a linear contraction coefficient of $\alpha_{1000/157} = 8.8 \cdot 10^{-6}\,\mathrm{K}^{-1}$. The value of 4.677 ± 0.002 Å determined at 157 °C matches well with values of samples in the two-layer setup in which at room temperature 4.675 ± 0.001 and 4.680 ± 0.001 Å were determined.

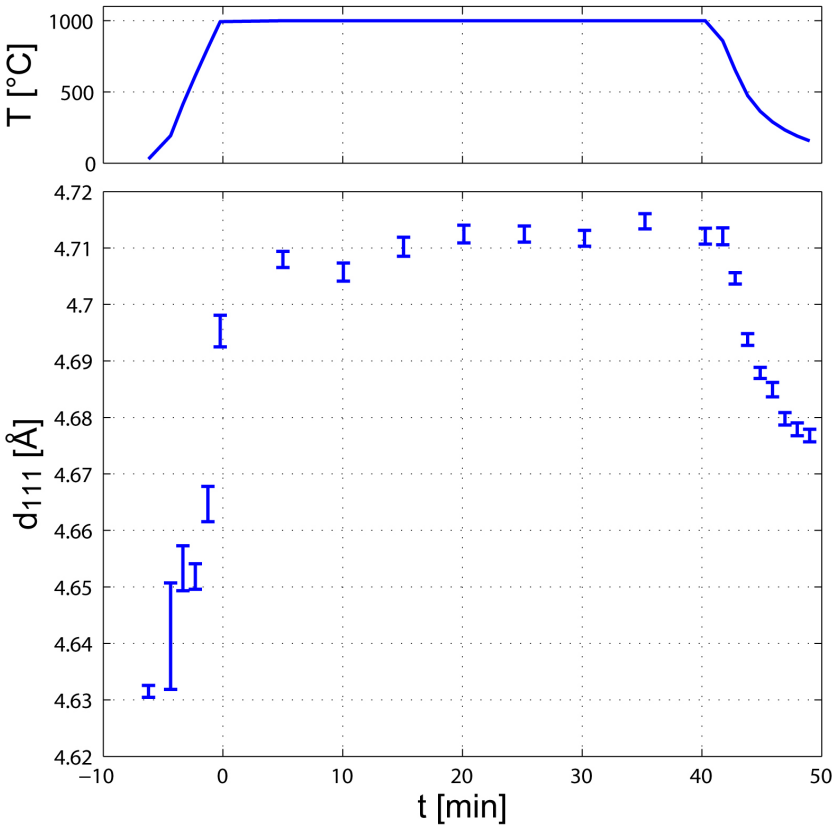

Figure 3.12: Corundum substrates three-layer setup: evolution of d_{111} of sample Cor21 during all four stages of the experiment. The upper graph displays the T_{sub} of the experiment using the same timescale as in the subimage below which presents the evolution of the lattice plane distance of the 111 spinel reflection. As expected, d_{111} increases upon heating and decreases upon cooling.

3.3 In-Situ Experiments — Periclase Substrates

3.3.1 Crystallization of the Al_2O_3 Reactant Layer and Onset of Spinel Growth

At the beginning of the experiments, it remained open to which polymorph the initially amorphous Al_2O_3 reactant layer will crystallize upon heating. In two experiments (samples Per26 and Per28) monitored at the EDDI beamline, a Bragg reflection at about 26 keV was detected during the heating stage that points to the crystallization of γ–Al_2O_3. A 3-D plot of experiment Per26 is presented in Figure 3.13. The 111 periclase substrate reflection at about 24.5 keV is prominent in all four spectra presented in Figure 3.13; the peak is shifted gradually towards slightly lower energies, i.e. higher lattice plane distances, due to the expansion of the lattice upon heating. Due to a slightly smaller lattice constant of γ–Al_2O_3 ($a_0 = 7.91$ Å; Zhou and Snyder, 1991) with respect to spinel ($a_0 = 8.084$ Å; Redfern et al., 1999), the 222 reflection of γ–Al_2O_3 is shifted towards a slightly higher energy with respect to the 222 reflection of spinel. As a defect spinel, γ–Al_2O_3 crystallizes also in the $Fd\bar{3}m$ space group (cf. section 1.2.2 on the crystal structure of spinels and information on γ–Al_2O_3). With respect to the cited lattice constant, the 222 reflection of γ–Al_2O_3 is expected at 25.97 keV or slightly less

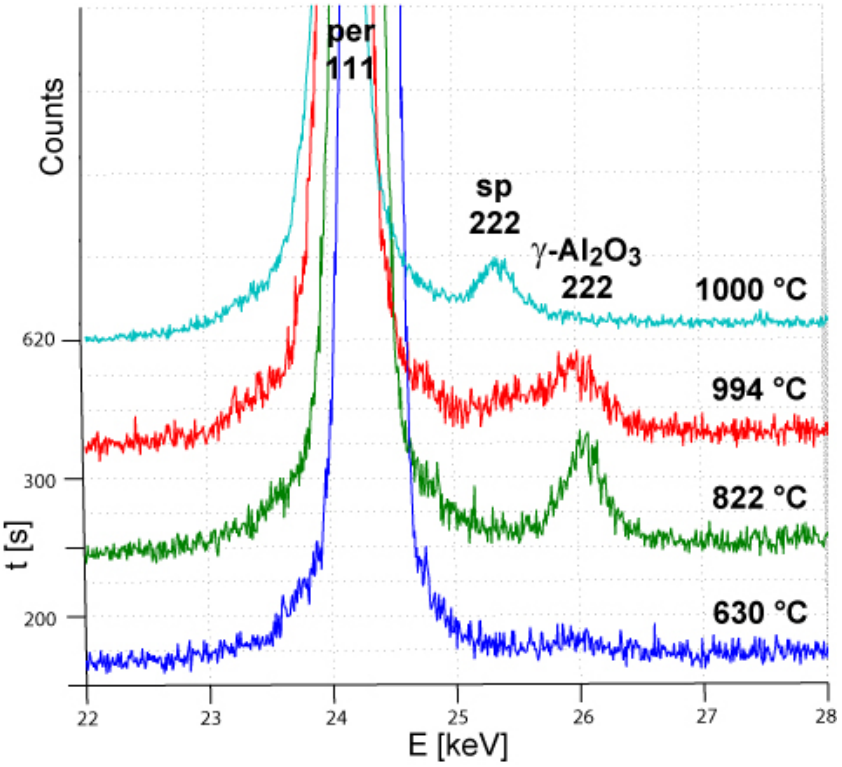

Figure 3.13: Crystallization of the amorphous Al_2O_3 reactant layer to γ–Al_2O_3, onset of spinel growth and rapid consumption of the reactant layer. The 3-D plot shows relevant parts between 22 and 28 keV of three spectra recorded during the heating stage (collected after 184, 247 and 309 seconds, respectively; $\Delta t = 60$ s) and the first spectrum recorded at target temperature 1000 °C (collected after 620 seconds; $\Delta t = 300$ s).

due to the expansion of the lattice at high temperatures. As can be seen in the spectrum recorded at 822 °C (green line in Fig. 3.13), a peak appeared at this position during the heating stage of this experiment. The γ–Al_2O_3 crystallized in the 60 seconds between the spectra recorded at 630 and 822 °C. The peak is relatively broad, pointing to the nanocrystallinity of the material. In the next spectrum recorded at 994 °C, it is indicated that the spinel-forming reaction takes place; because the intensity of the 222 γ–Al_2O_3 reflection decreased slightly and the 222 spinel reflection seems to emerge, part of the reactant layer was probably already used up in the 60 seconds between these two spectra. In the first spectrum at target temperature recorded 5 minutes later, the γ–Al_2O_3 reactant layer is already consumed and only the 222 spinel reflection can be seen.[2]

The γ–Al_2O_3 polymorph was also found in similar MgO/Al_2O_3 diffusion couples by Comer et al. (1966) and Sieber et al. (1996). The 222 Bragg reflection was observed because this reflection is dominated by the scattering from the rather well ordered oxygen sublattice, while the 111 reflection is contributed to by the two aluminum sublattices which are more disordered than the oxygen sublattice (Zhou and Snyder, 1991; Lippens and De Boer, 1964). The 111 reflection is thus rather diffuse and has a lower intensity.

[2]The sequence of crystallization and rapid consumption is similar for sample Per28. The broad reflection at 26 keV is at first observable in a spectrum recorded at 780 °C. The start of the reaction is indicated by the emergence of *hhh*-type spinel reflections in a spectrum recorded at 958 °C. In the first spectrum at 1000 °C, the γ–Al_2O_3 is again already consumed.

The general diffuse characteristic of the γ–Al_2O_3 powder pattern reflects a high degree of structural disorder of this polymorph (Zhou and Snyder, 1991). While the 111 reflection was absent, the 222 reflection was also observed by e.g. Wu et al. (2005) and Merckling et al. (2007) for epitaxial growth of γ–Al_2O_3 on (111)-oriented silicon.

The sequence of spectra in Figure 3.13 does not only demonstrate that supposedly γ–Al_2O_3 crystallized but also that the reaction rate was much faster in this setup compared to the experiments at 1000 °C using corundum substrates.

3.3.2 Spinel Growth in the Two-Layer Setup

The temperature was varied from 800 to 1000 °C; experiments were conducted at 800, 900 and 1000 °C for run durations of approximately 60 minutes in each case. Additional experiments differing in run duration were conducted at 1000 °C. An overview of samples and respective experimental parameters is given in Table A3 in the Appendix. A TEM foil was taken from all samples in this setup.

In-situ Experiment at 800 °C: The experiment at 800 °C was monitored at the KMC-2 beamline. Unlike the complementary experiment at 800 °C using corundum substrates, a reaction took place at this temperature using periclase substrates. The 111 spinel Bragg reflection started to emerge at target temperature but could not accurately be quantified until t = 4 min. The development of the peak with time is depicted in Figure 3.14a; the intensity of the peak remained relatively low during the course of the experiment. Figures 3.14b, 3.14c and 3.14d present the trends of I_{111}, d_{111} and of the $FWHM$ of the peak, respectively. Due to the low overall intensity, the data exhibits a pronounced scatter; however, the increase of I_{111} exhibits a parabolic trend, and the $FWHM$ was $> 1°$ even at the end of the experiment. This points to a steady but slow expansion as well as to the nanocrystallinity of the spinel layer. Using the Scherrer equation, the crystallite size was calculated to increase from 5 nm after 4 minutes at target temperature to only 8 nm at the end of the experiment. The d_{111} increased steadily with time from about 4.55 Å at the beginning to 4.63 Å at the end of the experiment.

The extent of the reaction band is hard to discern in TEM BF micrographs; HAADF images and EDX measurements served to discriminate between phases. Figure 3.15 shows such a HAADF image and two EDX measurements. Measurement 1 points to the existence of a thin spinel layer, the thickness of which was determined as 21 ± 1 nm. This layer is brighter than the reactant layer where in EDX measurement 2 almost only aluminum was found; the minor Mg-peak indicates that magnesium diffused into the reactant layer. This latter layer exhibits bright and dark patches; hence, this layer may be porous or nanocrystalline because darker areas represent less dense materials in the HAADF mode (nanocrystallinity is accompanied with a high percentage of grain boundaries). The initially amorphous Al_2O_3 layer crystallized supposedly to γ–Al_2O_3 as it was demonstrated in the previous subsection. Dark areas can also be found at the periclase/spinel phase boundary; this layer is designated as porous in Figure 3.15. The

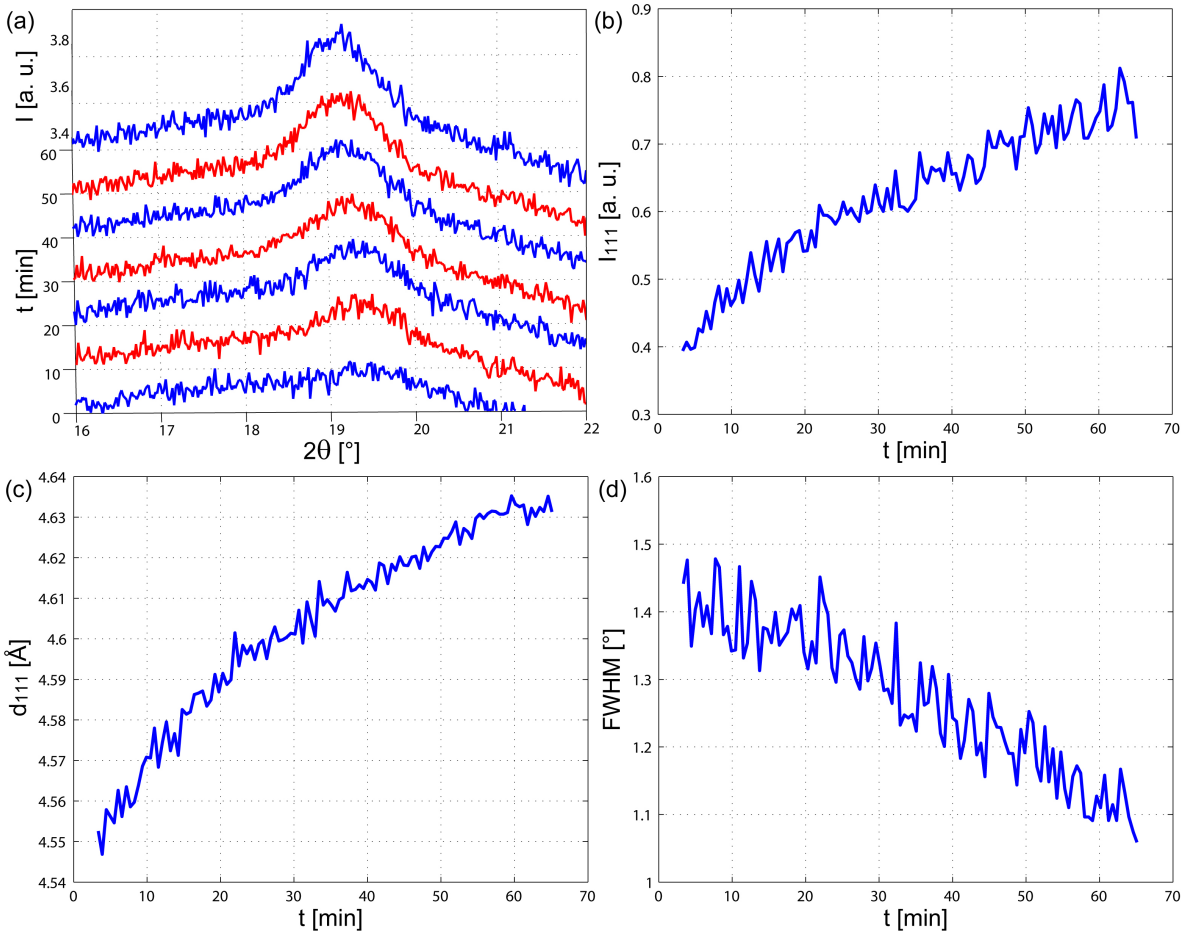

Figure 3.14: Periclase substrates two-layer setup: growth behavior at 800 °C. (a) 3-D plot: emergence of the 111 spinel Bragg reflection with time. Plotting approximately every 20th measurement, the period between two lines is 10 minutes. (b) The evolution of I_{111} exhibits a parabolic trend. (c) Evolution of the 111 spinel lattice plane distance. (d) Evolution of the *FWHM* of the 111 spinel reflection. The *FWHM* was always $> 1°$, pointing to the nanocrystallinity of the spinel layer.

porous layer appears to be rather discontinuous in this sample. This microstructure at the periclase/spinel phase boundary can be found in all periclase substrate experiments in which a reaction took place (this layer is presented in more detail in subsection 3.5.2 on special microstructures visible in TEM micrographs). Unlike the experiments using corundum substrates, bend contours are absent and the substrate/spinel interface is straight-lined.

In-situ Experiment at 900 °C: The experiment at 900 °C was monitored at the KMC-2 beamline. The 111 spinel Bragg reflection emerged notably in a measurement

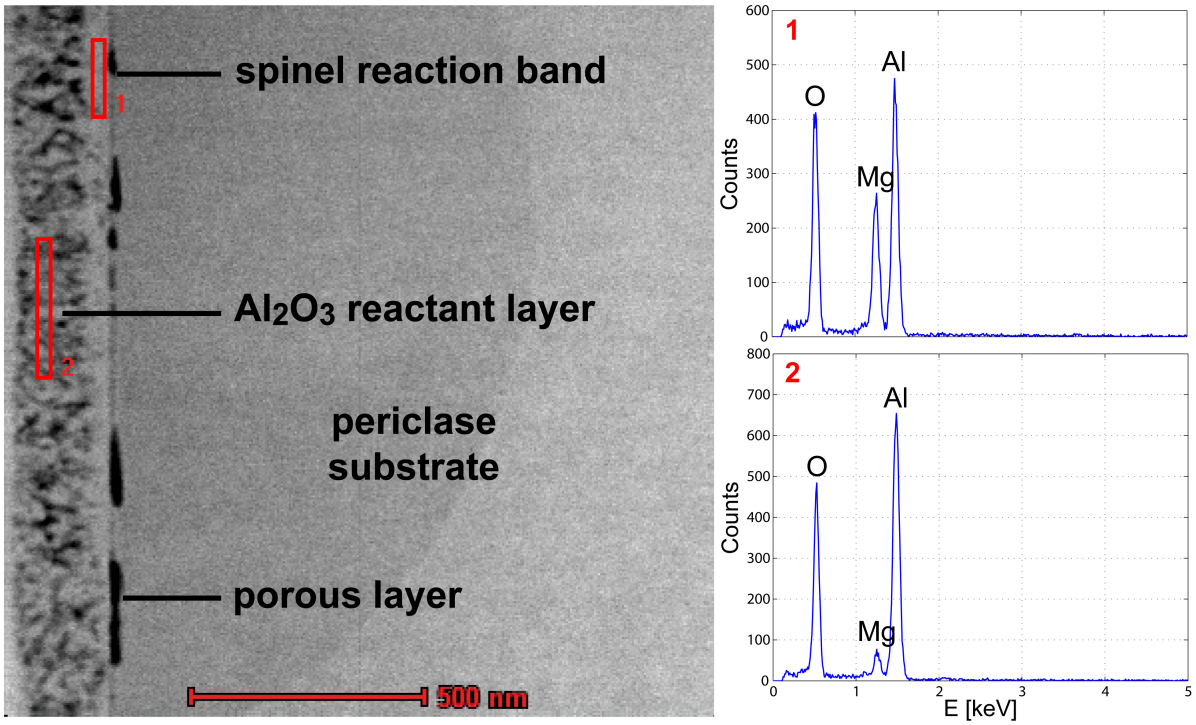

Figure 3.15: Periclase substrates two-layer setup: TEM analyses of the 800 °C experiment. HAADF micrograph on the left shows in red boxes areas of EDX measurements 1 and 2. Measurement 1 points to a thin layer of spinel between the reactants in accordance with the *in-situ* experiment. This layer is brighter than the reactant layer. Note scale bar at the bottom of the micrograph.

recorded at 895 °C, which was the last diffractogram recorded during the heating stage. Subsequently, the intensity of the reflection increased during the course of the experiment (Figs. 3.16a and 3.16b). The increase in I_{111} is linear for the first 20 minutes of the experiment but decelerates afterwards (Fig. 3.16b). Also the change in the 111 spinel lattice plane distance decelerates early in the experiment (Fig. 3.16c). Similar to the 800 °C experiment, the d_{111} exhibits an increasing trend, but now, d_{111} remains virtually unchanged during the last 30 minutes of the experiment, approaching a final value of 4.701 ± 0.001 Å. The evolution of the *FWHM* of the 111 spinel reflection is depicted in Figure 3.16d. Decreasing quickly during the first 20 minutes from $> 1°$ to $< 0.5°$, the *FWHM* remains virtually unchanged afterwards, approaching a final value of 0.45°.

Despite the steady increase of I_{111} until the end of the experiment, the trends of the 111 spinel lattice plane distance and especially of the *FWHM* of the reflection indicate that the reactant layer was consumed after 20 to 30 minutes. In line with the assumption of early consumption, no relics of a reactant layer was found in subsequent TEM analyses (visual inspection as well as EDX measurements). A TEM BF image is presented in Figure 3.17. The deceleration of the I_{111} increase may then be due to a dwindling

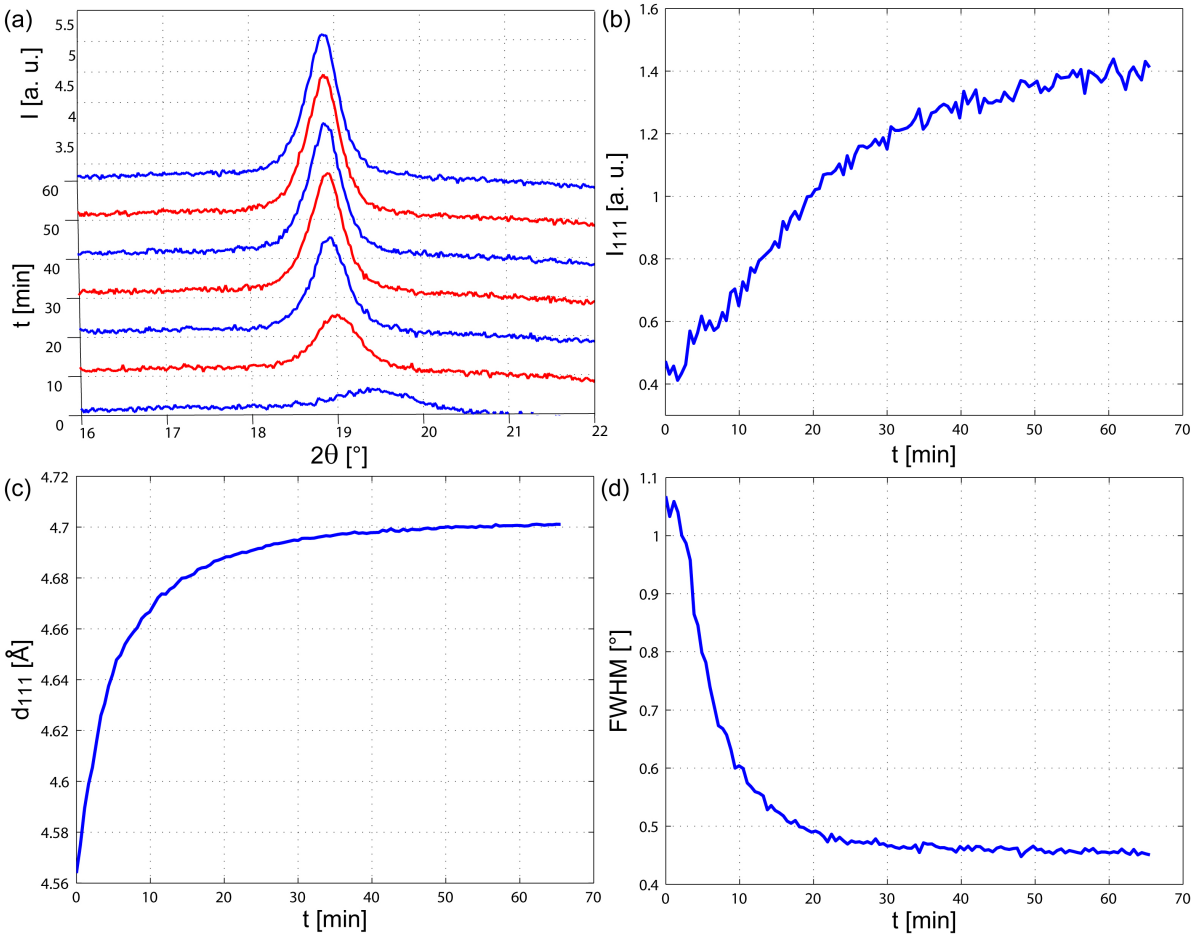

Figure 3.16: Periclase substrates two-layer setup: growth behavior at 900 °C. (a) 3-D plot: emergence of the 111 spinel Bragg reflection with time. Plotting approximately every 20th measurement, the period between two lines is 10 minutes. (b) Evolution of I_{111}. (c) Evolution of the 111 spinel lattice plane distance. (d) Evolution of the *FWHM* of the 111 spinel reflection.

reactant layer as it was suggested for sample Cor8 (cf. Fig. 3.7). Additionally, it is also possible that due to recrystallization processes the fraction of {111}-oriented spinel crystallites increased upon further annealing, i.e. 'misoriented' areas were consumed or rotated into the {111} out-of-plane orientation. The different shades of grey in the spinel layer presented in Figure 3.17 and also a DF image of the same area indicate that spinel orientations indeed are not strictly fixed across this reaction band.

A few elongated spinel crystallites can be discerned in the TEM micrograph. Their width is 40 to 50 nm. Their grain boundaries are perpendicular to the periclase/spinel phase boundary and terminate at the surface of the sample, strengthening the assumption that no reactant layer is present anymore. A porous or less dense layer can be seen at the

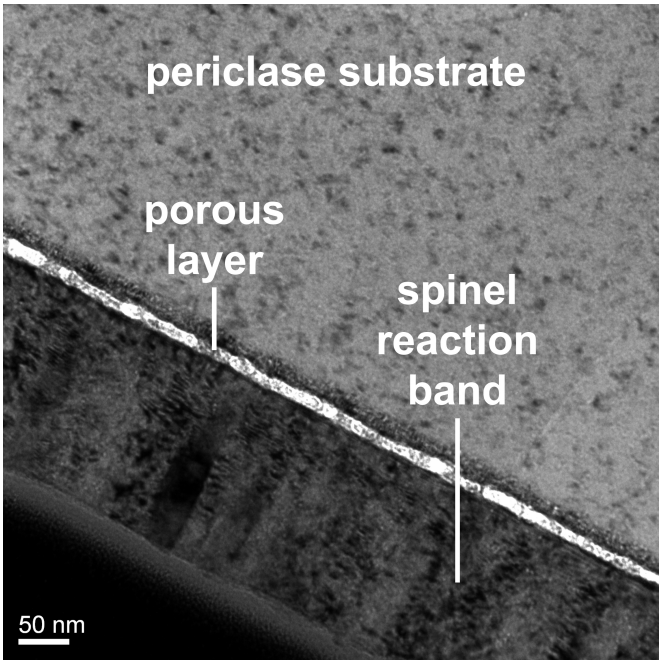

Figure 3.17: Periclase substrates two-layer setup: TEM BF image of the 900 °C experiment. No relics of the reactant layer were found. Some elongated crystallites can be discerned. Their width is 40 to 50 nm. Their grain boundaries are perpendicular to the periclase/spinel phase boundary and terminate at the surface of the sample. Typical for the periclase substrate samples, a porous layer can be seen at the periclase/spinel interface, which is also always straight-lined.

substrate/spinel phase boundary. This interface is again straight-lined. A microstructure that points to different sublayers inside the spinel reaction band could not be clearly observed in micrographs obtained from this sample.

Excluding the porous layer at the phase boundary, the thickness of the spinel layer was determined as 182 ± 3 nm. Assuming a linear growth law and consumption of the reactant layer after 30 minutes, the spinel growth rate was 6.1 nm/min in this experiment.

In-situ Experiments at 1000 °C: It has been demonstrated in the previous subsection on the crystallization of the Al_2O_3 reactant layer and the onset of spinel layer growth that reaction rates at 1000 °C were very high; EDDI spectra indicated that the reactant layer was already consumed after 5 minutes when the first spectrum at target temperature was recorded (cf. Fig. 3.13). In accordance with the *in-situ* experiments, a residual Al_2O_3 reactant layer was never found in subsequent TEM analyses. This may be illustrated by sample Per24 which was annealed for only 5 minutes — the shortest run duration of the 1000 °C experiments. A HAADF micrograph and two exemplary EDX measurements conducted in two microstructurally different sublayers of the run product are presented in Figure 3.18; only spinel was found in both sublayers. Excluding the porous layer at the periclase/spinel phase boundary, the total spinel layer thickness was determined as 271 ± 1 nm. The HAADF micrograph in Figure 3.18 appears similar to the one presented in Figure 3.15; on top of the periclase substrate follows a porous layer, then a bright, inner sublayer and finally a dark-stained, thicker, outer sublayer. Although this outer sublayer may look similar in both samples, the chemical signature is different. In the previous sample almost only aluminum was found in the outer sublayer, pointing

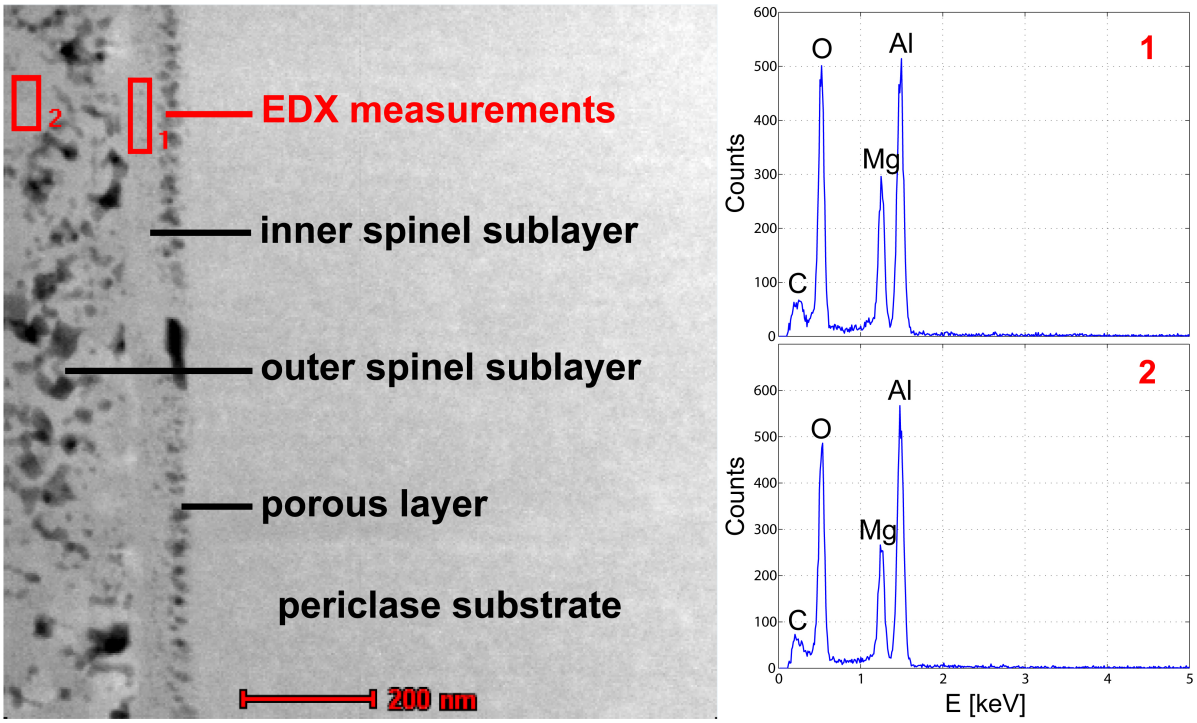

Figure 3.18: Periclase substrates two-layer setup: TEM analyses of a 1000 °C experiment. In the HAADF micrograph on the left three microstructurally different layers can be distinguished: a dark-stained, outer spinel sublayer where EDX measurement 2 was conducted, a bright, inner spinel sublayer where EDX measurement 1 was conducted and a porous layer at the periclase/spinel interface. EDX measurements 1 and 2 presented on the right point to spinel; no residual Al_2O_3 reactant layer was found. Note scale bar at the bottom of the micrograph.

to the existence of a thick residual reactant layer. In the present sample, however, EDX measurements were performed in bright as well as in dark areas of the outer sublayer and always spinel was found, indicating that the reactant layer was consumed within 5 minutes of annealing at 1000 °C.

The Al_2O_3 reactant layer was always consumed after 5 minutes; from the experiments conducted at 1000 °C it cannot be better resolved at which point the reaction was exactly completed. Assuming a linear growth law and consumption of the reactant layer after 5 minutes, the spinel growth rate for the sample presented in Figure 3.18 was at least 54.2 nm/min. Following the same assumptions, the determined spinel layer thicknesses for the other two 1000 °C experiments result in linear growth rates of at least 36.2 and 39.4 nm/min. The mean of these three values is then 43.3 nm/min, corresponding to 0.72 nm/s.

Evolution of Lattice Plane Distances and Peak Widths: An overview of 111 spinel lattice plane distances, *FWHM/I_Bs* and crystallite sizes at the end of the experiments in this setup is presented in Table 3.4. The mean 111 spinel lattice plane distance derived from the 1000 °C experiments is 4.691 ± 0.009 Å. The value at 900 °C seems to be in the same order or even higher with 4.701 ± 0.001 Å whereas it is sufficiently less in the experiment at 800 °C with 4.631 ± 0.002 Å.

The evolution of the 111 spinel lattice plane distances and *FWHMs* for the experiments at 800 and 900 °C were presented in Figures 3.14 and 3.16, respectively. The 111 spinel lattice plane distances exhibited increasing trends in the low temperature experiments accompanied by a decrease of the *FWHM*. In contrast, the 111 spinel lattice plane distance and the *FWHM* remained relatively constant during the course of the 1000 °C experiments, supporting the assumption of very fast reaction rates and an early consumption of the reactant layer.

Table 3.4: Periclase two-layer setup: overview of lattice plane distances, *FWHMs* (KMC-2) or *I_Bs* (EDDI) and crystallite sizes determined from the 111 spinel Bragg reflections, respectively.

Sample	d_{111} [Å]	FWHM [°]	D [nm]
Per27 (900 °C; 65.5 min)	4.701 ± 0.001	0.45	18
Per29 (800 °C; 65.1 min)	4.631 ± 0.002	1.06	8
Sample	**d_{111} [Å]**	**I_B [°]**	**D [nm]**
Per24 (1000 °C; 5 min)	4.700 ± 0.001	0.46	12
Per26 (1000 °C; 60.4 min)	4.683 ± 0.001	0.33	17
Per28 (1000 °C; 30.2 min)	4.690 ± 0.004	0.33	17

3.3.3 Spinel Growth in the Three-Layer Setup

In the three-layer setup, experiments were conducted at 700, 800, 900 and 1000 °C for run durations of approximately 40 minutes in each case. Two additional experiments differing in run duration were carried out at 1000 °C. An overview of samples and respective experimental parameters is given in Table A3 in the Appendix. A representative texture measurement was conducted and two TEM foils were prepared.

In-situ Experiment at 700 °C: No additional growth was observable at 700 °C; the I_{111} remained constant during the experiment, albeit exhibiting a marked scatter due to the low overall intensity. The position of the peak varied similarly, but no trend can be deduced; the mean of the 111 spinel lattice plane distance at 700 °C is 4.767 ± 0.006 Å.

In-situ Experiment at 800 °C: Similar to the two-layer setup where growth occured at 800 °C, an expansion of the seed layer is suggested for this experiment. The I_{111} rose markedly during the course of the experiment (Fig. 3.19a). The scatter of the data is attributed to the supposed minuteness of this reaction band. In the two-layer setup, it has been demonstrated that the reaction layer attained a thickness of only 21 ± 1 nm and the data varied likewise (cf. Figs. 3.14 and 3.15). Unlike this experiment, in which the 111 spinel lattice plane distance increased steadily to a final value of 4.631 ± 0.002 Å after 60 minutes, a decreasing trend was observed in the three-layer setup (Fig. 3.19b); the final value was 4.718 ± 0.003 Å.

In-situ Experiment at 900 °C: The increase of I_{111} was more pronounced in this experiment (Fig. 3.19c), pointing to enhanced reaction kinetics at 900 °C. Accordingly, the overall intensity is higher, and the scatter of the data points is greatly reduced compared to the former experiment at 800 °C. The I_{111} increased linearly with time. The fall of the 111 spinel lattice plane distance was more pronounced at 900 °C also; the d_{111} decreased asymptotically from 4.747 Å in the first measurement of the experiment, approaching a final value of 4.684 ± 0.001 Å at the end of the run (Fig. 3.19d). The *FWHM* fell until the end of the experiment, approaching a final value of 0.37°. The calculated crystallite size increased linearly with time from 9 to 21 nm.

The steadily increasing I_{111} and the steadily decreasing *FWHM* indicate that a reactant layer was still present after 40 minutes. The subsequent TEM analyses confirmed this assumption. The different layers are best discernible in HAADF micrographs; an example is presented in Figure 3.20a. In this and in the subimage below it may be best illustrated how growth supposedly occured in the two setups using periclase substrates (most of the individual layers and microstructures are also visible in previous micrographs presented, cf. Figs. 3.15, 3.16a, 3.18). The phase boundary between the periclase substrate and the spinel reaction layer marks the usual porous layer. The periclase substrate/spinel interface is straight-lined illustrating that growth in this direction occured uniformly. On top of the porous layer, which has a uniform thickness of about 45 nm, follows a homogeneous bright spinel layer. The extent of the seed layer is not visible in this foil, but it should be located inside this bright layer (cf. subimage below). The bright areas protrude unevenly distributed towards the top into the Al_2O_3 reactant layer, highlighting that growth in this direction varied markedly; accordingly, the reactant layer protrudes unevenly distributed towards the substrate. The extent of the reactant layer is approximately equivalent with the dark-stained areas that prevail at the surface of the sample. EDX measurements on top of the homogeneous bright layer, i.e. in the alternating bright and dark-stained areas, yielded signals of aluminum and magnesium, but the magnesium content was always too low for spinel; thus, these measurements are interpreted to be mixed signals emanating from spinel as well as from the Al_2O_3 reactant layer or merely from magnesium that diffused through the abundant grain boundaries into the reactant layer. The further away towards the surface of the sample the less magnesium

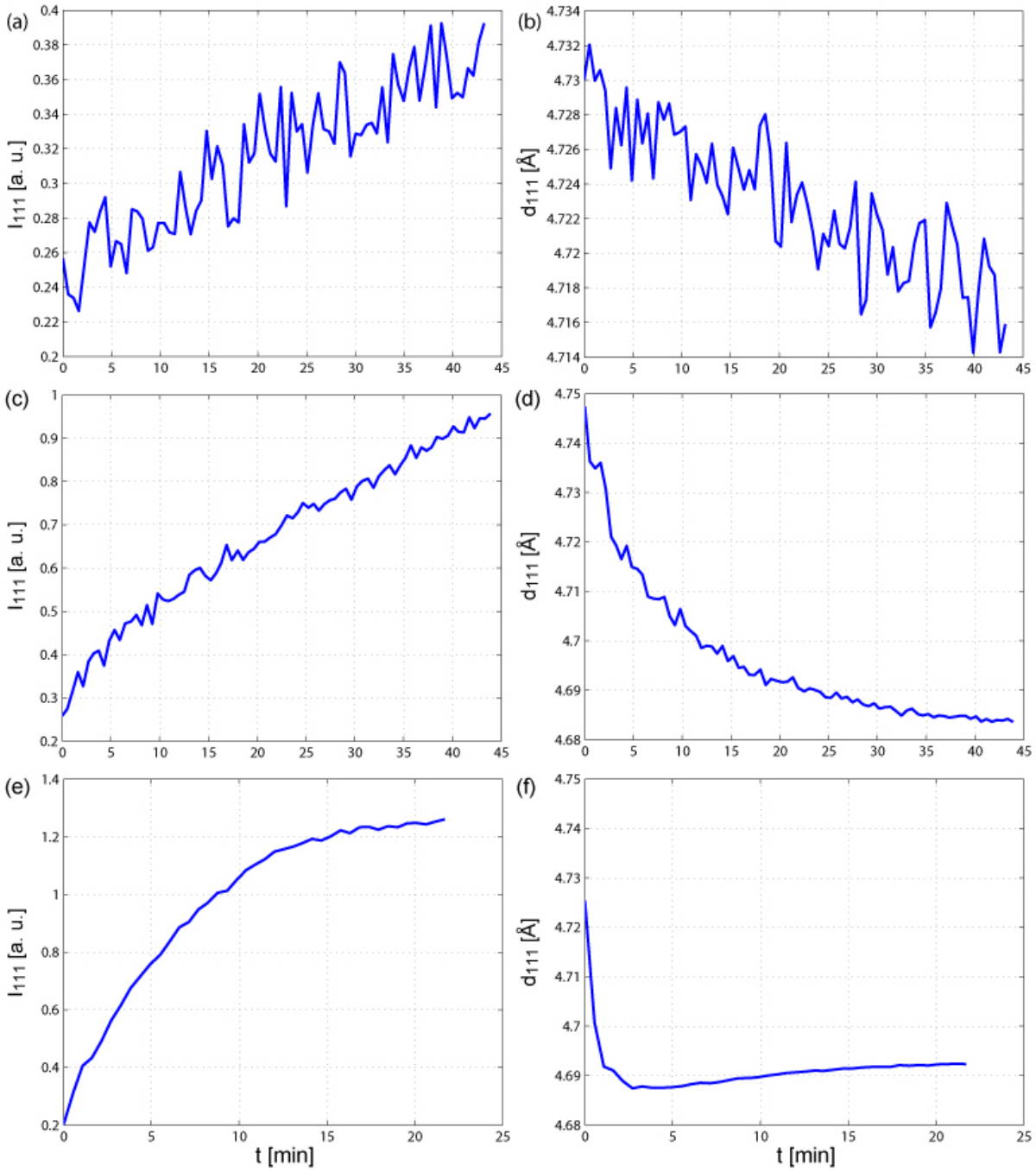

Figure 3.19: Periclase substrates three-layer setup: growth behavior at 800, 900 and 1000 °C in terms of the evolution of I_{111} (left column) and the 111 spinel lattice plane distance (right column). (a, b) 800 °C experiment. (c, d) 900 °C experiment. (e, f) 1000 °C epxeriment.

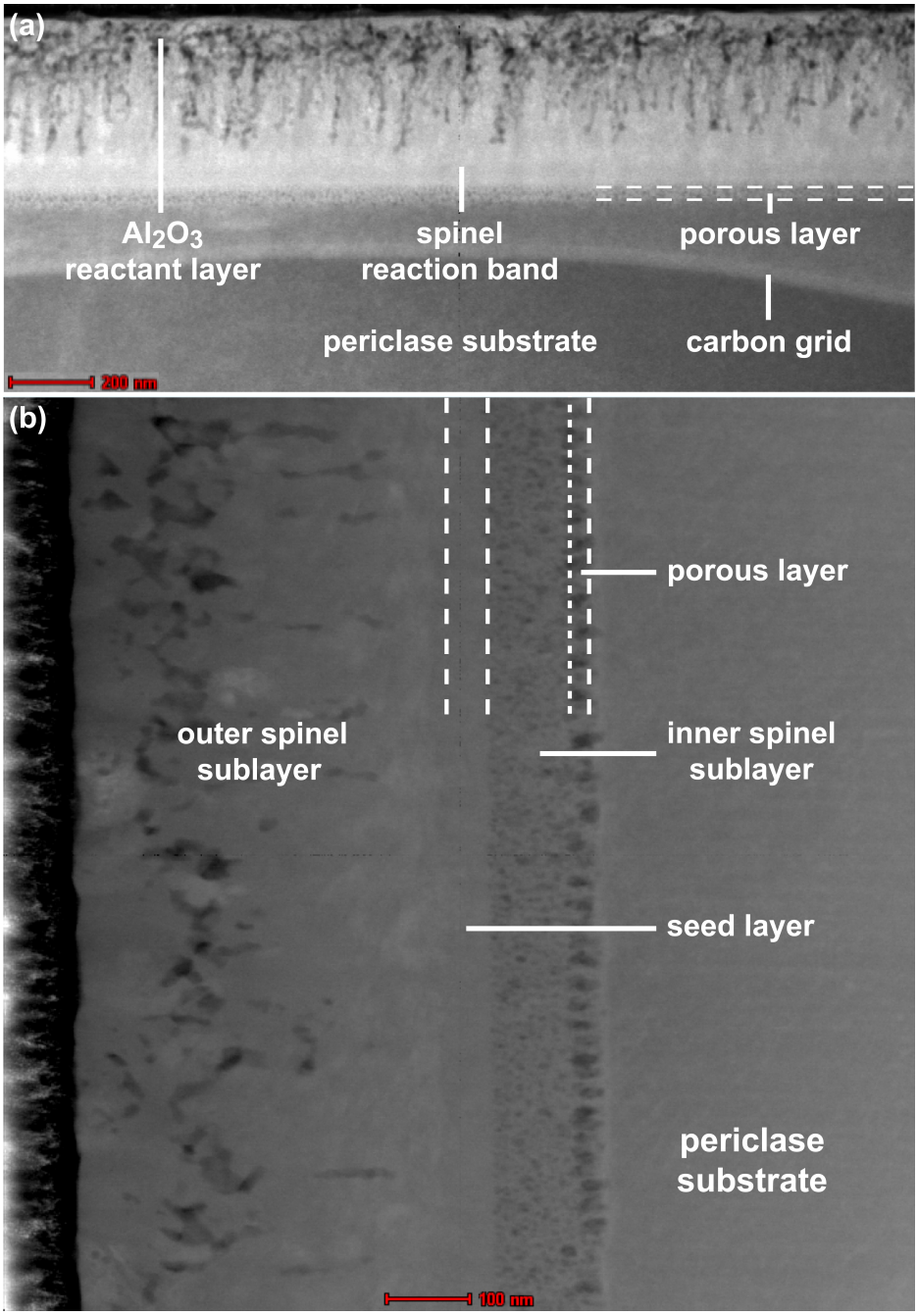

Figure 3.20: Periclase substrates three-layer setups: TEM analyses of the 900 and 1000 °C experiments. (a) HAADF micrograph of the 900 °C experiment. (b) HAADF micrograph of the 1000 °C experiment. The extent of the individual sublayers is marked by dashed lines. Note scale bars at the bottom of the images.

was found. The Al_2O_3 reactant layer remained nanocrystalline; larger grains were never discernible unlike it was the case for the periclase reactant layer (cf. Fig. 3.6c and 3.6d).

In summary, the growth front into the periclase substrate proceeded highly uniform whereas that into the reactant layer highly non-uniform. This non-uniform growth into the reactant layer prohibits the accurate determination of a mean spinel layer thickness. However, the bright area may exceed 200 nm. A layer thickness of roughly 300 nm is expected when applying the growth rate of 6.1 nm/min determined from the complementary experiment in the two-layer setup.

In-situ Experiment at 1000 °C: The complementary 40-minutes experiment at 1000 °C was monitored at the EDDI beamline, but no reflections of the thin films were detected during the run. However, TEM analyses proved that the reaction was completed during the run. Inspecting HAADF micrographs, the seed layer is well discernible inside the reaction band due to different shades of grey with respect to adjacent sublayers; an example is presented in Figure 3.20b. The seed layer is situated between an inner and an outer spinel sublayer, indicating that the inner sublayer is periclase-grown and the outer sublayer is Al_2O_3-grown. The seed layer, the inner and the outer sublayer have thicknesses of 62 ± 2, 133 ± 5 and 424 ± 15 nm, respectively. The inner spinel sublayer is divided into two layers with different porosities. The porosity is more pronounced in a layer immediately adjacent to the substrate whereas it is somewhat spotted in the remaining part of the inner sublayer (this boundary is marked by a dashed line in Figure 3.20b). On the other hand, the porosity in the outer sublayer, which is present especially towards the sample surface (the dark areas inside the outer spinel sublayer), is probably inherited from the nanocrystalline γ–Al_2O_3 layer. This assumption is deduced from the microstructures presented in previous HAADF micrographs in which these dark patches are also present and predominantly Al_2O_3 was found in EDX measurements (Figs. 3.15 and 3.20a).

Because the experiment at the EDDI beamline failed, the evolution of I_{111} and the lattice plane distance at 1000 °C may be presented using data of sample Per22 monitored for about 20 minutes at the KMC-2 beamline. The I_{111} increased quickly at the beginning of the run but decelerated markedly after about 10 minutes and stayed more or less constant during the final minutes, suggesting that the reaction was completed (Fig. 3.19e). This assumption is strengthened by the evolution of the *FWHM* and the deduced crystallite size; the crystallite size increases quickly from 12 nm at the beginning of the experiment until it remains virtually unchanged after 14 minutes, reaching a final value of 55 nm. The 111 spinel lattice plane distance rises during the heating stage, falls abruptly after target temperature is reached, i.e. when the reaction takes place, and increases slightly afterwards (Fig. 3.19f). This is dissimilar to the former experiments conducted at lower temperatures in which d_{111} strictly decreased at target temperature.

Sample Per20, monitored for only about 10 minutes at 1000 °C, yielded similar results to the previous sample, but the steady increase of I_{111} as well as of the crystallite size

until the end of the experiment suggests that the reaction was not completed during this short time span. Also the evolution of the 111 spinel lattice plane distance was similar.

Evolution of Lattice Plane Distances and Peak Widths: An overview of 111 spinel lattice plane distances, *FWHMs* and crystallite sizes at the end of the experiments in this setup is presented in Table 3.5. Strikingly, at 700 °C, the highest lattice plane distance is found. Accordingly, at higher temperatures, d_{111} becomes smaller. This behavior can be deduced from the steady decrease of the distance when the reaction takes place at target temperature. The higher the temperature the more pronounded d_{111} falls.

Table 3.5: Periclase three-layer setup: overview of lattice plane distances, *FWHMs* and crystallite sizes determined from the 111 spinel Bragg reflection, respectively.

Sample	d_{111} [Å]	FWHM [°]	D [nm]
Per18 (900 °C; 43.9 min)	4.684 ± 0.001	0.37	21
Per19 (800 °C; 43.2 min)	4.718 ± 0.003	0.70	11
Per20 (1000 °C; 11.4 min)	4.688 ± 0.001	0.17	46
Per21 (700 °C; 41.9 min)	4.767 ± 0.006	0.69	12
Per22 (1000 °C; 21.7 min)	4.692 ± 0.001	0.15	55

3.4 Texture Measurements

The macrotexture determined at the KMC-2 beamline and DPs obtained from selected area electron diffraction (SAED) measurements using TEM will be presented in the following two subsections.

3.4.1 Corundum Substrates

In all three experimental setups, the {111} pole figures confirm that the substrate/thin film out-of-plane orientation relationship is (0001) corundum || (111) spinel; maximum intensities were always found in the center of the pole figures, i.e. at $\alpha = 0$, and no other sharp spots appeared in the remaining parts of these pole figures (poles that are geometrically related to those {111}-oriented crystallites would be expected at $\beta = 70.5°$, but this outer part of the pole figure was not measured). These {111}-oriented crystallites possess distinct in-plane orientations as it is observable in {311} pole figures. Due to the angular relationships in the cubic crystal system, the {311} lattice planes are expected at $\alpha = 29.5°$ for all the grains that crystallized {111}-oriented. Six sharp spots at this position can indeed be seen in the {311} pole figures; they appear at regular distances of $\beta = 60°$.

These observations are presented in Figure 3.21. In Figures 3.21a and 3.21b are the {111} and {311} pole figures of the one-layer setup shown; this sample was annealed for 6 minutes at 1000 °C. The two half pole figures differ not much from the pole figures presented below in Figures 3.21c and 3.21d (measurements for sample Cor22 annealed for 2 hours at 1000 °C). Both {311} half pole figures exhibit three sharp spots in the measured interval of $\phi = 0$–$180°$. Due to the general central symmetry of the texture measurements, six spots are present at $\alpha = 29.5°$ when the full circle $\phi = 0$–$360°$ is measured. This can be seen in Figure 3.21f which shows a {311} pole figure of sample Cor16 (annealed for 40 minutes at 800 °C); the corresponding {111} pole figure of this sample is presented in Figure 3.21e.[3]

The difference between the measurements in Figure 3.21 is the degree of texture which is strongest for sample Cor22; the spot in the center of the {111} pole figure and those in the {311} pole figure possess relatively higher intensities compared to the interjacent areas in the plots. The degree of preferred orientation can be quantified by the texture toolbox MTEX by calculating a texture index (TI) which is determined from the orientation distribution function (ODF). The TI is consequentially highest for sample Cor22 with 13.6, but it is only 2.8 and 2.7 for samples Cor10 and Cor16, respectively.

Usually sharp spots were observed in the {311} pole figures such as they are presented in Figures 3.21b, 3.21d and 3.21f. In contrast, in all three samples in which the MgO reactant layer was consumed during the *in-situ* experiment (samples Cor8, Cor9 and Cor30), six triangular shapes are visible in the {311} pole figures, which also appear at regular distances of $\beta = 60°$. This observation is presented in Figure 3.22 for sample Cor9 for which additionally an {110} pole figure was measured. The wide spot in the center of the {111} pole figure and the triangles in the {110} and {311} pole figures indicate that the out-of-plane as well as the in-plane orientations of the crystallites are not strictly fixed anymore but that they can vary to some extent. A deviation from the exact [111] out-of-plane direction is indicated by the wide spot in the center of the {111} pole figure which extends evenly to ψ-values of 5°, meaning that crystallites are slightly tilted and/or twisted against each other. This tilt and/or twist is also indicated in the {110} and {311} pole figures due to the angular distribution of the poles in the triangles along α and β. However, judging from the TI of 17.6, this sample has still a relatively strong texture (likewise, sample Cor8 has also a strong texture with a TI of 15.4).

The parallelism of certain crystallographic directions of the phases is visible in DPs. Diffraction spots in DPs demonstrate that $<10\bar{1}0>$ corundum $||$ $<110>$ spinel $||$ $<110>$ periclase, indicating that directions of close packing within the planes of close-packed oxygen ions lie parallel; such a DP is presented in Figure 3.23. The proximity of the 220 periclase, 440 spinel and $30\bar{3}0$ corundum diffraction spots indicate that the corun-

[3]Rings with increased intensities in {111} pole figures — especially visible at $\alpha = 60°$ — are most likely measurement artifacts because they are not displaced when the substrate had a miscut; this is in particular observable for the periclase substrates presented in the next subsection (cf. Fig. 3.24) in which — due to the increased miscut of those samples — the {111} and {311} poles in the respective polar plots are sightly displaced (they lie not at $\alpha = 29.5°$ in {311} pole figures) but the rings are not.

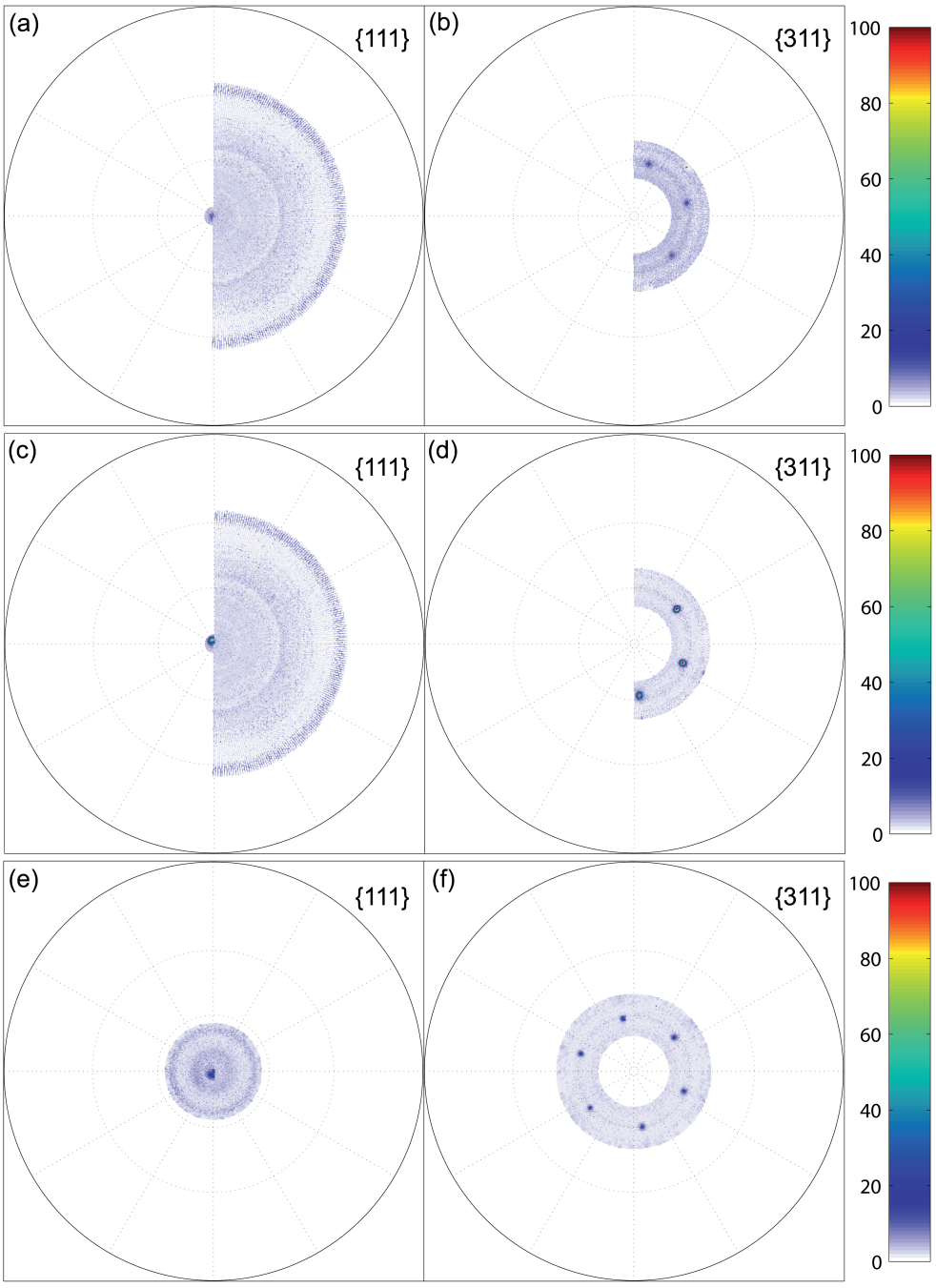

Figure 3.21: Corundum substrates: {111} and {311} pole figures (stereographic projections; normalized intensities). (a, b) One-layer setup (sample Cor10 annealed for 6 minutes at 1000 °C). (c, d) Three-layer setup (sample Cor22 annealed for 120 minutes at 1000 °C). (e, f) Three-layer setup (sample Cor16 annealed for 40 minutes at 800 °C).

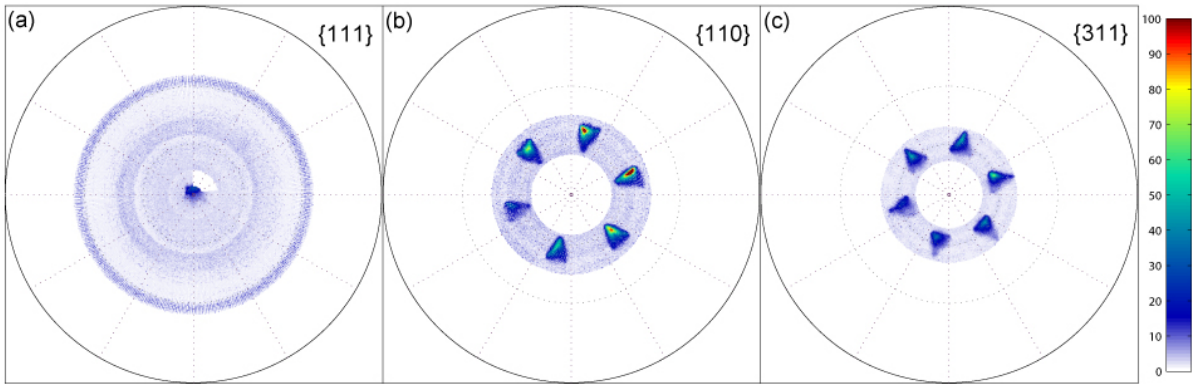

Figure 3.22: Pole figures of sample Cor9. (a) {111}, (b) {110} and (c) {311} pole figures (stereographic projections; normalized intensities). Triangular shapes instead of sharp spots are visible in {311} pole figures in all samples in which the MgO reactant layer was consumed during the experiment.

dum/spinel as well as the spinel/periclase lattice misfit is small. Using $f = (a_s - a_f) / a_s$, where f is the lattice misfit and a_s and a_f are the substrate and film lattice sizes along their close packed directions, respectively, the corundum/spinel lattice misfit amounts to –3.6 %. Similar values were reported by Rossi and Fulrath (1963) and Jeřábek et al. (2014). Using the cell parameters for corundum and spinel from the literature (sections

Figure 3.23:
Diffraction pattern of sample Cor18. The DP illustrates that an in-plane alignment between the three phases exists. Indexed spots demonstrate that the close-packed directions in the planes of close-packing of the phases lie parallel. However, periclase diffraction spots are somewhat smeared. The direct beam is denoted by 000.

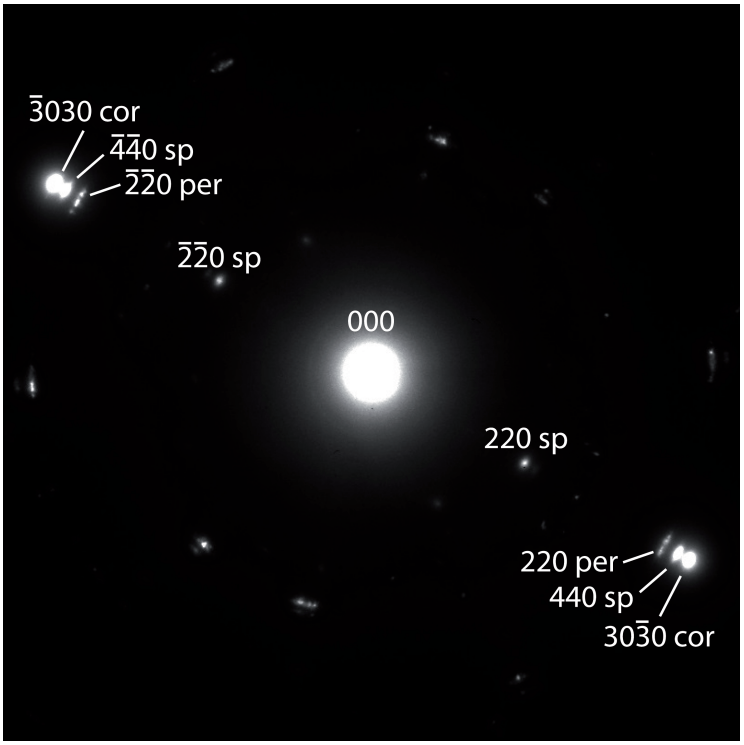

1.2.2 and 2.1.1) a misfit of –4.1 % is derived for these lattice planes, indicating that the spinel lattice is slightly strained to reduce the mismatch.

To summarize, pole figures and DPs along with EDDI spectra prove that the spinel layers grew topotaxially into the corundum substrates and the periclase reactant layers; directions of close packing within the planes of close-packed oxygen ions are parallel. A pronounced tilt and/or twist of the spinel crystallites is indicated in pole figures of samples in which the reactant layer was consumed.

3.4.2 Periclase Substrates

All pole figures of the periclase substrates exhibit sharp spots, illustrating that the spinel layers grew topotaxially into the substrates and the reactant layers. Due to the increased miscut of the periclase substrates (cf. section 2.1.2), these spots appear slightly displaced in α in the pole figures, i.e. not exactly in the center of {111} pole figures and not at $\alpha = 29.5^\circ$ in {311} pole figures. However, similar to the corundum substrates, a high intensity spot is present near the center of {111} pole figures, and six spots appear at regular distances of 60° in {311} pole figures. This is presented for the two-layer setup in Figure 3.24 for samples Per24 and Per26 annealed for 5 and 60 minutes, respectively (a HAADF micrograph of sample Per24 was presented in Fig. 3.18 on page 66). These specimens have TIs of 41.9 and 125.9, respectively, highlighting that the texture is strong and that the amount of oriented crystallites increases with run duration.

Only one sample was measured in the three-layer setup (sample Cor17 annealed for 40 minutes at 1000 °C; a HAADF micrograph of this sample was presented in Figure 3.20b on page 70, showing the inner and outer spinel sublayers as well as the seed layer in between); the two pole figures are presented in Figure 3.25a and 3.25b. The usual sharp spots are smeared in both measurements, but the sample has nevertheless a strong texture with a TI of 59.7. Additionally, three DPs were collected during TEM analysis. A DP collected at the periclase substrate/inner spinel sublayer interface is presented in Figure 3.25c; the DP proves that identical crystallographic directions of the phases are highly parallel. Some diffraction spots are indexed in Figure 3.25c; it can be seen that [100] periclase || [100] spinel, [011] periclase || [011] spinel and [111] periclase || [111] spinel. However, this exact orientation of the spinel crystallites becomes successively lost the further away from the periclase substrate the measurement is taken. A DP collected in the outer spinel sublayer is presented in Figure 3.25d. Periclase diffraction spots are absent in this DP, and the spinel diffraction spots are smeared towards a ring pattern, i.e. intensities are now pronounced over a certain angular range. This indicates that the texture is weaker in the outer spinel sublayer which replaced the Al_2O_3 reactant layer. An additional DP collected in the area of the spinel seed layer exhibits an intermediate stage of texture; the same spinel diffraction spots as in Figure 3.25c can be seen, but they show a tendency towards smearing such as in Figure 3.25d. As the diameter of the incident beam was about 150 nm, not only the seed layer was analyzed in this intermediate DP but probably also the outer spinel sublayer.

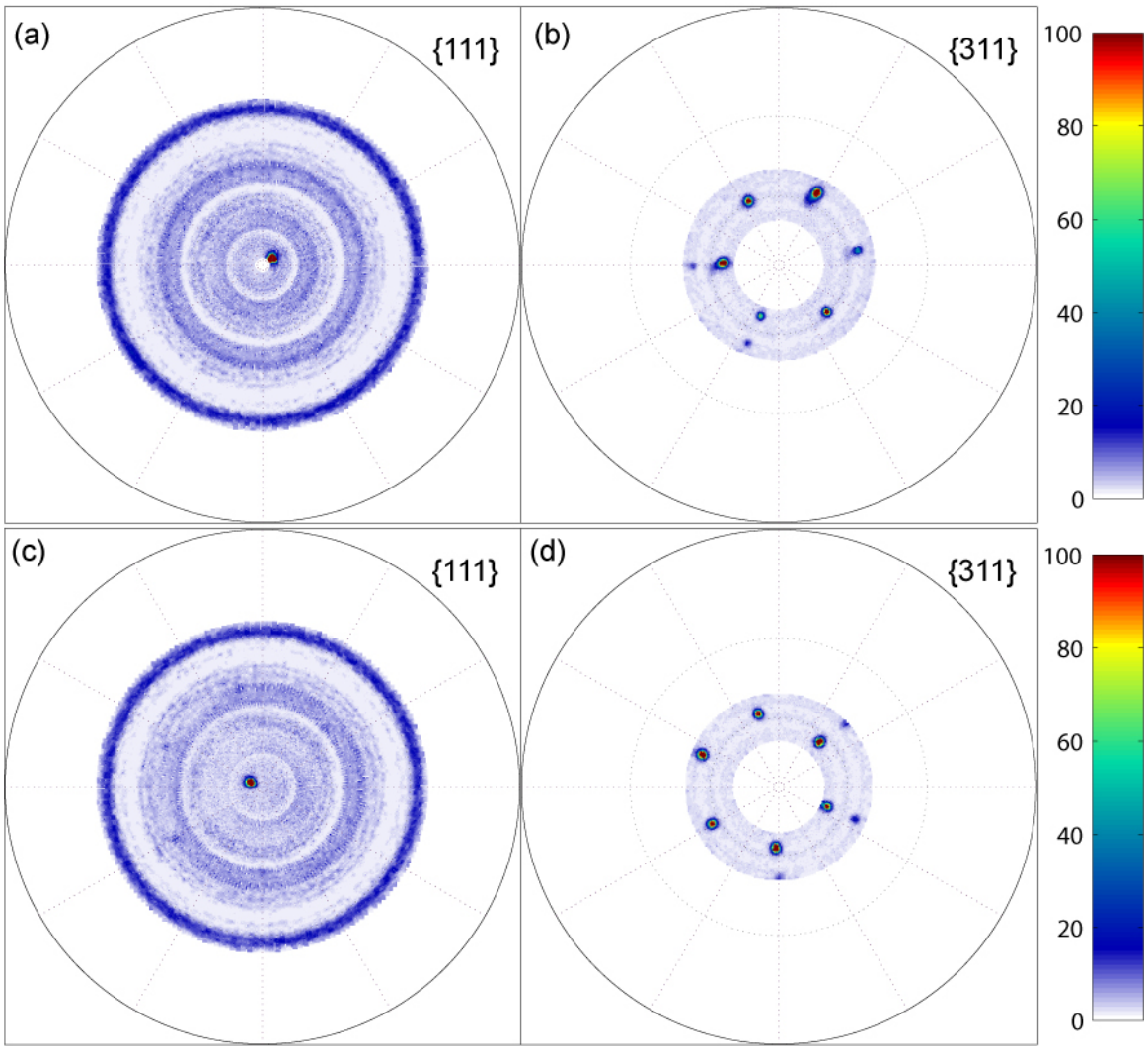

Figure 3.24: Periclase substrates two-layer setup. (a, c) {111} and (b, d) {311} pole figures (stereographic projections; normalized intensities) of samples Per24 (upper panel) and Per26 (lower panel), respectively. Sharp spots are visible in the pole figures. Due to the miscut of the periclase substrates, these spots are slightly displaced from their expected positions (but the intensive blue ring at $\alpha = 60°$ is not).

From the periclase and spinel diffraction spots in Figure 3.25c the lattice misfit was determined as +4.2 %. Similar values for the general lattice misfit between spinel and periclase were reported by Comer et al. (1966), Hesse et al. (1994), Sieber et al. (1996), Sieber et al. (1997) and Jeřábek et al. (2014). Using the cell parameters for periclase and spinel from the literature (sections 1.2.2 and 2.1.2), a misfit of +4.0 % is derived for these lattice planes, indicating that the spinel lattice is not strained to reduce the mismatch.

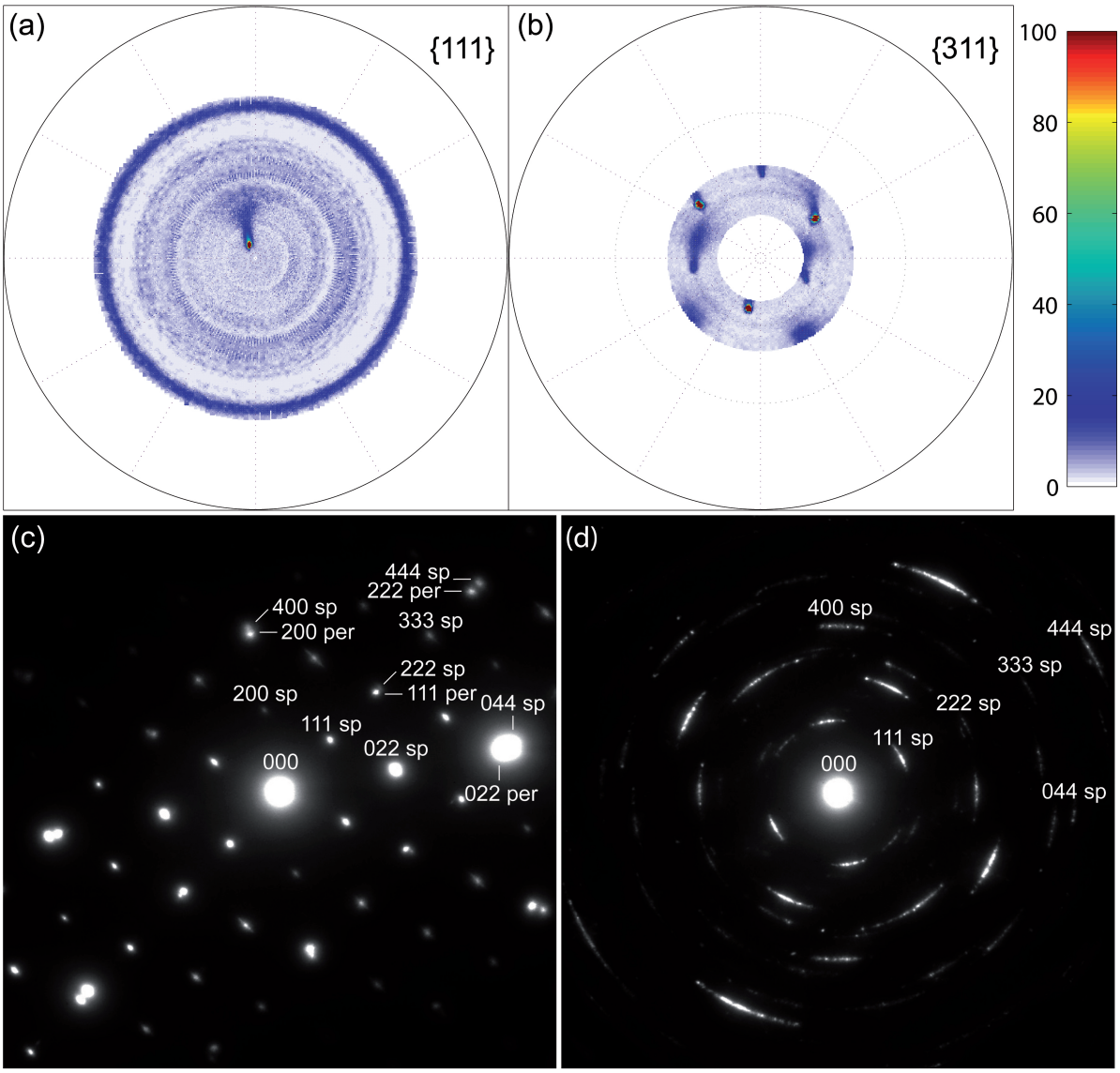

Figure 3.25: Periclase substrates three-layer setup. (a) {111} and (b) {311} pole figures (stereographic projections; normalized intensities) of sample Per17. (c) DP collected at the periclase substrate/inner spinel sublayer interface showing parallelism of low-index crystallographic directions of periclase and spinel. (d) DP collected in the outer spinel layer. Spinel diffraction spots are smeared now.

To summarize, pole figures and DPs along with EDDI spectra prove that the spinel layers grew topotaxially into the periclase substrates and the Al_2O_3 reactant layers; directions of close packing within the planes of close-packed oxygen ions are parallel. The orientation of crystallites that replaced the Al_2O_3 reactant layer may be less exact, especially when a spinel seed layer was used as the results in Figure 3.25 suggest.

3.5 Ex-situ TEM Analysis

Observations obtained from TEM micrographs regarding microstructures inside the spinel reactions bands as well as at the substrate/spinel phase boundaries are presented in the following two subsections. These observations have implications for the partial reactions at the interfaces and thus for the diffusion mechanism.

According to the cation counterdiffusion mechanism discussed in section 1.3.1, the initial interface between the substrate and the reactant layer is localized at a certain depth within the spinel reaction band. For every part spinel grown at the periclase/spinel interface, three parts are produced at the corundum/spinel interface. Thus, the reaction band can be split into a 25 % layer — the periclase-grown sublayer — and a 75 % layer — the corundum- or γ–Al_2O_3-grown sublayer.

3.5.1 Corundum Substrates

A natural, planar microstructure inside the spinel reaction bands at a depth compatible with the cation counterdiffusion mechanism was found in two long-duration experiments. This microstructure was already presented in Figures 3.7b and 3.7c for sample Cor8. The smaller, outer spinel sublayer in these micrographs grew highly uniform in thickness; this sublayer has a mean width of 92 ± 3 nm. In contrast, the thicker, inner sublayer has a wavy interface morphology towards the substrate, exhibiting outstanding thickness variations across the foil. This sublayer has a mean width of 302 ± 30 nm. The sublayer thickness ratio is therefore about 1:3, suggesting that a 25 % and a 75 % layer was formed by consumption of the periclase thin film and the corundum substrate, respectively.

A similar scenario was found for sample Cor9. This sample is presented in Figures 3.26a and 3.26b. The planar microstructure is not as clearly discernible as in the previous specimen, but the initial interface can nevertheless satisfactorily be traced, especially in Figure 3.26b. Different grain sizes may cause the change in contrast across the sublayers. Relatively large crystallites seem to be present in the inner sublayer as large areas with the same bright color suggest. On the other hand, the outer sublayer is overall darker and smaller crystallites seem to prevail. Grain sizes of 40 nm were estimated using the Scherrer equation; this may be more valid for the outer sublayer. Individual sublayer thickness measurements yielded widths of 76 ± 8 and 193 ± 27 nm which is near a 1:3 ratio. Similar to Cor8, this reaction rim grew highly non-uniform in thickness, i.e. some portions of the inner sublayer proceed further into the substrate than others.

Another feature visible in many TEM BF micrographs are bend contours. They were frequently observed when a reaction took place at temperatures $\geq 900\,^{\circ}$C, i.e. they are absent in micrographs obtained from the low temperature experiments presented in Figure 3.5; they were also never present when periclase was used as substrate. These bend contours were presented in several micrographs before in the sections on the *in-situ* monitoring of spinel layer growth (Figs. 3.6c, 3.6d, 3.8b, 3.11b and 3.11d); however,

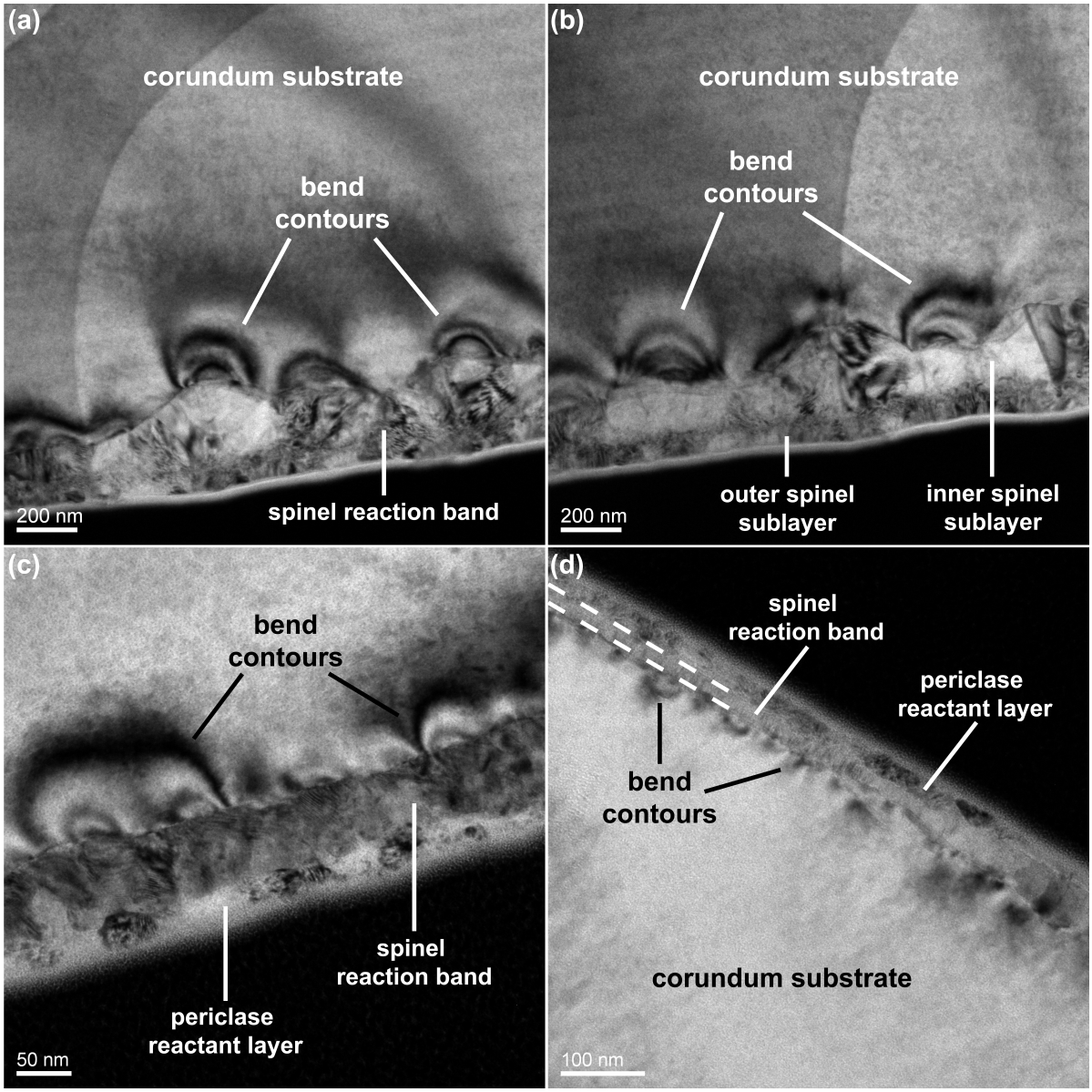

Figure 3.26: Bend contours in TEM BF micrographs. (a, b) Sample Cor9 (T = 1000 °C; t = 120 min). Individual bend contours extend 200 nm and more into the substrate. Two sublayers are discernible in the reaction band. Note that the holey carbon support film causes additional bowed contrasts across the substrate. (c) Sample Cor29 (T = 1000 °C; t = 31 min). Some bend contours seem to coalesce at the phase boundary. (d) Sample Cor27 annealed for only 5 minutes at 1000 °C exhibits rather blurred bend contours. The extent of the spinel reaction band is marked by dashed lines. Note scale bars in the lower left corners of the images.

they are more pronounced in the images presented in Figure 3.26. When present, they always emerge at the corundum/spinel phase boundary. They extend 10 to more than 100 nm into the corundum substrates, scaling to some degree with the thickness of the respective reaction band. In samples that were annealed at only 900 °C (Cor26 presented in Figs. 3.6c and 3.6d and Cor18 presented in Fig. 3.11b) or for a short run duration of only 5 minutes at 1000 °C (Cor27 presented in Fig. 3.26d), i.e. in experiments in which spinel growth or the expansion of the seed layer was restricted to less than 20 nm, the contours are rather blurred and less developed. On the other hand, well developed such as in Figures 3.26a, 3.26b and 3.26c, samples in which the spinel reaction band thickness exceeds 100 nm, they appear as alternating bright and dark curved lines. Still emerging at the phase boundary, these contrasts move across the foil when the sample is tilted in the microscope. Often, such as in Figure 3.26c, individual contours seem to coalesce at the corundum/spinel phase boundary.

An interpretation and explanation for the origin of these bend contours is given in chapter 'Discussion' in section 4.1.3.1 on the volume changes at the corundum substrate/spinel interface.

3.5.2 Periclase Substrates

A change in microstructure inside the spinel reaction bands that points to the cation counterdiffusion mechanism is also visible in TEM micrographs obtained from periclase substrate samples. This microstructure and two spinel sublayers were already presented in the HAADF micrograph in Figure 3.18; two additional BF images are presented in Figure 3.27. Due to different shades of grey, probably caused from different grain structures, two spinel sublayers can be distinguished in these images (EDX measurements proved that these two sublayers are indeed spinel). In both cases, a thin, inner sublayer is situated between a thin porous layer towards the periclase substrate and a thicker, outer sublayer towards the top of the sample. The boundaries between the spinel sublayers are marked by dashed lines in Figure 3.27.

In the HAADF micrograph in Figure 3.18, the inner sublayer is homogeneous bright whereas in the outer sublayer, dark patches are visible. Conversely, in the TEM BF micrographs of Figure 3.27, the inner spinel sublayers are altogether darker than the outer sublayers in which bright patches are visible. Both observations in these two different TEM modes point to the existence of less dense areas in the outer sublayers, i.e. these areas are darker than the surroundings in HAADF images but brighter in TEM BF images.

As the γ–Al_2O_3 layer exhibits many dark patches in HAADF micrographs when not all of the reactant layer was consumed (cf. Figs. 3.15 and 3.20), the porosity of the outer spinel sublayer is probably inherited from the nanocrystalline γ–Al_2O_3 that was transformed to spinel during the experiment. Due to its nanocrystallinity, grain boundaries are abundant in this material, and this is most likely the reason why it is less dense. Consequentially, the inner sublayer was transformed from the periclase single crystal

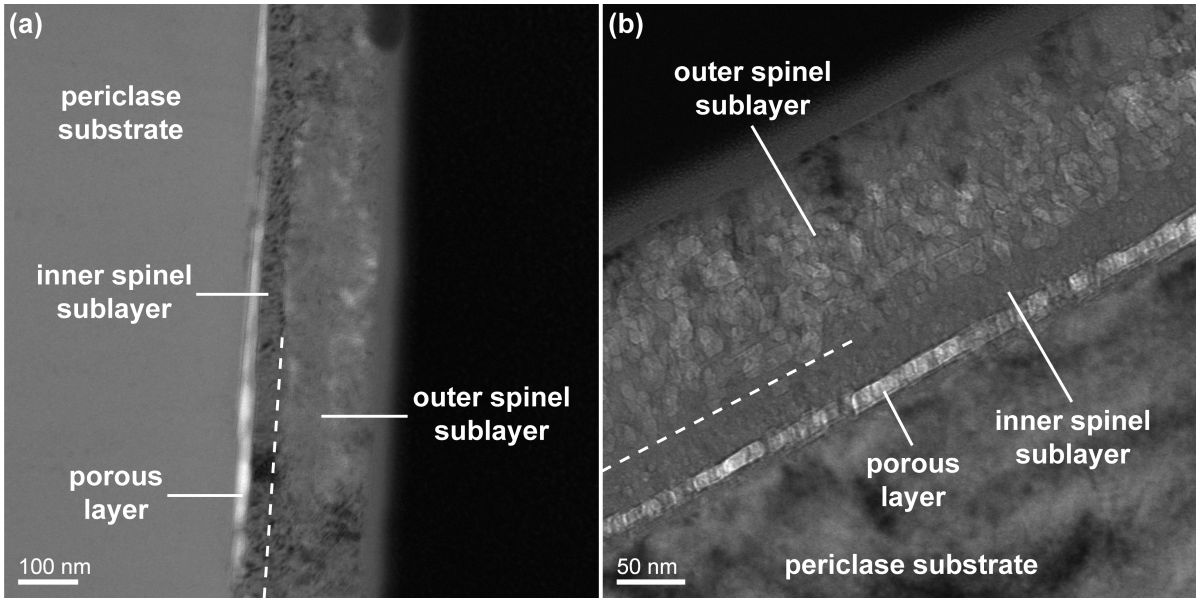

Figure 3.27: TEM BF micrographs to highlight a change in microstructure inside the reaction band; dashed lines mark the boundary between the spinel sublayers. A porous or less dense layer at the periclase/spinel phase boundary was always observed when spinel was formed. (a) Sample Per26 ($T = 1000\,°C$; $t = 60\,min$). A HAADF micrograph of this sample is presented in Figure 3.28. (b) Sample Per28 ($T = 1000\,°C$; $t = 30\,min$). Note scale bars in the lower left corners of the micrographs.

(no grain boundaries) to spinel in each case, and this is the reason why this sublayer is denser. The dissimilar grain structures are also visible in the HAADF micrograph presented in Figure 3.28. The inner spinel sublayer is homogeneous in color and appears almost monocrystalline whereas the outer sublayer exhibits a grainy structure which was most likely inherited from the nanocrystalline γ–Al_2O_3.

The expected thickness ratio of 1:3 between the two sublayers is better achieved for sample Per26 presented in Figures 3.27a and 3.28 when the porous layer between the substrate and the inner spinel sublayer is excluded from the thickness measurements for the inner sublayer. This is supported from inspections of HAADF micrographs such as in Figure 3.28 in which it can be seen that the adherence of the spinel layer to the substrate is poor. Large lateral voids have formed at the interface, and this porous layer is now rather a gap between substrate and thin film. Without this layer or gap, the inner sublayer of this sample has a mean thickness of $46 \pm 2\,nm$ whereas the outer sublayer was measured as $151 \pm 3\,nm$ thick.

On the other hand, for sample Per28 presented in Figure 3.27b, the 1:3 ratio is better achieved when the porous layer is included for the thickness measurements of the inner spinel sublayer. This approach is also supported from observations in HAADF and high-resolution TEM micrographs in which pores can be seen but not a distinctive gap,

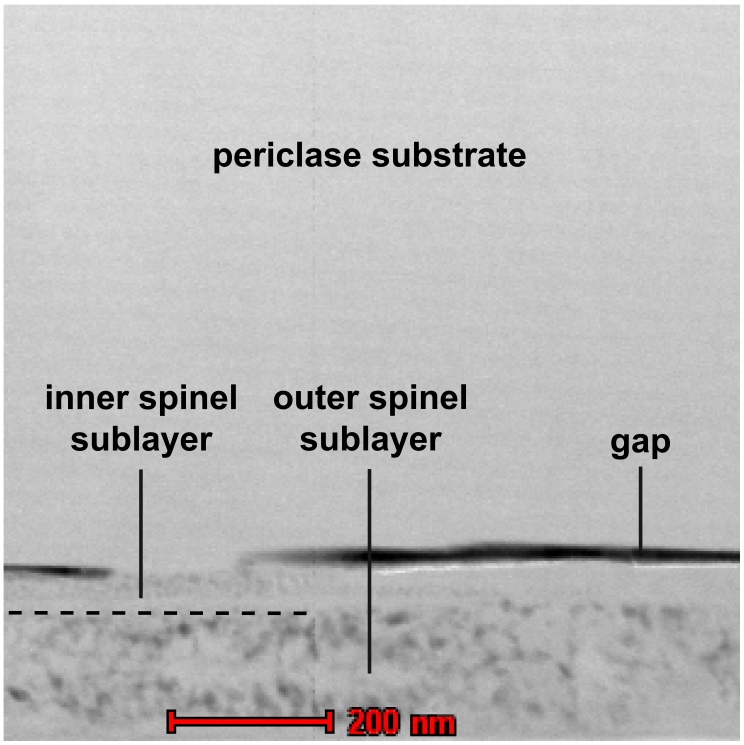

Figure 3.28:
HAADF micrograph of sample Per26. An almost continuous gap between periclase substrate and inner spinel sublayer has formed after 1 hour of annealing at 1000 °C. The dashed line marks the boundary between the spinel sublayers. The inner sublayer appears to be monocrystalline whereas the outer sublayer exhibits a grainy structure. A TEM BF image of this sample was presented in Figure 3.27a. Note scale bar at the bottom of the image.

i.e. the adherence of the thin film to the substrate is better than in the former sample. Thicknesses of 48 ± 2 and 133 ± 2 nm for the inner and outer sublayers were obtained, respectively. Without the porous layer, a thickness of 33 ± 1 nm was measured which results in a 1:4 ratio between the sublayers.

In the periclase three-layer setup, the spinel seed layer is situated between the two sublayers inside the reaction band as it was demonstrated by TEM analysis (Fig. 3.20b). The thicknesses of the inner and the outer sublayer were determined as 133 ± 5 and 424 ± 15 nm, respectively. The position of the seed layer inside the reaction band and the approximate 1:3 ratio between the sublayers are in very good agreement with the scenario expected from the cation counterdiffusion mechanism.

Bend contours, as they were frequently observed at the corundum substrate/spinel interface, were never present at the periclase substrate/spinel interface; instead, the porous layer always formed at the phase boundary. This layer was labeled as porous in all TEM images that were presented so far. In addition, the pores may collect into larger voids until finally a gap has formed at the interface. For example, in sample Per24, annealed for only 5 minutes at 1000 °C, a continuous gap has not yet formed, but voids or pores are present between the inner spinel sublayer and the substrate as it can be seen in the HAADF micrograph in Figure 3.18. A similar contact was found after 30 minutes (sample Per26 presented in Fig. 3.27b); however, the adherence is very poor after 60 minutes of annealing where an almost continuous gap is present (cf. Fig. 3.28). This may lead to the conclusion that a gap is gradually formed out of the pores and voids

upon heating at 1000 °C. The longer the run duration the poorer will be the adherence between thin film and substrate.

Some of the pores and voids directly at the interface may be even retained in the inner spinel layer when the growth front advances into the substrate; this remnant porosity in the inner spinel sublayer was observed in the sample presented in Figure 3.20b.

Another observation dissimilar to the corundum substrate samples is that the growth front always proceeded highly uniform into the substrate, i.e. the spinel layer thickness does not vary much across the foil.

The origin of the porous layer is discussed in section 4.1.3.2 on the volume changes at the periclase substrate/spinel interface.

3.6 Ex-situ Analysis of the One-Layer Setups

Some specimens were used to study the crystallization of initially amorphous $MgAl_2O_4$ layers to spinel on top of the two different substrates. The intensity of spinel Bragg reflections in GIXRD measurements was always low, even when 100 s/step was used as the counting rate. This is due to (i) spinel is composed of only light elements ($Z_O = 8$; $Z_{Mg} = 12$; $Z_{Al} = 13$); (ii) the scanned layers were not thicker than 200 nm; (iii) the material crystallized epitaxially aligned on the substrates as it was presented in previous sections.

3.6.1 Corundum Substrates

A GIXRD scan of a 180 nm thick spinel thin film that was annealed for 5 minutes at 1000 °C is presented in Figure 3.29a (this is the layer that was presented in Figure 2.11 on page 37 in side view). The GIXRD scan proves that the initially amorphous $MgAl_2O_4$ layer crystallized to spinel; all spinel Bragg reflections with their approximate relative peak intensities I_{hkl}/I_{311} are visible whereas no distinct reflections of the substrate or other phases are present. With respect to the lattice constant of spinel at room temperature ($a_0 = 8.084$ Å; Redfern et al., 1999), the peaks exhibit shifts towards higher 2θ values, i.e. smaller lattice plane distances. A Le Bail refinement (Le Bail et al., 1988; Le Bail, 2005) of the diffractogram presented in Figure 3.29a provided a lattice constant of $a = 8.005 \pm 0.002$ Å. The grain structure of the sample in plan view is presented in Figure 3.29b. The AFM measurement suggests that the surface roughness is in the nm range.

Because the scattering vector $\vec{s}_{hkl}$ of a Bragg reflection is not parallel to the substrate normal s_3 in the GIXRD configuration (cf. Fig. 2.12 on page 39), no conclusions regarding the texture of the sample can be drawn out of the measurement. However, another specimen with a 160 nm thick spinel layer on top was scanned at room temperature at the EDDI beamline. This specimen was annealed for 2 hours at 1000 °C. The spectrum is presented in Figure 3.29c; it exhibits prominent *hhh*-type spinel Bragg reflections besides

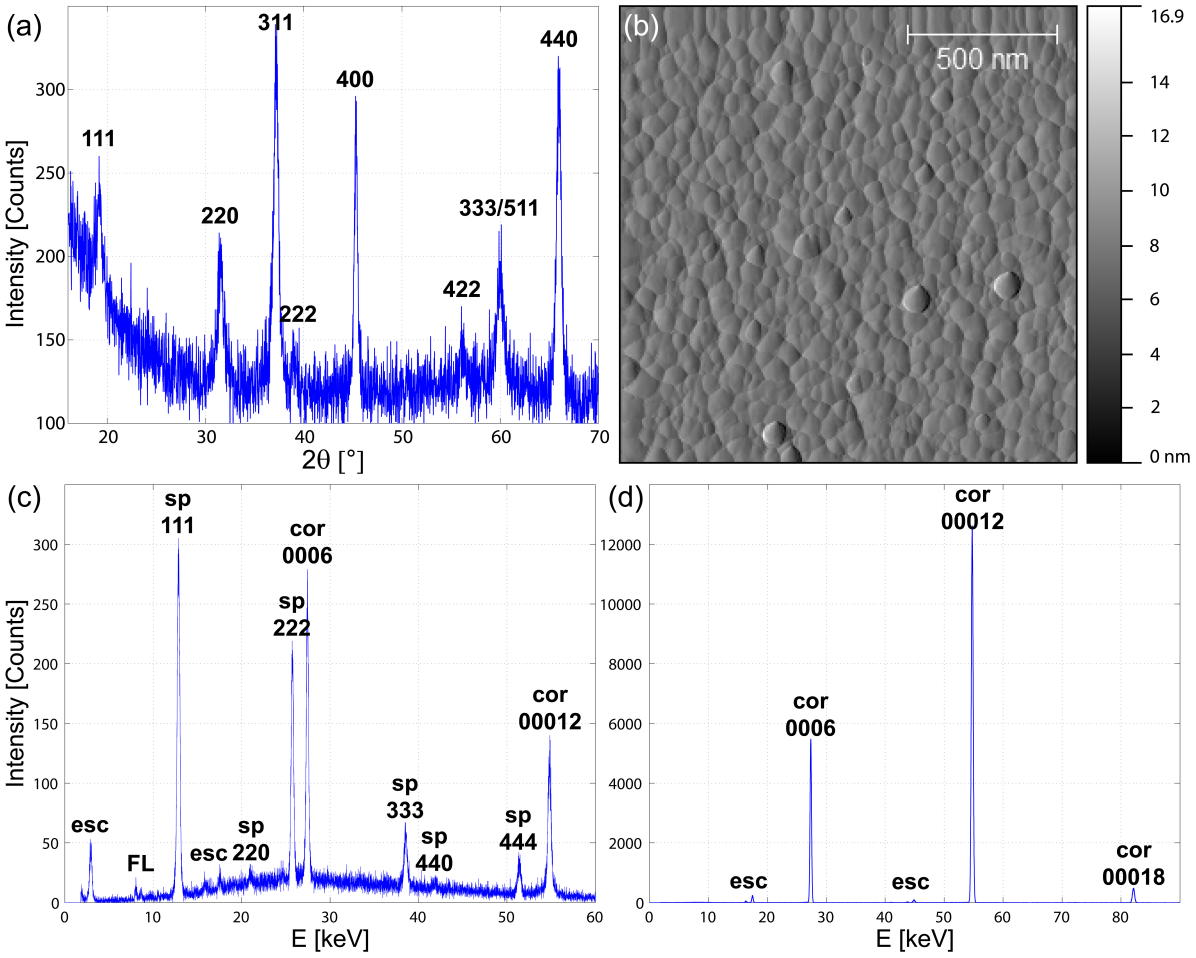

Figure 3.29: Corundum substrates one-layer setup: ex-situ analyses. (a) GIXRD scan of a 180 nm thick spinel layer. The initially amorphous layer was annealed for only 5 minutes at 1000 °C. The measurement was performed using CuKα radiation with an incident angle of $\alpha = 1.5°$, a step size of 0.02° and a counting rate of 100 s/step. (b) AFM measurement showing the grain structure in plan view. Note scale bars. (c) EDDI spectrum of a 160 nm thick spinel layer that was annealed for 2 hours at 1000 °C. Besides *hhh*-type spinel Bragg reflections, minor *hh0*-type signals are present. (d) Measurement of the sample after determining the miscut of the sample, i.e. the value of ω for which the intensity of the corundum reflections were highest. In this position, no reflections of the spinel thin film are discernible. For both spectra T = 25 °C and Δt = 60 s.

minor *hh0*-type signals. This illustrates that the out-of-plane orientation of most crystals is {111}. From the position of the 111 spinel reflection at 12.847 ± 0.002 keV, a lattice plane distance of 4.6164 ± 0.0008 Å is derived. This corresponds to a lattice constant of $a = 7.996 \pm 0.002$ Å. The Le Bail refinement of an additional GIXRD measurement of

this sample provided a lattice constant of $a = 7.998 \pm 0.006$ Å in very good agreement with the EDDI results.

The spinel reflections in Figure 3.29c are relatively prominent compared to the corundum substrate reflections. This was achieved by moving the sample via ω out of the position in which the intensity of the substrate reflection was highest. In the latter position, the reflections of the substrate are prominent, but no signals of the spinel thin film are discernible (Fig. 3.29d). This illustrates that the value of ω is crucial for the detection of the thin films and why no reflections were detected in some experiments.

3.6.2 Periclase Substrates

A GIXRD scan of a 160 nm thick spinel thin film that was annealed for 2 hours at 1000 °C is presented in Figure 3.30a. The diffractogram proves that the initially amorphous $MgAl_2O_4$ layer crystallized to spinel. The overall intensity is low, but most of the possible spinel Bragg reflections in this 2θ range are well discernible. A Le Bail refinement provided a lattice constant of $a = 8.047 \pm 0.004$ Å.

The grain structure of the film in plan view is presented in Figure 3.30b. Many triangular grains are observable in this SEM image. These grains are bright in color, share the same approximate grain size (diameters of 160 to 180 nm) and are aligned in the same way, suggesting epitaxial crystallization of the material. The triangular shape is typical for octahedral faces, i.e. {111}-oriented crystallites. Some areas with smaller grain sizes can be seen; the grain size distribution may be thus described as bimodal.

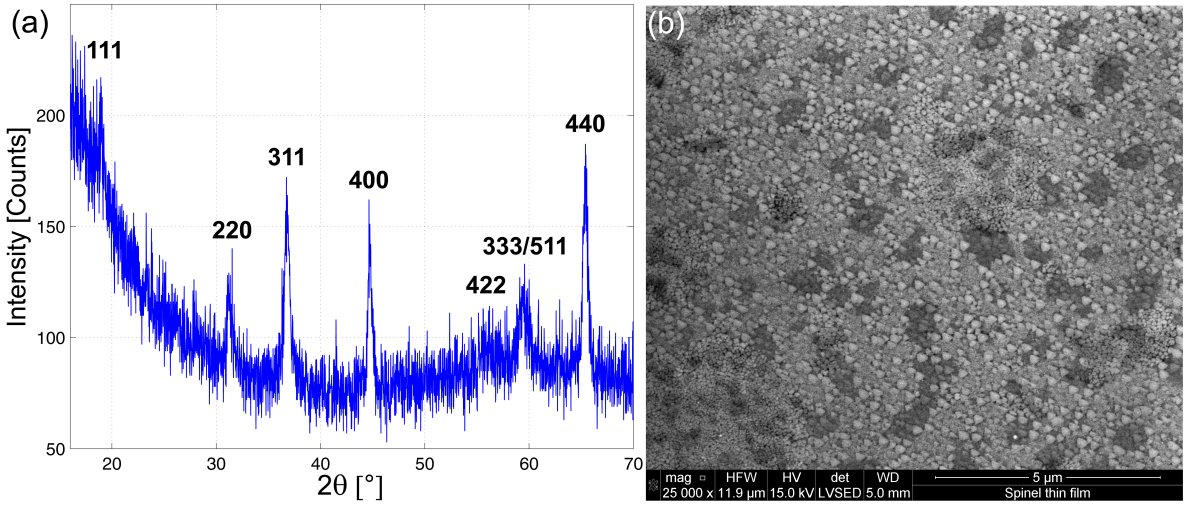

Figure 3.30: Periclase substrates one-layer setup. (a) GIXRD scan of a 160 nm thick spinel layer. The measurement was performed using CuKα radiation with an incident angle of $\alpha = 1.5°$, a step size of 0.02° and a counting rate of 100 s/step. (b) SEM image showing the grain structure of a spinel thin film in plan view. Note scale bar in the lower right corner of the image.

4 Discussion

4.1 Diffusion Mechanism

The proposed diffusion mechansim — the counterdiffusion of the cations through a relatively rigid oxygen sublattice — was presented and explained in section 1.3.1; to illustrate the initial and transient configuration of phases and spinel sublayers in this diffusion reaction couple, a schematic was given in Figure 1.3. At least three characteristics of the reaction bands presented in this thesis point to this diffusion mechanism:

1. The approximate spinel sublayer ratios of 1:3
2. The topotaxial growth of spinel into the substrates and the reactant layers indicates that the oxygen sublattice is rather rigid, i.e. it may remain unchanged upon transformation from the reactants to spinel[1]
3. Volume changes at the substrate/spinel interfaces that follow from the reaction stoichiometry of the cation counterdiffusion mechanism are indicated by bend contours using corundum substrates or a less dense layer using periclase substrates

These objects will be discussed in the following subsections.

4.1.1 Spinel Sublayers

Using corundum as well as periclase substrates, the initial interface between the reactants inside the spinel reaction bands could be identified either way in TEM BF as well as HAADF micrographs without using inert markers.

Using corundum substrates, the initial interface is indicated by a natural, planar microstructure that divides the reaction band into a thin outer sublayer and a thick inner sublayer with relative thickness proportions of about 1:3 as it was presented in section 3.5.1 on the ex-situ TEM analysis of these samples. It has to be noted that this planar microstructure was found only in two long-duration experiments in which the MgO reactant layer was consumed during the experiment; micrographs of these experiments were presented in Figures 3.7b, 3.7c, 3.26a and 3.26b. The outer sublayer was formed by consumption of the nanoscale MgO reactant layer and the inner sublayer

[1]However, the oxygen stacking has to be reconstructed from the hcp stacking of corundum to the fcc stacking of spinel and oxygen-oxygen distances of two adjacent phases are different.

by topotaxial growth of the reaction band into the substrate. Although these sublayers could not be identified in TEM micrographs of all other samples, it is suggested that the cation counterdiffusion mechanism operated in these experiments as well.

Using periclase substrates, a change in microstructure is also visible in TEM micrographs. This change was presented in section 3.5.2 on the ex-situ TEM analysis of these samples. In this setup, the thin, inner sublayer was formed by the topotaxial growth of spinel into the periclase single crystal and the thick, outer sublayer by consumption of the Al_2O_3 reactant layer. The TEM analysis of sample Per17 demonstrated that in the three-layer setup the seed layer is situated between a thin, inner and a thick, outer sublayer with thickness proportions of 1:3.

A microstructural and/or textural discontinuity inside spinel reaction bands was observed in several studies before as it was reviewed in the introduction in sections 1.3.2 and 1.3.3 on experimental spinel growth. At the nanoscale, inert markers were used to locate the initial interface in this system (Hesse et al., 1994, who used a $(1\bar{1}02)$-oriented corundum substrate; Sieber et al., 1996, who used (001)-oriented periclase as well as $(1\bar{1}02)$-oriented corundum substrates). As inert markers can nevertheless move in an experiment, natural markers such as grain structures or porosity may be more reliable and should be used whenever possible (Pettit et al., 1966). For example, Kotula et al. (1998) found their $NiAl_2O_4$ spinel seed layer inside reaction bands due to a general change in grain structure between the sublayers and due to different positions of stacking faults that formed during film growth.

4.1.2 Topotaxial Growth of Spinel Layers

Oriented crystallization of thin films on single crystal substrates is observed frequently. A single three-dimensionally constrained relationship between the orientation of a crystallite and the substrate for which the interface energy is minimized should always exist (Thompson, 1990).

4.1.2.1 Spinel Rotation Twins

Using corundum as well as periclase substrates, EDDI spectra and the pole figures demonstrated that the out-of-plane orientation of most spinel crystallites in the reaction bands is {111}. Additionally, {311} pole figures indicated that a distinct in-plane orientation exists. Due to the intrinsic threefold symmetry of the cubic crystal structure about {111}, three poles at $\alpha = 29.5^\circ$ and regular distances of $\beta = 120^\circ$ are expected in {311} pole figures when all the crystallites are epitaxial or topotaxial aligned. The occurrence of six poles at distances of $\beta = 60^\circ$ in the pole figures indicates that twinning around a <111> axis is present, i.e. two types of orientation variants exist. These variants are related by a 60° or equivalently 180° rotation about the <111> axis. This twin law is known as the spinel twin law; it is characterized by {111} twins in fcc minerals such as magnetite, diamond, galena and copper (Daneu et al., 2007). As both types of grains

are related by a pure rotation around the substrate normal, these twins are also termed rotation twins (Grundmann, 2011).

Following Grundmann (2011), trigonal substrates such as (0001)-oriented corundum as well as cubic (111)-oriented substrates such as periclase belong to the symmetry group $G_S = 3m$ with respect to the two-dimensional point symmetries of their semi-infinite half spaces. The expected number of rotational domains (RDs) for epilayers which belong to the symmetry group $G_E = 3m$ (such as (111)-oriented spinel crystallites) on substrates with $3m$ symmetry is only $N_{RD} = 1$, i.e. single domain growth is expected. However, two rotation variants are observed frequently in these systems, yielding $N_{RD} = 2$; some examples are presented in Table 4.1, more examples as well as a comprehensive overview of general epitaxial relationships can be found in Grundmann (2011).

There are at least two reasons why $N_{RD} = 2$ is frequently observed. Firstly, the topmost layer of the hcp oxygen sublattice of (0001)-oriented corundum as well as the topmost layer of (111)-oriented periclase offer a $6mm$ two-dimensional point symmetry, respectively, whereas the first two layers and the semi-infinite half space each have $3m$ point symmetries, respectively. Thus, if the arrangement of the spinel lattice is deter-

Table 4.1: Crystallographic orientation relationships between $3m$ materials. Lines in the table separate hexagonal/cubic (top), trigonal/cubic (middle) and cubic/cubic (bottom) substrate/epilayer systems. An in-plane twinning of the epilayers was found in all cited studies. In hcp structures the close-packed directions lie along $<11\bar{2}0>$ whereas in trigonal corundum they lie along $<10\bar{1}0>$ (e.g. Lee and Lagerlof, 1985). The close-packed directions for cubic minerals which have a fcc unit cell lie along the diagonals <110>.

Substrate/Epilayer	Out-of-plane	In-plane	Reference
2H-SiC/Diamond	(0001) || (111)	$<11\bar{2}0> \,\|\|\, <110>$	Suzuki et al., 1994
4H-SiC/γ–Al_2O_3	(0001) || (111)	$<11\bar{2}0> \,\|\|\, <110>$	Tanner et al., 2007
Graphite/Diamond	(0001) || (111)	$<11\bar{2}0> \,\|\|\, <110>$	Li et al., 1993
ZnO/MgO	(0001) || (111)	$<11\bar{2}0> \,\|\|\, <110>$	Saitoh et al., 2002
α–Al_2O_3/γ–Al_2O_3	(0001) || (111)	not specified	Simpson et al., 1998
α–Al_2O_3/Cu	(0001) || (111)	$<1\bar{1}00> \,\|\|\, <110>$	Knoll and Bialas, 1994
α–Al_2O_3/NiO	(0001) || (111)	$<1\bar{1}00> \,\|\|\, <110>$	Kotula and Carter, 1995
α–Al_2O_3/Pt	(0001) || (111)	$<1\bar{1}00> \,\|\|\, <110>$	Blanton and Hung, 1996
α–Al_2O_3/$MgAl_2O_4$	(0001) || (111)	$<1\bar{1}00> \,\|\|\, <110>$	(section 4.1.2.2)
α–Al_2O_3/MgO	(0001) || (111)	$<1\bar{1}00> \,\|\|\, <110>$	(section 4.1.2.2)
Si/γ–Al_2O_3	(111) || (111)	$<110> \,\|\|\, <110>$	Wu et al., 2005
Si/Al	(111) || (111)	$<110> \,\|\|\, <110>$	Choi et al., 1987
Si/Ag	(111) || (111)	$<110> \,\|\|\, <110>$	Nason et al., 1991
MgO/$MgAl_2O_4$	(111) || (111)	$<110> \,\|\|\, <110>$	(section 4.1.2.3)

mined solely by interaction with the top oxygen layer, it senses a sixfold symmetry and two rotation variants will be observable (Grundmann, 2011). This scenario was also suggested by Gupta and Yakuphanoglu (2011) for epitaxial growth of $MgFe_2O_4$ spinel on (0001)-oriented corundum; it is schematically depicted in Figure 4.1a. Secondly, due to the miscut of both substrates (cf. sections 2.1.1 and 2.1.2), terraces at the reaction surfaces are present. Some of these terraces will offer a $3m$ symmetry but 180° rotated with respect to the topmost layer, thus giving rise to two rotation variants; this scenario is schematically depicted in Figure 4.1b.

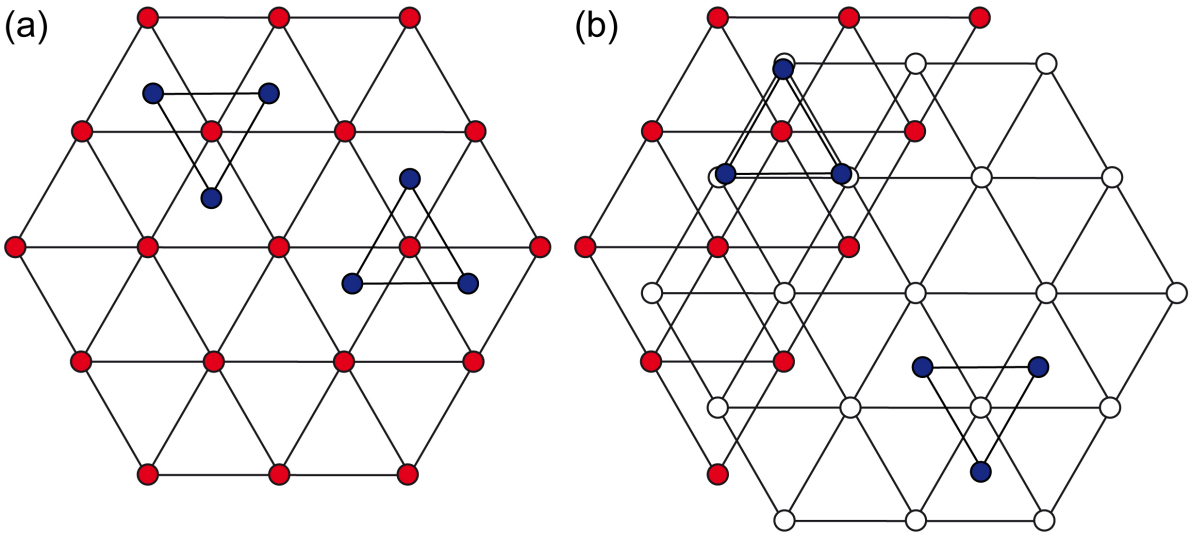

Figure 4.1: On the occurrence of spinel rotation twins (see text for explanation). Red spheres: topmost oxygen layer; white spheres: second layer; blue spheres: crystallites of the epilayer. (a) Two inequivalent domains that are related by a 180° rotation. (b) Two equivalent domains on different terraces of the substrate. After Gupta and Yakuphanoglu (2011) and Grundmann (2011). Image modified from Grundmann (2011).

4.1.2.2 Corundum Substrates

It is suggested that in the *in-situ* experiments first the MgO films crystallized epitaxially onto the corundum substrates before the spinel-forming reaction started at temperatures $\geq 900\,^{\circ}C$. In some experiments carried out at the EDDI beamline, the 111 periclase Bragg reflection appeared at temperatures between 700 and 800 °C. At these low temperatures, no spinel growth occurred, allowing heteroepitaxial crystallization of periclase onto corundum. The epitaxy of MgO films on c-plane corundum was studied several times before. For example, Li et al. (1992) reported two variants for the in-plane orientation of the periclase crystallites in line with typical findings for trigonal/cubic systems (cf. Table 4.1):

Out-of-plane: (0001) corundum || (111) periclase

In-plane variant A: $[10\bar{1}0]$ corundum || $[1\bar{1}0]$ periclase

In-plane variant B: $[10\bar{1}0]$ corundum || $[\bar{1}10]$ periclase

These two variants are in twin orientation with respect to each other and a $\Sigma 3$ boundary is formed where they meet (Pirouz and Yang, 1990; cited in Li et al., 1992). Similarly, Stampe et al. (1999) found that periclase films crystallize (111)-oriented on top of (0001)-oriented corundum single crystals. Six poles are present in {100} pole figures, indicating that at least two sets of crystallites are present, and all seem to occur with equal probability. An in-plane twinning and the parallelism of close-packed oxygen planes and directions in the corundum/periclase system was also found by e.g. Saitoh et al. (2002) and Martínez-Boubeta et al. (2012).

The spinel crystallites of the reaction bands grew topotaxially in both directions, replacing the lattices of the corundum substrates and the periclase reactant layers. The out-of-plane relation (0001) corundum || (111) spinel was found in EDDI spectra and in {111} pole figures, an in-plane twinning in {311} pole figures and the parallelism of certain crystallographic directions in DPs. Along with the periclase layer on top, these setups crystallized and grew as an epitaxial stack such that the planes of close-packed oxygen ions and the directions of close packing within these planes lie parallel:

Out-of-plane: (0001) corundum || (111) spinel || (111) periclase

In-plane: $<10\bar{1}0>$ corundum || $<110>$ spinel || $<110>$ periclase

The same crystallographic orientation relationship between c-plane corundum and spinel *sensu stricto* was reported several times before (e.g. Rossi and Fulrath, 1963; Boese, 2004; Liu et al., 2005; Keller et al., 2010). The same relations were also found for e.g. the growth of $NiAl_2O_4$ between c-plane corundum and thin films of NiO (Kotula and Carter, 1995; Kotula et al., 1998). Hesse et al. (1994) reported a similar epitaxial stack between *r*-plane corundum and periclase, illustrating that other orientations of the substrate ensure topotaxial growth as well:

Out-of-plane: $(1\bar{1}02)$ corundum || (001) spinel || (001) periclase

In-plane: $[11\bar{2}0]$ corundum || [010] spinel || [010] periclase

Instead of sharp spots, triangular shapes appear in {311} pole figures when the MgO reactant layer was consumed. This indicates that the crystallites slightly rotate out of the exact epitaxial alignment upon further annealing. Grains are now slightly tilted and/or twisted against each other.

4.1.2.3 Periclase Substrates

In these setups, it is suggested that first the amorphous Al_2O_3 crystallized to an epitaxial γ–Al_2O_3 layer in a way typical for cubic/cubic systems (cf. Table 4.1). The emergence of the 222 γ–Al_2O_3 Bragg reflection at temperatures between about 600 and 800 °C was observable at the EDDI beamline, indicating that the film had a {111} texture. It is also suggested that two orientation variants exist as an in-plane twinning in {111}-oriented γ–Al_2O_3 thin films is observed frequently. For example, Wu et al. (2005) demonstrated that γ–Al_2O_3 thin films crystallize epitaxially on (111)-oriented silicon substrates. Simpson et al. (1998) used (0001)-oriented corundum substrates and demonstrated that an amorphous Al_2O_3 layer crystallizes first to (111)-oriented γ–Al_2O_3. Six poles are present in {220} pole figures, indicating that two in-plane variants exist. The amorphous-to-γ–Al_2O_3 phase transformation started at a temperature of 760 °C. The γ–Al_2O_3 was transformed to α–Al_2O_3 at 950 °C with a very slow growth rate of 0.003 nm/s. This latter phase transformation was not observed at the EDDI beamline.

Similar to the setups using corundum substrates, the spinel crystals of the reaction bands grew topotaxially in both directions, replacing the lattices of the periclase substrates and the γ–Al_2O_3 reactant layers. The out-of-plane relation (111) periclase || (111) spinel was found in EDDI spectra and in {111} pole figures, an in-plane twinning in {311} pole figures and the parallelism of certain crystallographic directions in DPs. Along with the γ–Al_2O_3 layer on top, these setups crystallized and grew as an epitaxial stack such that the planes of close-packed oxygen ions and the directions of close packing within these planes lie parallel:

Out-of-plane: (111) periclase || (111) spinel || (111) γ–Al_2O_3

In-plane: <110> periclase || <110> spinel || <110> γ–Al_2O_3

It has to be noted that the texture may generally be weaker in the part that replaced the γ–Al_2O_3 layer, i.e. the outer spinel sublayer, especially when a seed layer was present as the DPs in Figure 3.25 illustrate. The epitaxial alignment between substrate and thin film is very good at their phase boundary whereas diffraction spots are smeared in the outer sublayer. Similar results were found by Comer et al. (1966). They studied the reaction between (001)-oriented periclase substrates and γ–Al_2O_3 thin films. They found a monocrystalline and a polycrystalline spinel layer in DPs and suggested that the monocrystalline layer was formed by consumption of the substrate whereas the polycrystalline layer was formed by consumption of the γ–Al_2O_3. Using TEM plan-view images, also Sieber et al. (1996, 1997) found that these grains at the top exhibit a rather large orientation variation. Sieber et al. (1997) studied the reaction between (001)-oriented periclase substrates and various oxides; a general cube-to-cube topotaxial relation was found, illustrating that other periclase orientations and other spinels ensure topotaxial growth as well.

4.1.3 Volume Changes at the Interfaces

Volume changes at the substrate/spinel interfaces that follow from the reaction stoichiometry of the cation counterdiffusion mechanism are displayed at the phase boundaries by either bend contours using corundum substrates or porosity using periclase substrates as it was presented in sections 3.5.1 and 3.5.2 on the *ex-situ* TEM analysis of the run products. Despite many studies were conducted in this system, the focus was never — to the knowledge of the author — on the volume changes at the interfaces, and these complementary effects were not observed in such a way before.

4.1.3.1 Corundum Substrates

Bend contours were observed frequently at the corundum substrate/spinel phase boundary in TEM BF micrographs. As these contours appeared only when a reaction took place, their existence could even be used to infer that in a three-layer setup a seed layer expanded during the experiment.

Bend contours are diffraction contrasts, and they indicate that the corundum crystal lattice is strained in the vicinity of the growing spinel layer. They appear when Bragg planes are twisted across a specimen so that different regions of the specimen are in different diffraction conditions at the same time (Fultz and Howe, 2008). The origin of this effect is presented schematically in Figure 4.2. Still extending from the corundum/spinel interface, these contours moved slightly across the foil when the sample was tilted in the microscope; this effect is characteristic for bend contours (Williams and Carter, 2009). Similar patterns may also arise as thickness fringes due to a varying foil thickness or from strain fields around defects such as misfit dislocations (Fultz and Howe, 2008). As these contours appear exclusively at the corundum/spinel phase boundary, and as they are observable only when the spinel-forming reaction took place, it is unlikely that varying

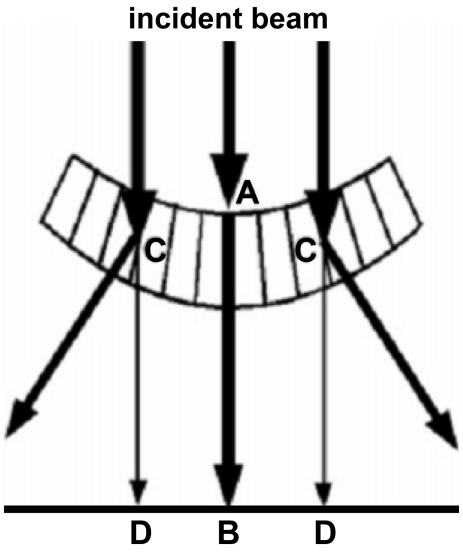

Figure 4.2: Schematic for the origin of bend contours that were observed in TEM BF micrographs at the corundum substrate/spinel phase boundary extending 10s of nm into the substrates. At point A the Bragg planes are parallel to the incident beam while at points C in the foil the Bragg condition is fullfilled; corresponding bright bands appear at point B and dark bands at points D in the image plane of the microscope (Rodriguez-Gonzalez et al., 2006). Image modified from Rodriguez-Gonzalez et al. (2006).

foil thicknesses cause this effect; thickness fringes were neither observed in TEM foils of periclase substrate samples. Misfit dislocations are expected at this interface, but it seems rather unlikely that they can deform the substrate lattice at a distance of 200 nm and more as it was shown in Figures 3.26a and 3.26b. Due to the transformation of the pseudo-hexagonal close-packed oxygen sublattice of corundum to face-centered cubic of spinel, transformation dislocations and/or interfacial ledges are required at this interface in addition to misfit dislocations (Kotula et al., 1998; Carter and Schmalzried, 1985). Transformation dislocations move to create a change in orientation or phase, and misfit dislocations accommodate the difference in lattice parameter between two well-aligned crystalline grains (Williams and Carter, 2009).

It is proposed that these contrasts arise due to the positive reaction volume of about 17 % when, according to the cation counterdiffusion mechanism and the reaction stoichiometry at this interface, 3 parts of spinel replace 4 parts of corundum at this interface. The positive reaction volume causes deformation of the corundum crystal lattice in the vicinity of the growth front. The contours are rather blurred and undeveloped when growth was restricted to less than 20 nm, but they become more pronounced the thicker the reaction band gets. The scaling of the bend contours with the thickness of the respective reaction band may indicate that stress gradually builds up at the growth front. A possible unequal distribution of stress may also lead to the observed non-uniform advancement of the corundum-grown spinel sublayer into the substrate. Without stresses a planar growth front is expected which moves with uniform thickness into the substrate (Milke et al., 2007); this uniform growth was observed for the periclase substrate samples discussed in the next subsection.

Milke and Wirth (2003) and Milke et al. (2007) observed bend contours in TEM BF micrographs obtained from similar reaction rim growth experiments. Milke and Wirth (2003) observed them at wollastonite/quartz interfaces protruding into quartz grains due to a positive reaction volume when wollastonite is formed in diffusion reaction couples between calcite and quartz according to the reaction $CaCO_3 + SiO_2 \longrightarrow CaSiO_3 + CO_2$. Milke et al. (2007) investigated growth of pyroxene layers between quartz substrates and olivine thin films according to the reaction $SiO_2 + (Mg, Fe)_2SiO_4 \longrightarrow (Mg, Fe)_2Si_2O_6$. Bend contours were observed at the quartz/pyroxene phase boundaries extending several 100 nm into the quartz substrates. A positive reaction volume at this interface was deduced, and it was demonstrated that MgO is mobile and SiO_2 rather immobile when pyroxene layers are formed. Along with the bend contours, the pyroxene layers grew also highly non-uniform in thickness. It was discussed that stresses locally add a mechanical contribution to the chemical potentials of the diffusing components.

These observations may lead to the conclusion that a positive reaction volume can be accompanied by a buildup of stress and by non-uniform growth of the reaction products with respect to their layer thicknesses. The stress can then be visualized by bend contours in TEM BF micrographs so that evidence may be provided for a proposed diffusion mechanism or even for the diffusing species.

4.1.3.2 Periclase Substrates

As soon as the spinel-forming reaction took place using periclase substrates, porosity was observed in TEM micrographs at the substrate/spinel phase boundary. This porosity was mostly concentrated in a porous layer immediately at the phase boundary, but it was demonstrated that pores are also retained in the remaining parts of the inner spinel sublayer which growths topotaxially into the periclase single crystal.

The pores at the interface may collect into larger voids until finally an almost continuous gap is formed. A continuous gap between the periclase crystal and μm-scale spinel layers was observed before, i.e. both spinel sublayers adhere rather strongly to the corundum crystal after the diffusion anneal (e.g. Rossi and Fulrath, 1963; Götze et al., 2010). This might be an effect of the negative volume change at the periclase/spinel interface, but pores can also be created by the Kirkendall effect. The Kirkendall effect (Kirkendall, 1942; Smigelskas and Kirkendall, 1947) refers to a non-equilibrium interdiffusion process in which the diffusion of vacancies towards the side of the faster diffusing species compensates for the unequal material flux (Fan et al., 2007). These vacancies can collect into voids, the so-called Kirkendall voids, which themselves may finally collect into a gap, separating the periclase substrate and the newly formed spinel layer. In this scenario, vacancies would diffuse towards the periclase/spinel interface to compensate for the coupled diffusion of Mg^{2+} and O^{2-} towards the corundum/spinel interface. However, the Kirkendall effect is usually not observed in the MgO–Al_2O_3 system, i.e. it is well established that spinel *sensu stricto* is formed by the counterdiffusion of the cations within a relatively rigid oxygen sublattice (Fan et al., 2006). In contrast, the formation of gahnite ($ZnAl_2O_4$) proceeds not via the counterdiffusion mechanism as it was first observed by Bengtson and Jagitsch (1947; cited in Carter, 1961). In Al_2O_3/ZnO diffusion reaction couples, a one-way transfer of Zn^{2+} and O^{2-} or even ZnO is observed which represents an extreme case of the Kirkendall effect (Fan et al., 2007b). When ZnO is the core material and Al_2O_3 is the shell material, the effect can be used to create hollow nanotubes when gahnite is formed by a solid-state reaction, i.e. ZnO diffuses outwards and Kirkendall voids coalesce into a single hollow core (e.g. Fan et al., 2006, 2007, 2007b; Yang et al., 2008).[2] In the case of spinel *sensu stricto*, only porous nanowires could be formed, and the authors contribute the different diffusion mechanisms to the rearrangement of the oxygen sublattices as periclase and spinel have a similar fcc crystal structure whereas the oxygen sublattice of gahnite has to be reconstructed from the hexagonal wurtzite crystal structure of ZnO to the cubic spinel structure (Fan et al., 2006); the semi-coherent corundum/spinel interface is involved in both cases.

Pores at a reaction front were also observed by Götze et al. (2010) in similar reaction rim growth experiments; they were observed at periclase/forsterite contacts in periclase/quartz diffusion reaction couples in which a double rim comprised of forsterite and enstatite develops between the reactants. Albeit an overall positive reaction volume is associated with the reaction periclase + enstatite $\longrightarrow$ forsterite, it was found that in

[2] A review of the Kirkendall effect in the nanoworld is given in Fan et al. (2007).

this system under dry conditions the MgO component is mobile and the SiO_2 component rather immobile (Milke et al., 2007; Milke et al., 2009; Gardés et al., 2011), indicating that these pores formed due to a material loss at this interface.

To summarize, as also two sublayers with relative thickness proportions of approximately 1:3 were observed in these samples, it is proposed that the pores are primarily formed due to the negative reaction volume of about 13 % when, according to the cation counterdiffusion mechanism and the reaction stoichiometry at the periclase/spinel interface, 1 part of spinel replaces 4 parts of periclase, but a contribution to pore and void formation due to the Kirkendall effect, i.e. a coupled diffusion of Mg^{2+} and O^{2-} towards the corundum/spinel interface, is not entirely ruled out.

4.2 Temperature-Dependent Growth Kinetics

4.2.1 Onset of Spinel Growth

The *in-situ* experiments of this study provide constraints at which temperature spinel starts to grow and subsequent growth is detectable on laboratory timescales using these materials and methods, i.e. a single crystal substrate/thin film diffusion couple setup and synchrotron X-ray diffraction. In the two-layer setups, an offset of 100 °C was observed for the start of the reaction; using corundum substrates, growth could be detected at 900 °C whereas for periclase substrates at 800 °C.

Even without using a spinel seed layer, the materials started to react immediately, no pronounced retardation of nucleation and subsequent growth occurred. In contrast, Pin et al. (2013b) found a retardation for the onset of $ZnAl_2O_4$ growth on (0001)-oriented corundum of about 13 minutes at 1000 °C. It was demonstrated that a seed layer is not necessary to avoid nucleation problems and to obtain planar geometries of the growth fronts; however, it has to be noted that the reaction bands neither grew entirely uniformly in thickness. Using corundum substrates, the growth front into the substrate developed increasingly non-planar with time; outstanding thickness variations were found in the longest experiments. On the other hand, using periclase substrates, growth into the γ–Al_2O_3 reactant layer proceeded supposedly non-uniform whereas the periclase substrate/spinel interface was always straight-lined. This irregular growth into the reactant layer was not prohibited by using seed layers. In contrast, Kotula and Carter (1995, 1996) deposited seed layers to deconvolute nucleation from growth, because their $NiAl_2O_4$ spinel nucleated at first at NiO twin boundaries when no seed layer was used, and subsequent growth was faster up those grain boundaries. Milke et al. (2007) deposited seed layers for similar reasons, i.e. to avoid nucleation problems and to ensure a planar reaction rim morphology (R. Milke, personal communication).

4.2.2 Spinel Growth Kinetics

As the peak area is proportional to the thickness of the diffracting material (e.g. Cserháti et al., 2008), the evolution of the integrated intensity of the 111 spinel Bragg reflection during an *in-situ* experiment may be correlated with the thickness evolution of the respective spinel reaction band, the final thickness of which was determined by cross-sectional TEM imaging. This is allowed because no sudden change in texture was observed at the EDDI beamline, i.e. only *hhh*-type spinel reflections were observed throughout the experiments. Additional evidence is provided by the texture measurements in which strong topotaxial orientation relationships between spinel reaction layers and the substrates were determined. Furthermore, the absorption of the X-rays for these materials and thicknesses can be neglected (cf. section 2.3.4 on the X-ray absorption within the layers). The evolution of I_{111} may thus be used to assess the growth kinetics of the spinel reaction layers and to deduce reaction regimes.

4.2.2.1 Corundum Substrates

This section is based to a large part on Götze et al. (2014); more detailed information on the model presented in the following and its governing equations can be found in Abart and Petrishcheva (2011) and — for its application to the spinel-forming reaction — in Götze et al. (2014).

Correlating the evolution of I_{111} with the thickness evolution of the respective reaction band, the experiments at 900 and 1000 °C suggest different reaction regimes. The increase of I_{111} at 900 °C was parabolic in the two-layer as well as in the three-layer setup, suggesting diffusion-controlled layer growth. On the other hand, at 1000 °C a linear increase of I_{111} was observed regularly, suggesting largely interface-controlled growth. These different trends of I_{111} were presented in Figure 3.8a for the complementary 1 hour experiments monitored at the EDDI beamline.

The mean linear growth rate at 1000 °C was determined as 0.050 nm/s. This is in good agreement with the value reported by Pin et al. (2013); for the growth of $ZnAl_2O_4$ on (0001)-oriented corundum substrates, they found a linear reaction rate of 0.048 ± 0.001 nm/s. The growth rate seems to be one order of magnitude slower for $CoAl_2O_4$ (He and Becker, 1997), and Kotula and Carter (1998) reported a rate of only 0.0001 nm/s for the growth of $NiAl_2O_4$ at 1050 °C.

Thermodynamic Model for Reaction Band Formation: The thermodynamic model for reaction band formation in planar geometry of Abart and Petrishcheva (2011) is applied to the data of the corundum substrates two-layer setup experiments to extract interface mobilities and effective diffusion coefficients. This model extends the formalism for diffusion-controlled reaction rim growth from Abart et al. (2009) and accounts for the interface reaction as well as for the long-range diffusion of the components as the potentially rate-limiting processes. Similar models describing mixed kinetics have been

developed by several authors before (e.g. Deal and Grove, 1965; Schmalzried, 1974; Farrell et al., 1975; Gösele and Tu, 1982; Dybkov, 1986).

The evolution equation which is a relationship between spinel layer thickness and time given by Abart and Petrishcheva (2011) reads:

$$t = \frac{1}{2\ (u-1)\ \tilde{D}\,\Delta G_{rim}}\,\Delta x^2 + \frac{1}{(u-1)\ \Delta G_{rim}}\left(\frac{1}{M_{cor}} + \frac{h^2}{M_{per}}\right)\Delta x \tag{4.1}$$

where

$$u = \frac{V_{sp}}{V_{cor}}\left(\frac{X^{per}_{\mathrm{Al_2O_3}} X^{cor}_{\mathrm{MgO}} - X^{cor}_{\mathrm{Al_2O_3}} X^{per}_{\mathrm{MgO}}}{X^{per}_{\mathrm{MgO}} X^{sp}_{\mathrm{Al_2O_3}} - X^{per}_{\mathrm{Al_2O_3}} X^{sp}_{\mathrm{MgO}}}\right) + 1 \tag{4.2}$$

and

$$h = -\frac{V_{per}}{V_{cor}}\,\frac{X^{sp}_{\mathrm{Al_2O_3}} X^{cor}_{\mathrm{MgO}} - X^{cor}_{\mathrm{Al_2O_3}} X^{sp}_{\mathrm{MgO}}}{X^{per}_{\mathrm{MgO}} X^{sp}_{\mathrm{Al_2O_3}} - X^{per}_{\mathrm{Al_2O_3}} X^{sp}_{\mathrm{MgO}}} \tag{4.3}$$

The kinetic parameter $\tilde{D}$ combines the effects of independent diffusion of the Al_2O_3 and MgO components.[3] The kinetic parameters M_{cor} and M_{per} are the mobilities of the corundum/spinel and the periclase/spinel interfaces, respectively; they relate the interface velocities to local thermodynamic driving forces. It has to be noted that only a fraction of the total thermodynamic driving force ΔG_r is available for interface motion in the model; the other fraction is dissipated in the course of long-range diffusion across the growing layer of spinel.

Equation 4.1 represents a mixed rate law in which the first term on the right hand side of the equation expresses the diffusion control and the second term the interface reaction control on overall layer growth. If the diffusion kinetics are fast, i.e. $\tilde{D}$ is large, the first term on the right hand side of Equation 4.1 may be neglected; then the second term dominates and a linear rate law results which is expected for reaction-controlled layer growth. In contrast, if the kinetics of the interface reactions at the corundum/spinel and the periclase/spinel interfaces are fast, i.e. M_{cor} and M_{per} are large, the second term on the right hand side of Equation 4.1 may be neglected; the first term then dominates and a parabolic rate law results which is expected for diffusion-controlled layer growth. Moreover, as the first term is quadratic in Δx and the second term is linear in Δx, the first term will become successively more dominant with increasing rim thickness. This leads to the well known result that the overall kinetics of layer growth evolves from an interface-controlled reaction regime during the early stages to a diffusion-controlled regime during later stages.

Application of the Model to Spinel Layer Growth: The *in-situ* monitoring of spinel layer growth at 900 and 1000 °C can be used to estimate some of the kinetic

[3] 'Components' denote chemical entities that suffice to describe the chemical compositions of the phases considered in the system, they may not represent the actual diffusing species (Götze et al., 2010), which are in this system Al^{3+} and Mg^{2+}.

parameters in Equation 4.1. From the linear relationship between layer thickness and time of the 1000 °C experiments, interface reaction control is inferred. The diffusion of the Al_2O_3 and MgO components was so efficient in this case that it did not have a detectable influence on the growth behavior. The corresponding evolution equation is obtained by neglecting the first term on the left hand side in Equation 4.1. It must be noted that the propagation of the periclase/spinel interface is kinematically coupled to the propagation of the corundum/spinel interface and, as a consequence, only the sum of $1/M_{cor}$ and h^2/M_{per} counts. In line with earlier findings (He and Becker, 1997; Kotula et al., 1998; Pin et al., 2013), it is suggested that the mobility of the periclase/spinel interface is high, and the overall mobility at 1000 °C largely represents the mobility of the corundum/spinel interface. This suggests that the term $1/M_{cor} + h^2/M_{per}$ in Equation 4.1 is dominated by $1/M_{cor}$. Equation 4.1 then allows for extracting the combined interface mobilities $1/M_{cor} + h^2/M_{per}$ from the experimentally observed rate of linear growth of the respective spinel layer. Inserting the problem-specific thermodynamic values and using the mean linear growth rate of the spinel layers at 1000 °C of 0.05 nm/s, the rate-limiting interface mobility is estimated at $1.3 \cdot 10^{-20}\,\mathrm{m^4/s\,J}$.

The linear part at the very beginning of the experiment at 900 °C is estimated at $1.3 \cdot 10^{-11}\,\mathrm{m/s}$; the combined interface mobility is then calculated as $3.5 \cdot 10^{-21}\,\mathrm{m^4\,/\,s\,J}$. The combined diffusion coefficient D_{sp} is determined as $2.9 \cdot 10^{-20}\,\mathrm{m^2/s}$; the corresponding effective diffusion coefficients $D_{Al_2O_3}$ and D_{MgO} are determined as $1.2 \cdot 10^{-20}$ and $3.5 \cdot 10^{-20}\,\mathrm{m^2/s}$, respectively.

Watson and Price (2002) investigated the rate of spinel growth between 1200 and 2000 °C. At these high temperatures, the spinel becomes non-stoichiometric across the layer, and this non-stoichiometry was used to determine interdiffusion coefficients for the Al/Mg exchange through the layer. Using their model, the interdiffusion coefficient at 900 °C is calculated as $9.1 \cdot 10^{-17}\,\mathrm{m^2/s}$, differing substantially from the model value. Zhang et al. (1996) investigated the rate of spinel growth between 1200 and 1600 °C. Interdiffusion coefficients were described by the Arrhenius equation. Using their equation, interdiffusion coefficients at 900 °C are determined as $2.6 \cdot 10^{-19}\,\mathrm{m^2/s}$, differing one order of magnitude from the model value.

4.2.2.2 Periclase Substrates

The thermodynamic model was not applied to the data obtained from the periclase substrate samples because (i) no thermodynamic data was found for the reaction $\gamma{-}Al_2O_3 + MgO \longrightarrow MgAl_2O_4$ in the literature; (ii) unlike using corundum substrates, it remains somewhat unclear at which point the reactant layer was exactly consumed in the two-layer setups. For instance, in the 900 °C experiment, the I_{111} rose parabolically until the end of the experiment after an initial linearly increasing part. This may indicate that the reaction was not completed, but no reactant layer was found in the subsequent TEM analysis. Additionally, despite the steady increase of I_{111}, the trends of d_{111} and especially of the *FWHM* of the peak indicate that the reactant layer was consumed

after 20 to 30 minutes; the *FWHM* remains virtually unchanged afterwards. The trend of I_{111} was then attributed to a dwindling reactant layer at the end of the experiment and to recrystallization processes inside the spinel layer, i.e. 'misoriented' areas were consumed or rotated into the {111} out-of-plane orientation. Additionally, it is possible that some relics of γ–Al_2O_3 remained inside the spinel layer as it was demonstrated that the growth front into the reactant layer proceeds highly non-uniform (cf. Fig. 3.20a). These relics were then transformed later to spinel, leading to the observed increase of I_{111} during later stages of the experiment. (iii) The model of Abart and Petrishcheva (2011) was developed for planar rim growth morphologies, but growth into the reactant layer occurred highly non-planar.

The linear growth rate at 900 °C was estimated at 6.1 nm/min, corresponding to 0.1 nm/s. The experiments at 1000 °C were all monitored at the EDDI beamline, and the reaction was completed when the first spectrum was recorded after 5 minutes. However, the mean linear growth rate of three experiments was estimated at 43.3 nm/min, corresponding to 0.72 nm/s, which then represents a minimum value.

4.2.2.3 Comparison of Growth Kinetics

The periclase substrate samples reacted earlier and growth kinetics were subsequently faster. Using corundum substrates, growth could be detected at 900 °C whereas for periclase substrates at 800 °C. At these low temperatures, spinel layers with thicknesses of 15 ± 1 and 20 ± 1 nm formed after about 1 hour, respectively, and in both cases a diffusion-controlled reaction regime was deduced from the evolution of the I_{111} during the experiment. These thicknesses correspond to only some 32 and 43 111 spinel lattice planes on top of each other in these reaction bands, respectively. At higher temperatures, an interface-controlled reaction regime was found for both substrates. The linear spinel-forming reaction rate of 0.1 nm/s was approximately twice as fast at 900 °C using periclase substrates as at 1000 °C using corundum substrates.

There are at the least three reasons why spinel growth occured earlier and was subsequently faster using periclase substrates: (i) the ΔG_r might be considerably lower for the reaction $\gamma\text{–}Al_2O_3 + MgO \longrightarrow MgAl_2O_4$ than for the reaction $\alpha\text{–}Al_2O_3 + MgO \longrightarrow MgAl_2O_4$ (no thermodynamic data for the former reaction was found in the literature); (ii) the negative reaction volume at the periclase/spinel growth front favors this reaction, i.e. there is no resistance to growth due to a positive reaction volume as it was suggested for the corundum substrates; the layers could grow fast and with uniform thickness into the substrates; (iii) all three phases (spinel, periclase as well as γ–Al_2O_3) possess fcc oxygen sublattices so that phase boundaries at both interfaces are coherent which facilitates the transformation to spinel; accordingly, the semi-coherent corundum/spinel phase boundary was found to be rate-limiting in the interface-controlled reaction regime in similar systems (e.g. He and Becker, 1997; Kotula et al., 1998; Pin et al., 2013b). This phase boundary is semi-coherent; the hcp oxygen sublattice of corundum has to be transformed into a fcc oxygen sublattice in spinel. In this case, a partial ion redistribu-

tion occurs along with the dislocation movement, and both processes can determine the reaction rate, provided that the exchange fluxes are high enough (Schmalzried, 1981). On the other hand, the periclase/spinel and the γ–Al_2O_3/spinel interfaces are coherent; the symmetries of the fcc oxygen sublattices do not change when they are transformed to spinel.

5 Summary

The start of a mineral reaction and the subsequent growth behavior of the product phase was monitored *in-situ* using a substrate/thin film experimental setup and synchrotron X-ray diffraction in combination with a heating attachment. Nanoscale magnesioaluminate spinel layers were synthesized at contacts between alumina polymorphs and periclase according to the reaction $Al_2O_3 + MgO \longrightarrow MgAl_2O_4$. Using these materials and methods, the growth could be observed at for this system relatively low temperatures as well as short run durations. In air, the temperature was varied from 700 to 1000 °C, and run durations lasted from 5 minutes to 3 hours.

Substrates were either (0001)-oriented corundum (α–Al_2O_3) single crystals or (111)-oriented periclase (MgO) single crystals. The oxygen sublattices of corundum and periclase are in a pseudo-hexagonal close-packed and face-centered cubic arrangement in these orientations, respectively, which allows topotaxial growth of spinel (having a face-centered cubic oxygen sublattice) into the substrates. The complementary Al_2O_3 and MgO reactant layers were deposited using the pulsed laser deposition (PLD) technique. These Al_2O_3 and MgO thin films were not thicker than 500 and 150 nm, respectively. For two additional experimental setups, a spinel seed layer (about 50 nm in thickness) was deposited between the reactants to avoid possible nucleation problems.

A novel heating attachment was aquired for the *in-situ* monitoring purposes. Our unit was modified by the manufacturer to measure the temperature at the substrate surface where the spinel-forming reaction takes place; a special second thermocouple was therefore installed into the device. The complete system consists of the heating attachment itself, a temperature control unit which is used, *inter alia*, to define target temperatures as well as heating and cooling rates, and an air service unit which provides cooling of the heating attachment at high temperatures. The system was set up and tested in several test runs before the actual *in-situ* experiments to ensure its functioning.

The *in-situ* experiments were carried out at the synchrotron facility BESSY II, situated in Berlin, Germany. First experiments were conducted at the EDDI beamline, employing the energy-dispersive mode of X-ray diffraction. In the best case, reflections of both the substrate and the thin films could be recorded in a single diffraction spectrum. In the spectra, it could be seen that the spinel layers in all experimental setups grow highly {111}-oriented. This 111 spinel Bragg reflection was then monitored during a second beamtime at the KMC-2 beamline of BESSY II, employing the angle-dispersive mode of X-ray diffraction.

No appreciable retardation of spinel growth was observed. In case the spinel-forming reaction took place, the 111 spinel Bragg reflection was always detected in the first EDDI

spectrum that was obtained at target temperature (usually recorded after 5 minutes). Depending on the temperature, at the KMC-2 beamline, the 111 spinel Bragg reflection was evaluable at the latest after 4 minutes of annealing at target temperature.

Because no sudden change in texture was observed during the *in-situ* experiments, i.e. only the 111 spinel Bragg reflections were observed, and because the attenuation of the X-rays is at most about 5 % for these materials and layer thicknesses, the evolution of the integrated intensity of the 111 spinel Bragg reflection in an experiment was used to assess the growth kinetics of the respective spinel layer. This approach is valid as it was demonstrated that the integrated intensity remains constant when the reactant layer is consumed; the moment of consumption may also be accompanied by a sudden change of the 111 spinel lattice plane distance, and the *FWHM* may not further decrease afterwards.

For the corundum substrates, growth was observed at temperatures $\geq 900\,^{\circ}\mathrm{C}$. In the 900 °C experiment, the spinel reaction band attained a thickness of $15 \pm 1\,\mathrm{nm}$ during 1 hour of annealing. This corresponds to only some 32 111 spinel lattice planes on top of each other. From the parabolic increase of the integrated intensity of the 111 spinel Bragg reflection in this experiment, a diffusion-controlled reaction regime was deduced. In this regime, the diffusion of the diffusing species is so slow that it is rate-limiting. On the other hand, the layers grew largely linearly with time at 1000 °C, and an interface-controlled reaction regime was deduced. In this regime, the diffusion is fast, but processes at the interfaces are rate-limiting. The mean linear reaction rate of spinel layer growth at 1000 °C was determined as 0.05 nm/s.

For the periclase substrates, growth was observed at temperatures $\geq 800\,^{\circ}\mathrm{C}$. In these experiments, the as-deposited amorphous Al_2O_3 layers crystallized to γ–Al_2O_3 which has a defect spinel structure. Diffusion-controlled growth was deduced at 800 °C. The spinel reaction layer attained a thickness of $21 \pm 1\,\mathrm{nm}$ during 65 minutes of annealing. Interface-controlled growth was deduced at temperatures $\geq 900\,^{\circ}\mathrm{C}$. Linear reaction rates were estimated at 6.1 nm/min at 900 °C and 43.3 nm/min at 1000 °C.

An offset of 100 °C was observed for the onset of spinel growth between the substrates. The periclase substrate samples reacted earlier and faster. The spinel growth front advanced uniformly into the substrates in this setup. It was argued that due to a negative reaction volume at the periclase/spinel interface, the layer experienced no resistance to this advancement and reaction kinetics were hence faster. Additionally, all three phases in this setup (spinel, periclase and γ–Al_2O_3) possess face-centered cubic oxygen sublattices so that phase boundaries at both interfaces are coherent which facilitates the transformation to spinel.

To determine absolute reaction band widths and to study microstructures and microtextures of the layers, samples were analyzed *ex-situ* using transmission electron microscopy (TEM). The proposed diffusion mechanism for this system — namely counter-diffusion of the cations through a relatively rigid oxygen sublattice — could be confirmed by inspection of TEM micrographs. Two spinel sublayers — a thicker, Al_2O_3-grown sublayer and a smaller, periclase-grown sublayer with approximate thickness proportions of

3:1 — could be discerned in many micrographs. These sublayers could be distinguished by a change in microstructure. Volume changes at both interfaces that follow from the reaction stoichiometry of the diffusion mechanism are also displayed in the micrographs. The positive reaction volume at the corundum substrate/spinel phase boundary is displayed by bend contours. These alternating dark and bright contrasts emerge at the interface and extend into the substrates, indicating that the Bragg planes of corundum are twisted in the vicinity of the spinel growth front due to the positive reaction volume. The bend contours scale with the thickness of the spinel layers, indicating that stress gradually builds up at this interface when spinel is formed. They appeared once the reaction took place in the two-layer setup so that they could be used to infer that a spinel seed layer expanded in the three-layer setup. The corundum substrate/spinel phase boundary was found to develop rather wavy with time; on the other hand, the periclase substrate/spinel phase boundary was always found to be straight-lined. Due to the negative reaction volume at this interface, no stress builds up, and bend contours were never observed. A porous layer directly at the interface was always found instead.

Additional texture measurements were carried out at the KMC-2 beamline. Along with diffraction patterns obtained from TEM analyses, these measurements demonstrated that the spinel layers grew topotaxially into the substrates and that rotation twins are present. The crystallites grew in such a way that with respect to the substrates the planes of close-packed oxygen ions and directions of close packing within these planes are parallel to each other.

Outlook: The experiments of this study demonstrated that it is possible to monitor *in-situ* a mineral reaction and the growth behavior of a geologically relevant mineral at the nanoscale on a reasonable laboratory timescale. In combination with an *ex-situ* analysis by TEM, the nanoscale run products and their growth behavior can be characterized outstandingly. This combination of materials and analytical methods can be used in future experiments to study the growth behavior of other minerals relevant in the Earth sciences. For instance, the growth of nanoscale enstatite layers between quartz and forsterite according to the reaction $SiO_2 + Mg_2SiO_4 \longrightarrow Mg_2Si_2O_6$ may be monitored *in-situ*.

Appendix

Table A1: List of frequently used abbreviations. More information on a specific entry can be found in the section provided in brackets.

Δt	Acquisition time for a spectrum or diffractogram
Δx	Thickness of a spinel reaction band
AFM	Atomic force microscopy (section 2.5.1)
BF	Bright-field (section 2.4)
d_{hkl}	Lattice plane distance
D	Crystallite size (section 2.3.5)
DF	Dark-field (section 2.4)
DHS	DHS 1100 Domed Hot Stage (section 2.3.1)
DP	Diffraction pattern (section 2.4)
EDDI	Beamline for energy-dispersive X-ray diffraction (section 2.3.2)
EDX	Energy dispersive X-ray spectroscopy (section 2.4)
FWHM	Full width at half maximum
esc	Escape peak(s) in diffraction spectra (section 2.3.2.3)
fcc	face-centered cubic
FL	Fluorescence lines in the diffraction spectra (section 2.3.2.3)
FIB	Focused ion beam (section 2.4)
GIXRD	Grazing incidence X-ray diffraction (section 2.5.2)
HAADF	High-angle angular dark field (section 2.4)
hcp	Hexagonal close-packed
I_B	Integral breadth
I_{hkl}	Integrated intensity of a Bragg reflection
ODF	Orientation distribution function (section 2.3.3.3)
PLD	Pulsed laser deposition (section 2.2)
SEM	Scanning electron microscopy (section 2.5.1)
T_{DHS}	Temperature at the sample plate (section 2.3.1)
T_{sub}	Temperature at the substrate surface (section 2.3.1)
TCU	TCU 200 Temperature Control Unit (section 2.3.1)
TEM	Transmission electron microscopy (section 2.4)
TI	Texture index (section 2.3.3.3)

Table A2: Overview of corundum substrate samples. Two-layer setup (top entries): only one pole figure was measured for sample Cor30. Three-layer setup (bottom entries): for sample Cor23, spinel reflections were only detected during the heating and cooling stages of the experiment, but they vanished at target temperature. DPs were collected from both samples that were analyzed by TEM.

Sample	Beamline	T [°C]	t [min]	Texture	TEM
Cor8	KMC-2	1000	180.2	+	+
Cor9	KMC-2	1000	120.1	+	+
Cor24	EDDI	700	61.7	−	+
Cor25	EDDI	800	61.1	−	+
Cor26	EDDI	900	60.6	−	+
Cor27	EDDI	1000	5	+	+
Cor28	EDDI	1000	61.7	+	+
Cor29	EDDI	1000	30.8	−	+
Cor30	EDDI	1000	119.3	±	+
Cor16	EDDI	800	40.3	+	−
Cor17	KMC-2	1000	10.9	−	−
Cor18	EDDI	900	40.3	−	+
Cor21	EDDI	1000	40.3	−	+
Cor22	EDDI	1000	120.3	+	−
Cor23	EDDI	1000	82.3	−	−

Table A3: Overview of periclase substrate samples. Two-layer setup (top entries): only one pole figure was measured for sample Per27. Three-layer setup (bottom entries): DPs were collected from both samples that were analyzed by TEM.

Sample	Beamline	T [°C]	t [min]	Texture	TEM
Per24	EDDI	1000	5	+	+
Per26	EDDI	1000	60.4	+	+
Per27	KMC-2	900	65.5	±	+
Per28	EDDI	1000	30.2	+	+
Per29	KMC-2	800	65.1	−	+
Per17	EDDI	1000	40.3	+	+
Per18	KMC-2	900	43.9	−	+
Per19	KMC-2	800	43.2	−	−
Per20	KMC-2	1000	11.4	−	−
Per21	KMC-2	700	41.9	−	−
Per22	KMC-2	1000	21.7	−	−

Bibliography

Abart R., Petrishcheva E. (2011): Thermodynamic Model For Reaction Rim Growth: Interface Reaction and Diffusion Control. American Journal of Science, 311: 517-527. DOI: 10.2475/06.2011.02

Abart R., Petrishcheva E., Fischer F. D., Svoboda J. (2009): Thermodynamic model for diffusion controlled reaction rim growth in a binary system: Application to the forsterite–enstatite–quartz system. American Journal of Science, 309: 114-131. DOI: 10.2475/02.2009.02

Alper A. M., McNally R. N., Ribbe P. H., Doman R. C. (1962): The System MgO–$MgAl_2O_4$. Journal of The American Ceramic Society, 45: 263-268

Apel D., Klaus M., Genzel C., Balzar D. (2011): Rietveld refinement of energy-dispersive synchrotron measurements. Zeitschrift für Kristallographie, 226: 934-943. DOI: 10.1524/zkri.2011.1436

Bachmann F., Hielscher R., Schaeben H. (2010): Texture Analysis with MTEX – Free and Open Source Software Toolbox. Solid State Phenomena, 160: 63-68. DOI: 10.4028/www.scientific.net/SSP.160.63

Baer D. R., Thevuthasan S. (2010): Characterization of Thin Films and Coatings. In *Handbook of Deposition Technologies for Films and Coatings – Science, Applications and Technology* edited by P. M. Martin. Elsevier Inc. ISBN: 978-0-8155-2031-3

Barbier A., Mocuta C., Renaud G. (2001): *In situ* Synchrotron Structural Studies of the Growth of Oxides and Metals. In *Handbook of Thin Films, Five-Volume Set* edited by H. S. Nalwa. Academic Press. ISBN: 978-0-12-512908-4

Bengtson B., Jagitsch R. (1947): Kinetic Studies on Formation of Spinel from Zinc Oxide and Alumina. Arkiv för Kemi, Mineralogi och Geologi, 24A: 1-16

Birkholz M. (2006): Thin Film Analysis by X-Ray Scattering. WILEY-VCH Verlag. ISBN: 978-3-527-31052-4

Blanton T. N., Hung L.-S. (1996): X-ray Diffraction Characterization of Multilayer Epitaxial Thin-Films Deposited on (0001) Sapphire. The Rigaku Journal, 13: 3-7

Blum W. C. (1997): Zum Einfluß elastischer Spannungen auf Phasenbildungs- und Transformationsprozesse im Dünnschichtsystem MgO–GeO_2. Dissertation, Martin-Luther-Universität Halle-Wittenberg. Shaker Verlag. ISBN: 3-8265-2869-7

Boese M. U. (2004): Herstellung und Charakterisierung epitaktischer Spinellbeschichtungen auf Korund und Analyse der Grenzflächen. Dissertation, Rheinische Friedrich-Wilhelms-Universität Bonn.

Carter C. B., Norton M. G. (2007): Ceramic Materials – Science and Engineering. Springer. ISBN: 978-0-387-46270-7

Carter C. B., Schmalzried H. (1985): The growth of spinel into Al_2O_3. Philosophical Magazine A, 52: 207-224

Carter R. E. (1961): Mechanism of Solid-State Reaction Between Magnesium Oxide and Aluminum Oxide and Between Magnesium Oxide and Ferric Oxide. Journal of The American Ceramic Society, 44: 116-120

Choi C.-H., Harper R. A., Yapsir A. S., Lu T. M. (1987): Epitaxial growth of Al(111)/ Si(111) films using partially ionized beam deposition. Applied Physics Letters, 51: 1992-1994

Comer J. J., Tombs N. C., Fitzgerald J. F. (1966): Growth of Single-Crystal and Polycrystalline Thin Films of $MgAl_2O_4$ and $MgFe_2O_4$. Journal of The American Ceramic Society, 49: 237-240

Connolly J. A. D. (1990): Multivariable phase diagrams: an algorithm based on generalized thermodynamics. American Journal of Science, 290: 666-718

Connolly J. A. D. (2005): Computation of phase equilibria by linear programming: A tool for geodynamic modeling and its application to subduction zone decarbonation. Earth and Planetary Science Letters, 236: 524-541. DOI: 10.1016/j.epsl.2005.04.033

Creagh D. C., Hubbell J. H. (2004): X-ray absorption (or attenuation) coefficients. In *International Tables for Crystallography – Volume C: Mathematical, Physical and Chemical Tables* edited by E. Prince. Kluwer Academic Publishers. ISBN: 1-4020-1900-9

Cserháti C., Balogh Z., Csik A., Langer G. A., Erdélyi Z., Glodán G., Katona G. L., Beke D. L., Zizak I., Darowski N., Dudzik E., Feyerherm R. (2008): Linear growth kinetics of nanometric silicides in Co/amorphous-Si and Co/CoSi/amorphous-Si thin films. Journal of Applied Physics, 104: 024311. DOI: 10.1063/1.2957071

Deal B. E, Grove A. S. (1965): General Relationship for the Thermal Oxidation of Silicon. Journal of Applied Physics, 36: 3770-3778. DOI:10.1063/1.1713945

Deer W. A., Howie R. A., Zussman J. (1992): An Introduction to the Rock Forming Minerals. Longman. ISBN: 978-0-582-30094-1

Denks I. A., Genzel C. (2007): Enhancement of energy dispersive residual stress analysis by consideration of detector electronic effects. Nuclear Instruments and Methods in Physics Research B, 262: 87-94. DOI: 10.1016/j.nimb.2007.05.007

Dohmen R., Becker H.-W., Meißner E., Etzel T., Chakraborty S. (2002): Production of silicate thin films using pulsed laser deposition (PLD) and applications to studies in mineral kinetics. European Journal of Mineralogy, 14: 1155-1168. DOI: 10.1127/0935-1221/2002/0014-1155

Duckwitz C. A., Schmalzried H. (1971): Reaktionen zwischen festen Oxiden unter Einschluß von Gastransport. Zeitschrift für Physikalische Chemie Neue Folge, 76: 173-193

Dybkov V. I. (1986): Reaction diffusion in heterogeneous binary systems. Part 2 Growth of the chemical compound layers at the interface between two elementary substances: two compound layers. Journal of Material Sciences, 21: 3085-3090

Eason R. (2007): Pulsed Laser Deposition of Thin Films – Applications-Led Growth of Functional Materials. John Wiley & Sons, Inc. ISBN: 978-0-471-44709-2

Engler O., Randle V. (2010): Introduction to Texture Analysis – Macrotexture, Microtexture, and Orientation Mapping. CRC Press. ISBN: 978-1-4200-6365-3

Erko A., Packe I., Hellwig C., Fieber-Erdmann M., Pawlizki O., Veldkamp M., Gudat W. (2000): KMC-2: the New X-ray Beamline at BESSY II. AIP Conference Proceedings, 521: 415-418. DOI: 10.1063/1.1291824

Fabriès J. (1979): Spinel-Olivine Geothermometry in Peridotites From Ultramafic Complexes. Contributions to Mineralogy and Petrology, 69: 329-336

Fan H. J., Knez M., Scholz R., Nielsch K., Pippel E., Hesse D., Zacharias M., Gösele U. (2006): Monocrystalline spinel nanotube fabrication based on the Kirkendall effect. Nature Materials, 5: 627-631. DOI: 10.1038/nmat1673

Fan H. J., Gösele U., Zacharias M. (2007): Formation of Nanotubes and Hollow Nanoparticles Based on Kirkendall and Diffusion Processes: A Review. Small, 7: 1660-1671. DOI: 10.1002/smll.200700382

Fan H. J., Knez M., Scholz R., Hesse D., Nielsch K., Zacharias M., Gösele U. (2007b): Influence of Surface Diffusion on the Formation of Hollow Nanostructures Induced by the Kirkendall Effect: The Basic Concept. Nano Letters, 7: 993-997. DOI: 10.1021/nl070026p

Farrell H. H., Gilmer G. H., Suenaga M. (1975): Diffusion mechanisms for growth of Nb_3Sn intermetallic layers. Thin Solid Films, 25: 253-264

Fultz B., Howe J. (2008): Transmission Electron Microscopy and Diffractometry of Materials. Springer. ISBN: 978-3-540-73885-5

Gardés E., Wunder B., Wirth R., Heinrich W. (2011): Growth of multilayered polycrystalline reaction rims in the MgO–SiO_2 system, part I: experiments. Contributions to Mineralogy and Petrology, 161: 1-12. DOI: 10.1007/s00410-010-0517-z

Genzel C., Denks I. A., Klaus M. (2006): The Materials Science Beamline EDDI for Energy-Dispersive Analysis of Subsurface Residual Stress Gradients. Materials Science Forum, 524-525: 193-198. DOI: 10.4028/www.scientific.net/MSF.524-525.193

Genzel C., Denks I. A., Gibmeier J., Klaus M., Wagener G. (2007): The materials science synchrotron beamline EDDI for energy-dispersive diffraction analysis. Nuclear Instruments and Methods in Physics Research A, 578: 23-33. DOI: 10.1016/j.nima.2007.05.209

Ghigna P., Pin S., Spinolo G., Newton M. A., Tarantino S. C., Zema M. (2011): Synchrotron radiation in solid state chemistry. Radiation Physics and Chemistry, 80: 1109-1111. DOI: 10.1016/j.radphyschem.2011.02.014

Giannuzzi L. A., Stevie F. A. (2005): Introduction to Focused Ion Beams: Instrumentation, Theory, Techniques and Practice. Springer. ISBN: 0-387-23116-1

Gösele U., Tu K. N. (1982): Growth kinetics of planar binary diffusion couples: "Thin-film case" versus "Bulk cases". Journal of Applied Physics, 53: 3252-3260. DOI: 10.1063/1.331028

Götze L. C., Abart R., Rybacki E., Keller L. M., Petrishcheva E., Dresen G. (2010): Reaction rim growth in the system MgO–Al_2O_3–SiO_2 under uniaxial stress. Mineralogy and Petrology, 99: 263-277. DOI: 10.1007/s00710-009-0080-3

Götze L. C., Abart R., Milke R., Schorr S., Zizak I., Dohmen R., Wirth R. (2014): Growth of magnesio-aluminate spinel in thin film geometry: in situ monitoring using synchrotron X-ray diffraction and thermodynamic model. Physics and Chemistry of Minerals, 41: 681-693. DOI: 10.1007/s00269-014-0682-0

Graff A., Senz S., Zakharov N. D., Hesse D. (1998): Structure of the Topotaxial $MgSn_2O_4$/MgO Solid Reaction Front. Zeitschrift für Physikalische Chemie, 206: 117-128

Greenwood N. N., Earnshaw A. (1990): Chemie der Elemente. VCH Verlagsgesellschaft. ISBN: 3-527-26169-9

Grundmann M. (2011): Formation of epitaxial domains: Unified theory and survey of experimental results. Physica Status Solidi B, 248: 805-824. DOI: 10.1002/pssb.201046530

Güder F., Yang Y., Goetze S., Berger A., Scholz R., Hiller D., Hesse D., Zacharias M. (2011): Toward Discrete Multilayered Composite Structures: Do Hollow Networks Form in a Polycrystalline Infinite Nanoplane by the Kirkendall Effect? Chemistry of Materials, 23: 4445-4451. DOI: 10.1021/cm201446y

Gupta R. K., Yakuphanoglu F. (2011): Epitaxial growth of $MgFe_2O_4$ (111) thin films on sapphire (0001) substrate. Materials Letters, 65: 3058-3060. DOI: 10.1016/j.matlet.2011.06.091

Gutiérrez G., Taga A., Johansson B. (2002): Theoretical structure determination of γ–Al_2O_3. Physical Review B, 65: 012101. DOI: 10.1103/PhysRevB.65.012101

Haggerty, S. E. (1991): Oxide Mineralogy of the Upper Mantle. In *Oxide Minerals: Petrologic and Magnetic Significance* edited by D. H. Lindsley. Mineralogical Society of America. ISBN: 0-939950-30-8

Hallstedt B. (1992): Thermodynamic Assessment of the System MgO–Al_2O_3. Journal of The American Ceramic Society, 75: 1497-1507

Hazen R. M. (1976): Effects of temperature and pressure on the cell dimension and X-ray temperature factors of periclase. American Mineralogist, 61: 266-271

He, B. B. (2009): Two-Dimensional X-Ray Diffraction. John Wiley & Sons, Inc. ISBN: 978-0-470-22722-0

He T., Becker K. D. (1997): An optical in-situ study of a reacting spinel crystal. Solid State Ionics, 101-103: 337-342

Helpa V., Rybacki E., Abart R., Morales L. F. G., Rhede D., Jeřábek P., Dresen G. (2014): Reaction kinetics of dolomite rim growth. Contributions to Mineralogy and Petrology, 167: 1001. DOI: 10.1007/s00410-014-1001-y

Hesse D., Senz S., Scholz R., Werner P., Heydenreich J. (1994): Structure and Morphology of the Reaction Fronts During the Formation of $MgAl_2O_4$ Thin Films by Solid State Reaction Between *R*-cut Sapphire Substrates and MgO Films. Interface Science, 2: 221-237

Hielscher R., Mainprice D., Schaeben H. (2010): Material Behavior: Texture and Anisotropy. In *Handbook of Geomathematics* edited by W. Freeden, M. Z. Nashed, T. Sonar. Springer. ISBN: 978-3-642-01545-8

Hielscher R., Schaeben H. (2008): A novel pole figure inversion method: specification of the *MTEX* algorithm. Journal of Applied Crystallography, 41: 1024-1037. DOI: 10.1107/S0021889808030112

Hill R. J., Craig J. R., Gibbs G. V. (1979): Systematics of the Spinel Structure Type. Physics and Chemistry of Minerals, 4: 317-339

Holland T. J. B., Powell R. (1998): An internally consistent thermodynamic dataset for phases of petrological interest. Journal of Metamorphic Geology, 16: 309-343. DOI: 10.1111/j.1525-1314.1998.00140.x

Jeřábek P., Abart R., Rybacki E., Habler G. (2014): Microstructure and texture evolution during growth of magnesio-aluminate spinel at corundum-periclase interfaces under uniaxial load: the effect of stress concentration on reaction progress. American Journal of Science, 314: 940-965. DOI: 10.2475/05.2014.02

Joachim B., Gardés E., Abart R., Heinrich W. (2011): Experimental growth of åkermanite reaction rims between wollastonite and monticellite: evidence for volume diffusion control. Contributions to Mineralogy and Petrology, 161: 389-399. DOI: 10.1007/s00410-010-0538-7

Keller L. M., Götze L. C., Rybacki E., Dresen G., Abart R. (2010): Enhancement of solid-state reaction rates by non-hydrostatic stress effects on polycrystalline diffusion kinetics. American Mineralogist, 95: 1399-1407. DOI: 10.2138/am.2010.3372

Kirkendall E. O. (1942): Diffusion of zinc in alpha brass. Transactions of the AIME, 147: 104-109

Knoll E., Bialas H. (1994): Growth modes of epitaxial copper films on c-sapphire. Thin Solid Films, 250: 42-46

Koch E., Wagner C. (1936): Formation of Ag_2HgI_4 from AgI and HgI_2 by Reaction in the Solid State. Zeitschrift für Physikalische Chemie, B34: 317-321

Kotula P. G., Carter C. B. (1995): Volume expansion and lattice rotations in solid-state reactions between oxides. Scripta Metallurgica et Materialia, 32: 863-866

Kotula P. G., Carter C. B. (1996): Interfacial Control of Reaction Kinetics in Oxides. Physical Review Letters, 77: 3367-3370

Kotula P. G., Johnson M. T., Carter C. B. (1998): Thin-Film Reactions. Zeitschrift für Physikalische Chemie, 206: 73-99

Le Bail A. (2005): Whole powder pattern decomposition methods and applications: A retrospection. Powder Diffraction, 20: 316-326. DOI: 10.1154/1.2135315

Le Bail A., Duroy H., Fourquet J. L. (1988): Ab-initio structure determination of $LiSbWO_6$ by X-ray powder diffraction. Material Research Bulletin, 23: 447-452

Lee J. H., Eun J. H., Kim S. G., Park S. Y., Lee M. J., Kim H. J. (2003): Hydration behavior of MgO single crystals and thin films. Journal of Materials Research, 18: 2895-2903. DOI: 10.1557/JMR.2003.0404

Lee W. E., Lagerlof K. P. D. (1985): Structural and Electron Diffraction Data for Sapphire (α–Al_2O_3). Journal of Electron Microscopy Technique, 2: 247-258. DOI: 10.1002/jemt.1060020309

Levin I., Brandon D. (1998): Metastable Alumina Polymorphs: Crystal Structures and Transition Sequences. Journal of the American Ceramic Society, 81: 1995-2012

Li D. X., Pirouz P., Heuer A. H., Yadavalli S., Flynn C. P. (1992): A high-resolution electron microscopy study of MgO/Al_2O_3 interfaces and $MgAl_2O_4$ spinel formation. Philosophical Magazine A, 65: 403-425. DOI: 10.1080/01418619208201530

Li Z., Wang L., Suzuki T., Argoitia A., Pirouz P., Angus J. C. (1993): Orientation relationship between chemical vapor deposited diamond and graphite substrates. Journal of Applied Physics, 73: 711-715. DOI: 10.1063/1.353327

Lippens B. C., De Boer J. H. (1964): Study of Phase Transformations During Calcination of Aluminum Hydroxides by Selected Area Electron Diffraction. Acta Crystallographica, 17: 1312-1321

Liu C.-M., Chen J.-C., Chen C.-J. (2005): The growth of an epitaxial Mg–Al spinel layer on sapphire by solid-state reactions. Journal of Crystal Growth, 285: 275-283. DOI: 10.1016/j.jcrysgro.2005.08.023

Mackenzie K. J. D., Ryan M. J. (1981): Effect of electric fields on solid-state reactions between oxides – Part 3 Interdiffusion in polycrystalline magnesium and aluminium oxide pellets. Journal of Materials Science, 16: 579-588

Martin P. M. (2010): Handbook of Deposition Technologies for Films and Coatings – Science, Applications and Technology. Elsevier Inc. ISBN: 978-0-8155-2031-3

Martínez-Boubeta C., Botana A. S., Pardo V., Baldomir D., Antony A., Bertomeu J., Rebled J. M., López-Conesa L., Estradé S., Peiró F. (2012): Heteroepitaxial growth of MgO(111) thin films on Al_2O_3(0001): Evidence of a wurtzite to rocksalt transformation. Physical Review B, 86: 041407(R). DOI: 10.1103/PhysRevB.86.041407

Mason J. K., Schuh C. A. (2009): Representations of Texture. In *Electron Backscatter Diffraction in Materials Science* edited by A. J. Schwartz, M. Kumar, B. L. Adams, D. P. Field. Springer. ISBN: 978-0-387-88135-5

Matthes S. (2001): Mineralogie – Eine Einführung in die spezielle Mineralogie, Petrologie und Lagerstättenkunde. Springer. ISBN: 3-540-67423-3

Mattox D. M. (2010): Non-Elemental Characterization of Films and Coatings. In *Handbook of Deposition Technologies for Films and Coatings – Science, Applications and Technology* edited by P. M. Martin. Elsevier Inc. ISBN: 978-0-8155-2031-3

Merckling C., El-Kazzi M., Favre-Nicolin V., Gendry M., Robach Y., Grenet G., Hollinger G. (2007): Epitaxial growth and relaxation of γ–Al_2O_3 on silicon. Thin Solid Films, 515: 6479-6483. DOI: 10.1016/j.tsf.2006.11.157

Milke R., Wirth R. (2003): The formation of columnar fiber texture in wollastonite rims by induced stress and implications for diffusion-controlled corona growth. Physics and Chemistry of Minerals, 30: 230-242. DOI: 10.1007/s00269-003-0304-8

Milke R., Wiedenbeck M., Heinrich W. (2001): Grain boundary diffusion of Si, Mg, and O in enstatite reaction rims: a SIMS study using isotopically doped reactants. Contributions to Mineralogy and Petrology, 142: 15-26. DOI: 10.1007/s004100100277

Milke R., Dohmen R., Becker H.-W., Wirth R. (2007): Growth kinetics of enstatite reaction rims studied on nano-scale, Part I: Methodology, microscopic observations and the role of water. Contributions to Mineralogy and Petrology, 154: 519-533. DOI: 10.1007/s00410-007-0207-7

Milke R., Kolzer K., Koch-Müller M., Wunder B. (2009): Orthopyroxene rim growth between olivine and quartz at low temperatures (750–950°C) and low water concentration. Mineralogy and Petrology, 97: 223-232. DOI: 10.1007/s00710-009-0093-y

Nakajima H. (1997): The Discovery and Acceptance of the Kirkendall Effect: The Result of a Short Research Career. Journal of the Minerals, Metals & Materials Society, 49: 15-19

Nason T. C., You L., Yang G.-R., Lu T.-M. (1991): Growth of epitaxial Ag/Si films by the partially ionized beam deposition technique. Journal of Applied Physics, 69: 773-777. DOI: 10.1063/1.347363

Navias L. (1961): Preparation and Properties of Spinel Made by Vapor Transport and Diffusion in the System MgO–Al_2O_3. Journal of The American Ceramic Society, 44: 434-446

Navrotsky A., Wechsler B. A., Geisinger K., Seifert F. (1986): Thermochemistry of $MgAl_2O_4$–$Al_{8/3}O_4$ Defect Spinels. Journal of The American Ceramic Society, 69: 418-422

Norton D. P. (2007): Pulsed Laser Deposition of Complex Materials: Progress Towards Applications. In *Pulsed Laser Deposition of Thin Films – Applications-Led Growth of Functional Materials* edited by R. Eason. John Wiley & Sons, Inc. ISBN: 978-0-471-44709-2

O'Neill H. S. C., Navrotsky A. (1983): Simple spinels: crystallographic parameters, cation radii, lattice energies, and cation distribution. American Mineralogist, 68: 181-194

Paar A. (2011): Instruction Manual DHS 1100 Domed Hot Stage. Published by Anton Paar. Document number: C58IB002EN-C

Paar A. (2011b): Instruction Manual TCU 200 Temperature Control Unit for DHS 1100. Published by Anton Paar. Document number: B39IB020en-B

Pettit F. S., Randklev E. H., Felten E. J. (1966): Formation of $NiAl_2O_4$ by Solid State Reaction. Journal of The American Ceramic Society, 49: 199-203

Pin S., Suardelli M., D'Acapito F., Spinolo G., Zema M., Tarantino S. C., Ghigna P. (2013): Role of Interfacial Energy and Crystallographic Orientation on the Mechanism of the $ZnO + Al_2O_3 \longrightarrow ZnAl_2O_4$ Solid-State Reaction: I. Reactivity of Films Deposited onto the Sapphire (110) and (012) Faces. The Journal of Physical Chemistry C, 117: 6105-6112. DOI: 10.1021/jp3124956

Pin S., Suardelli M., D'Acapito F., Spinolo G., Zema M., Tarantino S. C., Barba L., Ghigna P. (2013b): Role of Interfacial Energy and Crystallographic Orientation on the Mechanism of the $ZnO + Al_2O_3 \longrightarrow ZnAl_2O_4$ Solid-State Reaction: II. Reactivity of Films Deposited onto the Sapphire (001) Face. The Journal of Physical Chemistry C, 117: 6113-6119. DOI: 10.1021/jp312517w

Pirouz P., Yang J. (1990): Anti-Site Bonds and the Structure of Interfaces in SiC. MRS Proceedings, 183: 173. DOI: 10.1557/PROC-183-173

Redfern S. A. T., Harrison R. J., O'Neill H. S. C., Wood D. R. R. (1999): Thermodynamics and kinetics of cation ordering in $MgAl_2O_4$ spinel up to 1600 °C from in situ neutron diffraction. American Mineralogist, 84: 299-310

Resel R., Tamas E., Sonderegger B., Hofbauer P., Keckes J. (2003): A heating stage up to 1173 K for X-ray diffraction studies in the whole orientation space. Journal of Applied Crystallography, 36: 80-85. DOI: 10.1107/S0021889802019568

Rodríguez-Gonzalez B., Pastoriza-Santos I., Liz-Marzán L. M. (2006): Bending Contours in Silver Nanoprisms. The Journal of Physical Chemistry B, 110: 11796-11799. DOI: 10.1021/jp061195l

Rossi R. C., Fulrath R. M. (1963): Epitaxial Growth of Spinel by Reaction in the Solid State. Journal of The American Ceramic Society, 46: 145-149

Saitoh H., Okada Y., Ohshio S. (2002): Synthesis of MgO/ZnO hetero-epitaxial whiskers using chemical vapor deposition operated under atmospheric pressure. Journal of Materials Science, 37: 4597-4602. DOI: 10.1023/A:1020696215411

Salmang H., Scholze H. (2007): Keramik. Springer. ISBN: 978-3-540-63273-3

Schmalzried H., Wagner C. (1962): Fehlordnung in ternären Ionenkristallen. Zeitschrift für Physikalische Chemie Neue Folge, 31: 198-221

Schmalzried H. (1974): Solid-state reactions between oxides. In *Defects and transport in oxides* edited by M. S. Seltzer and R. I. Jaffee. Plenum Press. ISBN: 978-1-4615-8725-5

Schmalzried H. (1978): Reactivity and Point Defects of Double Oxides With Emphasis on Simple Silicates. Physics and Chemistry of Minerals, 2: 279-294

Schmalzried H. (1978b): The Role of Phase Boundaries in Heterogeneous Solid State Reactions (I) Classification and the Dynamic Equilibrium at Interfaces. Berichte der Bunsengesellschaft für physikalische Chemie, 82: 273-277

Schmalzried H. (1981): Solid State Reactions. Verlag Chemie. ISBN: 3-527-25872-8

Schmalzried H. (1995): Chemical Kinetics of Solids. VCH Verlagsgesellschaft mbH. ISBN: 3-527-29094-X

Schou J. (2009): Physical aspects of the pulsed laser deposition technique: The stoichiometric transfer of material from target to film. Applied Surface Science, 255: 5191-5198. DOI: 10.1016/j.apsusc.2008.10.101

Shaginyan L. R., (2001): Pulsed Laser Deposition of Thin Films: Expectations and Reality. In *Handbook of Thin Films, Five-Volume Set* edited by H. S. Nalwa. Academic Press. ISBN: 978-0-125-12908-4

Shah S. I., Jaffari G. H., Yassitepe E., Ali B. (2010): Evaporation: Processes, Bulk Microstructures, and Mechanical Properties. In *Handbook of Deposition Technologies for Films and Coatings – Science, Applications and Technology* edited by P. M. Martin. Elsevier Inc. ISBN: 978-0-8155-2031-3

Sickafus K. E., Wills J. M. (1999): Structure of Spinel. Journal of the American Ceramic Society, 82: 3279-3292. DOI: 10.1111/j.1151-2916.1999.tb02241.x

Sieber H., Hesse D., Pan X., Senz S., Heydenreich J. (1996): TEM Investigations of Spinel-forming Solid State Reactions: Reaction Mechanism, Film Orientation, and Interface Structure during $MgAl_2O_4$ Formation on MgO (001) and Al_2O_3 ($1\bar{1}.2$) Single Crystal Substrates. Zeitschrift für anorganische und allgemeine Chemie, 622: 1658-1666

Sieber H., Hesse D. Werner P. (1997): Misfit accommodation mechanisms at moving reaction fronts during topotaxial spinel-forming thin-film solid-state reactions: a high-resolution transmission electron microscopy study of five spinels of different misfits. Philosophical Magazine A, 75: 889-908

Sieber H., Hesse D., Werner P., Senz S. (1997b): Differences in the Defect Structures of the Reaction Fronts of Solid State Reactions within Interface- and Diffusion-Controlled Reaction Regimes. Defect and Diffusion Forum, 143-147: 649-654

Sieber H., Werner P., Hesse D. (1997c): The atomic structure of the reaction front as a function of the kinetic regime of a spinel-forming solid-state reaction. Philosophical Magazine A, 75: 909-924

Simpson T. W., Wen Q., Yu N., Clarke D. R. (1998): Kinetics of the Amorphous $\longrightarrow$ γ $\longrightarrow$ α Transformations in Aluminum Oxide: Effect of Crystallographic Orientation. Journal of the American Ceramic Society, 81: 61-66. DOI: 10.1111/j.1151-2916.1998.tb02296.x

Smigelskas A. D., Kirkendall E. O. (1947): Zinc diffusion in alpha brass. Transactions of the AIME, 171: 130-142

Spieß L., Teichert G., Schwarzer R., Behnken H., Genzel C. (2009): Moderne Röntgenbeugung – Röntgendiffraktometrie für Materialwissenschaftler, Physiker und Chemiker. Vieweg+Teubner. ISBN: 978-3-8351-0166-1

Stampe P. A., Bullock M., Tucker W. P., Kennedy R. J. (1999): Growth of MgO thin films on *M*-, *A*-, *C*- and *R*-plane sapphire by laser ablation. Journal of Physics D: Applied Physics, 32: 1778-1787. DOI: 10.1088/0022-3727/32/15/304

Sutcu M., Akkurt S., Okur S. (2009): Influence of crystallographic orientation on hydration of MgO single crystals. Ceramics International, 35: 2571-2576. DOI: 10.1016/j.ceramint.2009.02.012

Suzuki T., Yagi M., Shibuki K. (1994): Growth of oriented diamond on single crystal of silicon carbide (0001). Applied Physics Letters, 64: 557-559. DOI: 10.1063/1.111102

Tanner C. M., Sawkar-Mathur M., Lu J., Blom H.-O., Toney M. F., Chang J. P. (2007): Structural properties of epitaxial γ–Al_2O_3 (111) thin films on 4*H*–SiC (0001). Applied Physics Letters, 90: 061916. DOI: 10.1063/1.2435978

Thirsk H. R., Whitmore E. J. (1940): An electron diffraction study of the surface reaction between nickel oxide and corundum. Transactions of the Faraday Society, 35: 565-574. DOI: 10.1039/TF9403500565

Thompson C. V. (1990): Grain Growth in Thin Films. Annual Review of Materials Research, 20: 245-268. DOI: 10.1146/annurev.ms.20.080190.001333

Verwey E. J. W., Heilmann E. L. (1947): Physical Properties and Cation Arrangement of Oxides with Spinel Structures – I. Cation Arrangement in Spinels. The Journal of Chemical Physics, 15: 174-180. DOI: 10.1063/1.1746464

Wasa K., Kitabatake M., Adachi H. (2004): Thin Film Materials Technology – Sputtering of Compound Materials. Springer. ISBN: 3-540-21118-7

Watson E. B., Price J. D. (2002): Kinetics of the reaction MgO + Al_2O_3 ⟶ $MgAl_2O_4$ and Al–Mg interdiffusion in spinel at 1200 to 2000°C and 1.0 to 4.0 GPa. Geochimica et Cosmochimica Acta, 66: 2123-2138. DOI: 10.1016/S0016-7037(02)00827-X

Whitney II W. P., Stubican V. S. (1971): Interdiffusion Studies in the System MgO–Al_2O_3. Journal of Physics and Chemistry of Solids, 32: 305-312

Williams D. B., Carter C. B. (2009): Transmission Electron Microscopy – A Textbook for Materials Science. Springer. ISBN: 978-0-387-76500-6

Wirth R. (2004): Focused Ion Beam (FIB): A novel technology for advanced application of micro- and nanoanalysis in geosciences and applied mineralogy. European Journal of Mineralogy, 16: 863-876. DOI: 10.1127/0935-1221/2004/0016-0863

Wirth R. (2009): Focused Ion Beam (FIB) combined with SEM and TEM: Advanced analytical tools for studies of chemical composition, microstructure and crystal structure in geomaterials on a nanometre scale. Chemical Geology, 261: 217-229. DOI: 10.1016/j.chemgeo.2008.05.019

Wojdyr M. (2010): Fityk: a general-purpose peak fitting program. Journal of Applied Crystallography, 43: 1126-1128. DOI: 10.1107/S0021889810030499

Wood B. J., Kirkpatrick R. J., Montez B. (1986): Order-disorder phenomena in $MgAl_2O_4$ spinel. American Mineralogist, 71: 999-1006

Wood B. J., Kiseeva E. S., Matzen A. K. (2013): Garnet in the Earth's Mantle. Elements, 9: 421-426. DOI: 10.2113/gselements.9.6.421

Wu S. Y., Hong M., Kortan A. R., Kwo J., Mannaerts J. P., Lee W. C., Huang Y. L. (2005): High-quality thin single-crystal γ–Al_2O_3 films grown on Si (111). Applied Physics Letters, 87: 091908. DOI: 10.1063/1.2037205

Yang Y., Kim D. S., Knez M., Scholz R., Berger A., Pippel E., Hesse D., Gösele U., Zacharias M. (2008): Influence of Temperature on Evolution of Coaxial ZnO/Al_2O_3 One-Dimensional Heterostructures: From Core–Shell Nanowires to Spinel Nanotubes and Porous Nanowires. The Journal of Physical Chemistry C, 112: 4068-4074. DOI: 10.1021/jp710948j

Yund R. A. (1997): Rates of grain boundary diffusion through enstatite and forsterite reaction rims. Contributions to Mineralogy and Petrology, 126: 224-236

Zhang P., Debroy T., Seetharaman S. (1996): Interdiffusion in the MgO–Al_2O_3 Spinel With or Without Some Dopants. Metallurgical and Materials Transactions A, 27A: 2105-2114

Zhou R.-S., Snyder R. L. (1991): Structures and Transformation Mechanisms of the η, γ and θ Transition Aluminas. Acta Crystallographica, B47: 617-630

Eidesstattliche Erklärung

Hiermit versichere ich, dass ich die vorliegende Arbeit selbstständig verfasst und keine anderen als die angegebenen Hilfsmittel benutzt habe. Die Stellen der Arbeit, die anderen Publikationen wörtlich oder inhaltlich entnommen worden sind, wurden durch entsprechende Angaben der Quellen kenntlich gemacht.

Berlin, 4.2.2015

Danksagung

Ich möchte an dieser Stelle alle Kollegen an den verschiedenen Universitäten und Instituten, an welchen ich während dieser Zeit gearbeitet habe, grüßen und insbesondere allen Kollegen danken, die zum Gelingen dieser Arbeit beigetragen haben.

Ich bedanke mich zuallererst bei meinen Betreuern Prof. Dr. Susan Schorr und Dr. Ralf Milke für das Vertrauen und die Unterstützung. Ich bedanke mich recht herzlich bei Jim Pauly für die Durchsicht dieser Arbeit und nützliche Verbesserungsvorschläge. Ich grüße ferner alle anderen Kollegen im Arbeitsbereich Mineralogie-Petrologie der FU Berlin.

Ich grüße die Kollegen der Abteilung Kristallographie am Helmholtz-Zentrum Berlin (HZB). Ich bedanke mich recht herzlich bei Dr. Manuela Klaus, Prof. Dr. Christoph Genzel und Dr. Ivo Zizak für die vorzügliche Betreuung an den Beamlines während meiner zwei Strahlzeiten in Adlershof bei BESSY II. René Gunder sei dabei gedankt für das Aushelfen bei meinen Messungen während beider Strahlzeiten.

Am Helmholtz-Zentrum Potsdam (GFZ) grüße ich alle Kollegen der Sektionen Geomechanik und Rheologie und Chemie und Physik der Geomaterialien, mit denen ich während meiner Studien- und Doktorandenzeit zusammengearbeitet habe. Für die Hilfe in diesem Projekt danke ich ganz herzlich Anja Schreiber und Dr. Richard Wirth für die Präparation bzw. Analyse von TEM-Folien. Ebenso sei Dr. Luiz Morales für die Betrachtung von einigen Proben mit dem Zweistrahlmikroskop gedankt. Ich danke desweiteren Dr. Katharina Marquardt für Diskussionen und Tipps bezüglich der Beschichtungen. Stefan Gehrmann sei gedankt für Präparationsarbeiten.

An der Ruhr-Universität Bochum danke ich Dr. Ralf Dohmen für die Hilfe am Excimerlaser. Es seien auch alle anderen Kollegen gegrüßt, die ich dort kennengelernt habe.

An der Universität Wien bedanke ich mich bei Prof. Dr. Rainer Abart für die Zusammenarbeit an dem ersten Paper dieses Projekts und für alle anderen Hilfeleistungen. Es seien auch Dr. Elena Petrishcheva und alle anderen Kollegen der Arbeitsgruppe dort gegrüßt.

Ich grüße ferner alle anderen Kollegen, die in der Forschergruppe 741 'Nanoscale processes and geomaterials properties' gearbeitet haben. Diese Arbeit wurde im Rahmen dieser Forschergruppe durchgeführt. Ich danke der Deutschen Forschungsgemeinschaft für die finanzielle Unterstützung.